Using Biomolecular Recognition to Selectively Self-Assemble Microscale Components onto Patterned Substrates

by

Trevor Olsen

A thesis submitted in partial fulfillment of the requirements for the degree of

Master of Science

in

Microsystems and Nanodevices

Department of Electrical and Computer Engineering

University of Alberta

Abstract

Modern nanofabrication technology in the 21st century has continued year after year to push the boundaries of what is possible at the nanoscale. With the advent of molecular electronics, [1] single electron devices, [2] nanoelectromechanical systems (NEMS), [3] and other nanotechnologies, the near future will see a requirement for the die-to-substrate assembly of components that are much smaller than conventional robotic pick-and-place technologies can accommodate. Many researchers have proposed the mechanism of self-assembly to replace robotic pick-and-place technologies and meet the micro/nanoscale assembly needs of some future technologies. [4], [5], [6], [7]

Presented here is a biologically inspired approach for the selective self-assembly of micron-scale components onto lithographically patterned target sites on a substrate. Two mechanisms of selective adhesion through biomolecular recognition are explored and tested in this thesis: the strong protein-ligand interaction between avidin and biotin, [8] and the hybridization interaction that occurs between two complementary single-stranded DNA oligonucleotides. [9] Other than the benefits in scale, the method of integration by self-assembly may be advantageous for its parallel nature, 3D capabilities, and the ability to integrate devices made from incompatible processing technologies into a single platform (heterogeneous integration). Square silicon microtiles with widths ranging from 5 μm to 25 μm were chosen to be test devices (model 'nanochips') for the assembly. These devices, fabricated from silicon-on-insulator (SOI) substrates, were coated with a thin film of gold on one side, deposited by sputtering. A buffered oxide underetch of the buried SiO_2 layer left the microtiles attached to the SOI handle substrate only by narrow SiO_2 pillars. This allowed for facile release of the microtiles into solution from the front side of the substrate by ultrasound fracture of the SiO_2 pillars in a bath sonicator.

In the initial demonstration, self-assembled monolayers (SAMs) were employed to functionalize both the microtiles and the gold pads with biotin and avidin, respectively. Preliminary experiments employed commercially functionalized gold nanoparticles and polystyrene microspheres to develop reliable procedures for forming avidin and biotin SAMs on gold. After the gold-coated microtiles were

functionalized with a biotin SAM and a target substrate had its gold pads functionalized with an avidin SAM, the microtiles were released into a solution of phosphate buffered saline (PBS) containing a low concentration of polysorbate 20. The avidin-functionalized target substrate was then placed in this solution. Self-assembly of the microtiles onto the substrate was achieved by intermittently stirring the solution over 24 hours. In the most successful demonstration, 5 μm square microtiles were self-assembled onto patterned 5 μm square gold pads on the target substrate. After rinsing, the avidin-biotin self-assembly method yielded 2.0% of the total target pads covered by assembled microtiles at a selectivity ratio of 7.3:1 in favour of microtiles affixed to the target pads as opposed to the surrounding silicon substrate. DNA-driven self-assembly of the microtiles was also successfully demonstrated at a lower yield using similar procedures.

Dedicated to my mother Susan

1955-2014

Thank you for all your love, encouragement, and support.

Preface

A summary of the main results from this thesis and many elements from Chapter 5 of this thesis were published in a paper titled "Programmed Self-Assembly of Microscale Components Using Biomolecular Recognition through the Avidin-Biotin Interaction" in the Nov. 2014 (58th EIPBN Conference Special Issue) issue of *Journal of Vacuum Science and Technology B* by T. Olsen, J. Ng, M. Stepanova, and S. K. Dew. [10] For this paper, T. Olsen was responsible for the experimental techniques, results, and analysis, and manuscript composition while J. Ng helped to develop the microtile self-assembly procedure and M. Stepanova contributed to manuscript edits. S. K. Dew was the supervisory author and was involved with concept formation and manuscript composition.

Acknowledgements

I would like to thank my supervisors, Dr. Steven Dew and Dr. Maria Stepanova, for providing me with funding and access to the various laboratories, cleanroom facilities, workspaces, chemicals, and products that I used to complete this work. In particular, my quiet and comfortable workspace in the National Institute for Nanotechnology (NINT) and the chemistry laboratory on the sixth floor of the Electrical and Computer Engineering Research Facility (ECERF) were crucial assets to facilitating the completion of this work. I would also like to thank my supervisors for their exceptional guidance and encouragement throughout this work. It has been a very challenging but rewarding experience, and I will always be grateful for the opportunity that they provided me.

I would like to thank the Natural Sciences and Engineering Research Council (NSERC) of Canada and Alberta Innovates–Technology Futures for providing me with funding in the form of a Master's-level Canada Graduate Scholarship and complementary NSERC Top-Up Award.

I would also like to thank the people in my research group who aided me or guided me with their experience. In particular, I would like to thank Jason Ng, Robert Peters, and Mohammad Ali Mohammad, all of whom gave me some great advice during this work.

I would like to thank all of the University of Alberta Nanofab staff, especially Scott Munro, Les Schowalter, and Stephanie Bozic, for their training and exceptional process guidance. I would also like to thank Ben Pacheco from Cytodiagnostics for giving me some guidance and suggestions for forming mixed self-assembled monolayers on gold.

Lastly, I would like to thank my parents, brothers, and sisters and my girlfriend Katrina for all of your wonderful love and support.

List of Figures

Figure 2.1: Approximate speed (parts assembled per hour) versus part size for a variety of serial assembly methods. This study was performed by Morris *et al.* in 2005 and indicates the size range where they believed self-assembly could have the most significant contributions. The lettering from a to h corresponds to individual atom placement by STM (a), polymer memory storage devices (b), optical tweezers assembly (c), 3D microassembly (d), robotic pick-and-place printed wiring board assembly (e), robotic assembly of a grease gun coupler (f), robotic assembly of automobile wheel bearings (g), and robotic assembly of an automobile body and chassis (h). [6] 4

Figure 2.2: (A) Visualization of Yeh and Smith's gravitationally-driven trapezoidal shape matching self-assembly mechanism. (B) Schematic of their bubble pump apparatus for component recirculation. [30] 8

Figure 2.3: The dynamics of capillary force driven die-to-substrate self-assembly in its standard embodiment. (a) shows a top view three-dimensional perspective whereas (b) shows the same sequence from the side view. [15] 10

Figure 2.4: A hybrid approach to programmable, stochastic, fluidic self-assembly of microparts developed by Stauth *et al*. This approach is driven by molten solder capillary forces, gravity, and shape matching. [22] 14

Figure 2.5: (B) Schematic depicting the details of the automated reel-to-reel molten solder driven fluidic self-assembly machine developed by Park, Jacobs, *et al*. (C) Schematic illustrating the jet pump principle used to achieve recirculation of the chips. [49] 14

Figure 2.6: Illustration of surface tension-directed self-assembly of silicon microchips (60x60x20 μm) at a liquid-liquid-solid interface employing an energy cascade to: move components from suspension to the oil-water interface, pre-orient the components within the interface, and assemble the components onto molten solder (95°C) pads through dipping. [17] 16

Figure 2.7: Stepwise schematic of the robotically-assisted self-alignment procedure of hybrid microassembly, as originally proposed by Sariola, Zhou, *et al*. [56] 18

Figure 2.8: Schematic illustration of electric field driven self-assembly. Electrical biasing of the selected receptor site induces fluidic transport of the component onto the desired location. [28] 19

Figure 2.9: Snapshot views of the magnetic field driven self-assembly process developed by Shetye *et al*. The final shot demonstrates how final alignment of the silicon dies can be induced by vibration of the substrate. [66] 22

Figure 2.10: Proposed process flow for fabrication and release of silicon islands by sonication and then self-assembly driven by single-stranded DNA, as proposed by Bashir *et al*. The process flow goes as follows: (a) pattern SOI substrate with photoresist and deposit Au/Cr, (b) pattern Au/Cr pads by lift-off (c) etch silicon device layer down to buried oxide layer by potassium hydroxide (KOH) etching, (d) underetch buried oxide layer to leave only narrow pillars holding the tiles onto the handle substrate, (e) release silicon islands into solution by bath ultrasonicating to break the oxide pillars, (f) functionalize the gold side of the silicon islands and gold pads on a target substrate with complementary single-stranded DNA SAMs and induce self-assembly of the islands onto the target substrate. [73] 24

Figure 2.11: An initial demonstration of microscale DNA-driven self-assembly of silicon islands which were functionalized and assembled together to form duplexes. [74] 25

Figure 2.12: Results showing 1 μm diameter polystyrene microspheres self-assembled onto a patterned target circle using two SAMs of complementary single-stranded DNA. [76] 25

Figure 2.13: Schematic illustration of proposed self-assembly mechanism where biotinylated double-stranded DNA SAMs are functionalized on both the substrate and the devices and avidin is used as the linking element. [82] 28

Figure 2.14: Molecular structure of the biotin molecule. The valeric acid side chain on the left side is commonly used to incorporate various reactive groups that can attach the biotin molecule onto other molecules without impairing the functionality or avidin-binding capability of the biotin molecule itself. [95] 30

Figure 2.15: Scheme of the different steps taking place during SAM formation on a metal surface: (i) physisorption, (ii) lying down phase formation, (iii) nucleation of the standing up phase, (iv) completion of the standing up phase. [105] 32

Figure 3.1: SEM image of Cytodiagnostics' 100 nm wide biotin-functionalized gold nanoparticles illustrating their platonic structure. It should be noted the nanoparticles in this image were not self-assembled using the avidin-biotin interaction, but were immobilized onto a substrate by allowing a droplet to evaporate. 34

Figure 3.2: Schematic illustration of the procedure used to form an avidin SAM on the target gold pads. This 3-step illustration first shows the thiol adsorption of MUA onto the target gold pad to form an MUA SAM. The second step involves the addition of EDC to form an *O*-acylisourea intermediate on the end of the MUA. In the third step, the primary amine group on an avidin protein replaces the *O*-acylisourea intermediate so that the avidin becomes the functional group of the SAM while an isourea by-product is released. 37

Figure 3.3: Sample SEM image of 100 nm biotin-functionalized gold nanoparticles selectively self-assembling onto the target gold pad (left) with much lower yield assembly onto the background silicon substrate (right). 39

Figure 3.4: Illustration of some of the steps to the ImageJ nanoparticle counting analysis. (A) The threshold function is used to make the nanoparticles appear black and the background (gold or silicon) appear white. (B) After the analyze particles function is used to count the number of assembled nanoparticles, ImageJ can identify exactly which nanoparticle is counted for each number with red text inserted inside the outline of each nanoparticle 41

Figure 3.5: A comparison of two of the most successful self-assemblies of 100 nm wide biotin-functionalized gold nanoparticles onto avidin-functionalized target gold pads. The exact same avidin SAM formula was used for both results and the only experimental variation was the rinsing/sonication procedure afterward. In the upper two images, the substrate was rinsed with isopropyl alcohol (IPA) and no sonication was performed. In the lower two images, the substrate was submerged in an IPA bath and then sonicated at a low intensity setting for 5 minutes, followed by further IPA rinsing. The two images on the left are 3,000X magnified images showing the entire 25 μm x 25 μm target gold pad while the two images on the right are 10,000X magnified for the particle counting analysis. 45

Figure 3.6: SEM image of a sample that had a sacrificial SiO_2 layer deposited by PECVD on top of the silicon substrate before the gold pads were deposited and patterned. This substrate had biotin-functionalized gold nanoparticles self-assembled onto its avidin-functionalized gold pads by the procedure outlined in section 3.1. After the after the assembly, however, the SiO_2 layer was wet etched

away by a dip in BOE, which removed a large majority of the non-specifically bonded nanoparticles on the background substrate..... 47

Figure 4.1: Schematic illustration of the procedure used to form the biotin SAM on the gold pads of the target substrate. The sequential addition of longer biotin-PEG-SH chains (molecular weight of 10 kDa) and then shorter methoxy-PEG-SH chains (5 kDa) forms a mixed monolayer SAM with spaced apart biotin molecules available at the surface of the monolayer. From the molecular weights of these PEG chains, it can be estimated that n in the figure is approximately equal to 111, while m is approximately equal to 108. 53

Figure 4.2: A visual depiction of some of the steps involved in the ImageJ microsphere counting analysis. (A) An original SEM image taken on a random target gold pad on a 11.11 μg/mL biotin-PEG-SH concentration sample from the 0.82 μm diameter microsphere batch. (B) The same image after using ImageJ's threshold, crop, noise despeckle, and watershed functions. (C) The image after the ImageJ analyze particles function has been used to count the number of assembled microspheres, with the count of each microsphere indicated by red text inserted inside the outline of each one. 56

Figure 4.3: An example histogram plot where the centroid-to-centroid distances between all of the possible pairs of assembled microspheres on a target pad were computed and placed into distance bins that were selected to be multiples of the average microsphere diameter on the target pad. This sample histogram was generated from an image in the 1.34 μm diameter microsphere batch. 58

Figure 4.4: A visual summary of the ImageJ counting analysis performed on the 0.82 μm diameter and 1.34 μm diameter microsphere batches. Based on the closest match to the average self-assembled microsphere density, one ImageJ-modified image from each of the biotin-PEG-SH reagent concentrations tested was chosen for this figure. Viewing them next to each other, the effect of the SAM formation reagent concentration on the final self-assembly density can be seen visually..... 59

Figure 4.5: This graph of the results from Table 2 plots the average assembled microsphere density (from ImageJ analysis) vs. the concentration of biotin-PEG-SH reagent that was used during the SAM formation. The results from all three microsphere sizes that were tested are included in this plot. It should be noted, however, that they are all scaled differently so that they can all be shown on the same plot. 62

Figure 4.6: The same neighbouring microspheres histogram from Figure 4.3 (in blue) but with an added random distribution histogram (red) inserted next to it for visual comparison. 65

Figure 4.7: Plot of the average ratio between the observed and predicted (random distribution) histogram *2d* bin values vs. the concentration of biotin-PEG-SH reagent that was used during the SAM formation step for the 0.82 μm and 1.34 μm microsphere batches. 66

Figure 4.8: Plot of the ratio between the observed and predicted (random distribution) *2d* bin histogram values vs. the assembled microscope density of each of the 1.34 μm microsphere target pad images that was analyzed for clustering. As can be seen from the graph, the values are linearly correlated with each other with negative proportionality constant. A linear fit placed on the data using Origin resulted in a slope of -8.72 ± 0.75. 68

Figure 5.1: Process flow diagram illustrating the entire experimental procedure from microtile fabrication to target substrate and microtile functionalization and finally the assembly of the released microtiles onto target gold pads on the target substrate. 71

Figure 5.2: Photographs taken from directly above the SOI substrate as it goes different stages of processing. (A) After Cr and Au are sputtered on top of the Si device layer and then the substrate is patterned by photolithography. (B) After Au/Cr wet etching. (C) After Si reactive-ion etching. (D) After BOE undetching of the oxide, leaving the handle Si substrate visible. 74

Figure 5.3: SEM images of silicon microtiles fabricated from an SOI wafer. (A) Silicon microtiles with buried oxide layers that have been etched by BOE so that only a narrow pillar of SiO_2 holds the microtile. The substrate in this figure has already undergone bath ultrasonication so most of the microtiles have been released into solution. (B) A closer look at an underetched microtile illustrating the amount of underetching required to break off the tiles with a very high yield during sonication. 75

Figure 5.4: Schematic illustration of the procedure used to form the biotin SAM on the gold-coated silicon microtiles (while they remained fixed on the handle substrate by thin SiO_2 pillars). The sequential addition of longer biotin-PEG-SH chains (molecular weight of 10 kDa) and then shorter methoxy-PEG-SH chains (5 kDa) formed a mixed monolayer SAM with spaced apart biotin molecules available at the surface of the monolayer. From the molecular weights of these PEG chains, it can be estimated that n in the figure is approximately equal to 111, while m is approximately equal to 108. 79

Figure 5.5: Photographs of self-assembly setup. (A) Magnetic stirring hotplate with a centrifuge tube on it being held vertically by a yellow stand. (B) A closer look at the contents of the centrifuge tube (from bottom to top): 1/8" magnetic stir bar, cross-shaped holder, SEM stub, target gold pad substrate super-glued onto SEM stub. 81

Figure 5.6: SEM image of 5 µm square silicon microtiles selectively self-assembled onto a large gold area (pictured grey) instead of the silicon substrate (pictured black). An assembled microtile density of up to 999 tiles/mm^2 was achieved on large gold areas. 86

Figure 5.7: SEM image of 5 µm square silicon microtiles selectively assembled onto wide gold pads and stripes with high selectivity. 87

Figure 5.8: SEM images of 5 µm square silicon microtiles that have landed on target gold pads of the same size. (A) The typical yield, selectivity, orientation and degree of pad overlap that can be seen between the microtiles and target gold pads across the wafer. (B) A 5 µm square microtile that is completely overlapping and very well aligned with its target gold pad. 87

Figure 5.9: A large area SEM image illustrating the yield and selectivity of 5 µm square silicon microtiles assembled onto 5 µm square gold pads across the target substrate. 2.05% of the target gold pads were covered by microtiles and the selectivity ratio of microtiles on the pads as opposed to off of the pads was found to be 7.32:1. 88

Figure 5.10: SEM images demonstrating the fabrication and assembly of 25 µm wide square silicon microtiles that were made and tested using similar procedures to the 5 µm microtiles discussed earlier. (A) A 25 µm wide microtile that has been BOE underetched and still remains on the SOI wafer after sonication release has released most of the surrounding microtiles on the substrate. (B) 25 µm square silicon microtiles affixed to 25 µm wide target gold pads with a high selectivity but poor yield. 90

Figure 5.11: SEM images demonstrating the fabrication and assembly of 5x10 µm rectangular microtiles that were fabricated using the exact same procedures as the 5 µm square microtiles. (A) A 5x10 µm rectangular microtile that has been BOE underetched and still remains on the SOI wafer after sonication release has released of most of the surrounding microtiles. (B) A 5x10 µm rectangular microtile that has successfully landed on a target pad of the same size. 92

Figure 6.1: SEM images demonstrating the successful low-yield assembly of 5 μm wide square silicon microtiles driven by complementary single-stranded DNA oligonucleotides. (A) A lower magnification SEM image demonstrating the low assembly yield but good selectivity of the microtiles landing on the target gold pads as opposed to the background silicon substrate. (B) A higher magnification SEM image showing a microtile affixed to a target gold pad. 99

Figure 8.1: Illustrations of the model employed to derive Equation 4.1. (A) demonstrates the area of a particular bin for a particle located far from the pad's boundaries, (B) demonstrates the areas near the pad boundaries where the frequencies are affected by the boundaries, (C) demonstrates the model when assuming that the effect of the boundary along the *x*-direction is negligible because the pad length in the *x*-direction (L_x) is much longer than in the y-direction (L_y), and (D) demonstrates the effects of the pad boundaries on the corresponding bin area when a particle is located within Bin_{upper} of the pad boundary. [141] 109

Figure 8.2: Circuit level schematic and wiring diagram of the timer apparatus used to switch on (provide power to) the magnetic stirrer in 2 minute cycles for 24 hours. This apparatus was designed and constructed by Jason Ng. [124] 110

Figure 8.3: (A) Photostitched image of entire 7 mm x 4.5 mm target pad substrate (30 images from confocal microscope) with 5 μm square silicon microtiles assembled onto gold pads of the same size. This photostitch is from the most successful assembly run, with 2853 microtiles assembled overlapping with the target gold pads and 390 on the background silicon substrate, (B) The same photostitched substrate image after an ImageJ analysis counted the total number of microtiles on the substrate (on and off pads) to be 3243. The microtiles that landed on the target gold pads are labeled in green, while the microtiles on the background silicon (off of the pads) are labeled in red. 111

List of Tables

Table 1: Summary of Main Results from Gold Nanoparticle Self-Assembly Experiments..... 43

Table 2: Summary of Results from Avidin-Coated Microsphere Self-Assembly Experiments..... 60

List of Abbreviations

BOE – Buffered oxide etch

CMOS – Complementary metal oxide semiconductor

DNA – Deoxyribonucleic acid

EDC – 1-ethyl-3-(3-dimethylaminopropyl)carbodiimide

EDTA – Ethylenediaminetetraacetic Acid

EHT – Extra High Tension

ELISA – Enzyme-Linked Immunosorbent Assay

EMSA – Electrophoretic mobility shift assays

FACS – Fluorescence activated cell sorting

HF – Hydrofluoric acid

HPLC – High performance liquid chromatography

PBS – Phosphate-buffered saline

PBSP – Phosphate-buffered saline (1x) + polysorbate 20 (0.05%)

ICP – Inductively coupled plasma

IPA – Isopropyl alcohol

LED – Light-emitting diode

MES – 2-(*N*-morpholino)ethanesulfonic acid

MUA – 11-Mercaptoundecanoic acid

NEMS – Nanoelectromechanical systems

PCR – Polymerase chain reaction

PDMS – Polydimethylsiloxane

PEG – Polyethylene glycol

RFID – Radio-frequency identification

RIE – Reactive-ion etching

RNA – Ribonucleic acid

RPM – Revolutions per minute

SAM – Self-assembled monolayer

SEM – Scanning electron microscope

SH – Sulfhydryl group, also known as a thiol group when bonded to carbon

SOI – Silicon on insulator

SPA – Scintillation proximity assay

SPR – Surface plasmon resonance

SSPE – Standard Saline Phosphate EDTA

Sulfo-NHS – *N*-hydroxysulfosuccinimide

TEA – Triethanolamine

TCEP – *Tris*(2-carboxyethyl)phosphine

Table of Contents

1. Introduction 1
2. Self-Assembly of Microscale Devices: A Literature Review 3
2.1. Die-to-Substrate Assembly of Microscale Devices 3
2.2. Methods of Fluidic Self-Assembly 6
2.2.1. Shape Recognition (Gravitationally Driven) 7
2.2.2. Capillary Force Driven 9
2.2.2.1. Capillary Forces: Molten Solder Driven 12
2.2.2.2. Capillary Forces: Liquid-Liquid Interface Driven 15
2.2.2.3. Hybrid Microhandling: Robotically Assisted Self-Alignment 17
2.2.3. Electric Field Driven 19
2.2.3.1. Electrophoresis Driven 20
2.2.4. Magnetic Field Driven 21
2.2.5. DNA Driven 23
2.3. Self-Assembly by Protein-Ligand Interactions 26
2.3.1. Overview of Proteins 26
2.3.2. Protein-Ligand Driven Self-Assembly of Micro- and Nano-scale Devices 26
2.3.3. The Avidin-Biotin Interaction 28
2.4. Self-Assembled Monolayers 31
3. Self-Assembly of Biotin-Functionalized Gold Nanoparticles 34
3.1. Experimental 34
3.1.1. Experimental Overview 34
3.1.2. Target Substrate Fabrication 35
3.1.3. Avidin SAM on Target Substrate Gold Pads 36
3.1.4. Self-Assembly Procedure 38
3.1.5. Yield and Selectivity Measurement 39
3.2. Results & Discussion 43
3.2.1. Variations to the Experiment 45
3.3. Conclusion 48
4. Self-Assembly of Avidin-Coated Polystyrene Microspheres 50
4.1. Experimental 50
4.1.1. Experimental Overview 50
4.1.1. Target Substrate Fabrication 51

4.1.2. Biotin SAM on Target Substrate Gold Pads 51
4.1.3. Self-Assembly Procedure 54
4.1.4. Assembled Microsphere Density Calculation 55
4.1.5. Clustering Analysis 57
4.2. Results & Discussion 59
4.2.1. Clustering Analysis 64
4.3. Conclusion 68
5. Avidin-Biotin Driven Die-to-Substrate Self-Assembly of Silicon Microtiles 70
5.1. Experimental 70
5.1.1. Experimental Overview 70
5.1.2. Silicon Microtile Fabrication 71
5.1.3. Target Substrate Fabrication 76
5.1.4. Avidin SAM on Target Substrate Gold Pads 77
5.1.5. Biotin SAM on Gold-Coated Silicon Microtiles 77
5.1.6. Microtile Sonication Release Procedure 79
5.1.7. Microtile Self-Assembly Procedure 80
5.1.8. Yield-Reducing Experimental Variations 81
5.1.9. Yield and Selectivity Measurement 84
5.2. Results & Discussion 85
5.2.1. Selectivity and Yield 88
5.2.2. Microtile Shape and Size Variations 90
5.2.3. Discussion 92
5.3. Conclusion 94
6. Single-Stranded DNA Driven Microtile Self-Assembly 95
6.1. Experimental 96
6.2. Results & Discussion 98
6.3. Conclusion 100
7. Conclusion and Future Work 101
7.1. Future Work 103
8. Appendix 107
8.1. Derivation of Equation 4.2 107
8.2. Supplementary Figures 110
Works Cited 112

1. Introduction

As nanoelectronic devices and integrated circuits continue to scale down year after year through developments in nanofabrication technology, the traditional die-to-substrate assembly technologies for such devices may not be able to continue scaling down. The current industry standard for such assembly is called robotic pick-and-place. [11] Although this can be a very high throughput process when alignment and placement accuracy are not of paramount concern, the near future will soon require the ability to assemble much smaller devices than conventional robotic pick-and-place technologies can accommodate. [6] The concept of self-assembly has been explored in a vast amount of research, and it has been proposed many times as a new integration paradigm to replace robotic pick-and-place and meet the needs of many technologies that require the assembly of micro and nanoscale devices. [4], [6], [5], [7], [12], [13] The main motivation behind the work in this thesis is the vast potential for biologically-inspired self-assembly mechanisms to be employed for the assembly of microscale technologies such as integrated circuits or microelectromechanical systems (MEMS). Another motivation was the ability to exploit some very powerful assembly technologies found in nature. Selective adhesion through biomolecular recognition occurs in many aspects of nature, but two promising examples are explored in this thesis: the strong protein-ligand interaction between avidin and biotin, [8] and the hybridization interaction that occurs between two complementary single-stranded DNA oligonucleotides. [9] The goal of this work was to exploit these natural nanotechnologies to realize the assembly of nanofabricated semiconductor devices.

Chapter 2 of this thesis presents a literature review on the die-to-substrate self-assembly of microscale devices. Many different driving forces of self-assembly are described and discussed, as well as some extra concepts that are fundamental to this thesis, such as the avidin-biotin protein-ligand binding interaction and or thiol-based self-assembled monolayers (SAMs).

Chapter 3 details and discusses experiments that were performed with biotin-functionalized gold nanoparticles for the purposes of developing a procedure for forming a functional avidin SAM on gold. In similar form to Chapter 3, Chapter 4 details and discusses experiments that were performed with avidin-

coated polystyrene microspheres for the purposes of developing a procedure for forming a biotin SAM on gold.

The two SAM procedures developed in Chapters 3 and 4 are both employed in Chapter 5, in which gold-coated silicon microtiles are fabricated, functionalized, and released into solution from a silicon-on-insulator substrate. These devices are test devices for the self-assembly of microscale integrated onto functionalized target sites via the avidin-biotin binding interaction. An imaging analysis was carried out after the assembly to evaluate the yield and selectivity of the binding. Chapter 6 outlines and discusses experiments that were performed using the exact same methodologies as in Chapter 5, but complementary single-stranded DNA oligonucleotide SAMs were instead employed to drive the assembly of the microtiles.

Chapter 7 concludes this thesis with an overview of the results and outcomes of this work. This conclusion chapter also contains a proposal future work that could be performed to further investigate the capabilities of this approach. Chapter 8 is an appendix that includes equation derivations and supplementary figures.

2. Self-Assembly of Microscale Devices: A Literature Review

2.1. Die-to-Substrate Assembly of Microscale Devices

Although CMOS-based electronics are continuing to scale down and push performance abilities with the traditional planar chip approach, a continuously rising trend in the field of nanotechnology, commonly dubbed 'More than Moore', [14] is the fabrication of complicated, multifunctional non-planar device architectures. These advanced devices may utilize complex architectures such as the integration of multiple components made from incompatible fabrication processes into one standalone platform (heterogeneous integration), three-dimensional integration of components, or interfaces between electronic and non-electronic domains. Presently, the most common die-to-substrate assembly technique used in microelectronic manufacturing lines is robotic pick-and-place, where automated tools integrate components by physically picking them up, moving them to the desired location, and bonding them into place through mechanical, electrical, or chemical means. [15] For many years, this high-yield method has well suited the needs of consumer electronic manufacturing, with possible throughputs reaching up to 100,000 assembled parts per hour. [16] Such high assembly rates, however, are only possible for relatively low positioning accuracies, on the scale of tens of micrometers. If higher accuracy is needed, the throughput must be dramatically lowered. As can be seen from Figure 2.1, which presents a comparison of assembly rates from various serial-based assembly technologies, the possible assembly rate of parts severely decreases as the part size becomes lower than 300 μm. [6] With the advent of molecular electronics, [1] single electron devices, [2] nanoelectromechanical systems (NEMS), [3] and other nanoscale components, the near future will soon see a requirement for the die-to-substrate assembly of systems that are much smaller and more complicated than conventional robotic pick-and-place technologies can accommodate.

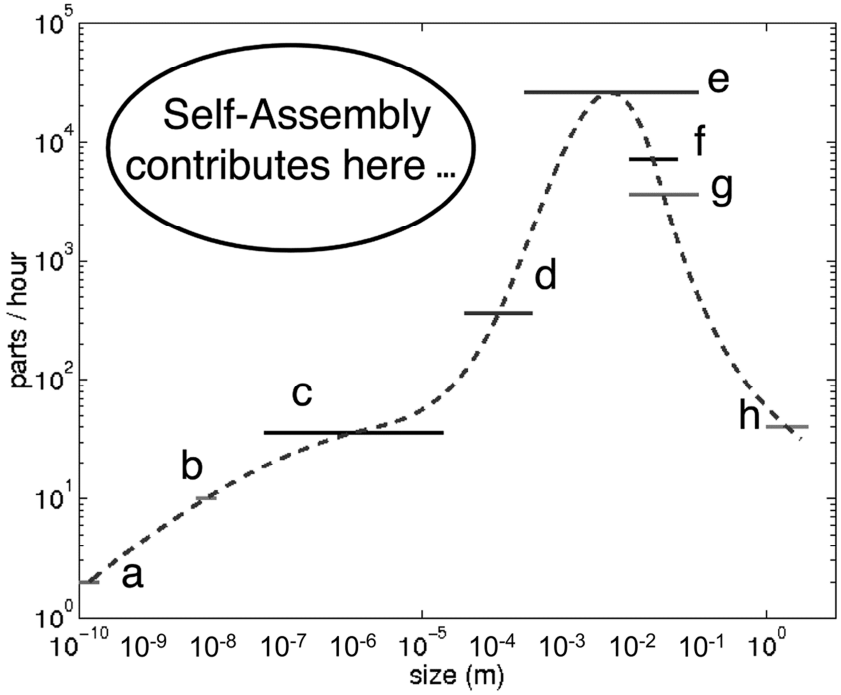

Figure 2.1: Approximate speed (parts assembled per hour) versus part size for a variety of serial assembly methods. This study was performed by Morris *et al.* in 2005 and indicates the size range where they believed self-assembly could have the most significant contributions. The lettering from a to h corresponds to individual atom placement by STM (a), polymer memory storage devices (b), optical tweezers assembly (c), 3D microassembly (d), robotic pick-and-place printed wiring board assembly (e), robotic assembly of a grease gun coupler (f), robotic assembly of automobile wheel bearings (g), and robotic assembly of an automobile body and chassis (h). [6]

A few alternative assembly mechanisms have been proposed to integrate components smaller than 300 μm. Inkjet printing, for example, may be a very suitable easy-to-integrate method for producing low-performance electric devices. [17] Unfortunately, this method is not yet adequate for producing higher performance inorganic devices, which are typically formed by high temperature processes. Another recent assembly technology that may soon become an industry-scalable option is the robotically assisted method of transfer printing microchips using microstructured elastomeric surfaces. [18] This technique uses a soft stamp made from an elastomer such as polydimethylsiloxane (PDMS) to grab microchips from a source wafer and release them at desired locations on a target substrate. Inspired by the aphid, a sap-sucking insect, this method relies on pressure induced sagging of the microtip-structured elastomeric surface to provide extreme, reversible levels of switchability in generalized adhesion, with strong to weak ratios from retrieval to delivery of higher than 1000. By realizing close control of the force and speed of the

initial contact and retraction of the components, this method works simply by the action of the generalized adhesive forces to the PDMS, which are typically dominated by van der Waals interactions. [19]

Unlike typical robotic pick-and-place systems, which grab and place their components serially, this transfer printing technique can be performed with many components in parallel over large areas, and specific component locations can be programmed by specifically structured stamps. This method, however, is still robotically assisted and requires high-resolution microscopy cameras for accurate alignment, thus there can be issues when scaling down. Kim, *et al*. demonstrated this technique with 100x100 μm wide square silicon microtiles at throughputs corresponding to millions of parts assembled per hour. [18] The silicon microtiles were fabricated and released from a silicon-on-insulator (SOI) wafer with a similar underetching technique to that described in the Chapter 5.1.2 of this thesis. Another powerful advantage of this method is its ability to transfer print onto extremely rough surfaces. By using a stamp with 5 microtips (4 at each corner and 1 in the middle), it was possible to transfer print the silicon microtiles onto a rough surface of ultrananocrystalline diamond, where the estimated contact area between the microtile and the diamond was estimated to be less than 1% of the microtile area. [18]

Due to the scaling limitations of robotic pick-and-place assembly, a new die-to-substrate integration paradigm must be developed. An ideal assembly method for devices measuring less than 100 μm is one that can handle many parts in parallel, integrate heterogeneous components made from different processes onto one common substrate, and be able to organize and position parts in planar, nonplanar, and/or 3D geometries. The non-contact, typically fluid-mediated method of self-assembly has been used to localize and assimilate micro- and nano-scale components in numerous applications such as bioelectronics, novel microelectronic architectures, tissue engineering, metamaterials, nanomedicine, and photonics, and it has been proposed to meet the future needs of die-to-substrate assembly. [7]

2.2. Methods of Fluidic Self-Assembly

A great amount of research has gone into the prospect of fluidic self-assembly to meet the needs of modern non-planar device architectures. Self-assembly of microscale components and devices has been proposed and demonstrated with many different driving mechanisms. Typically, a common pattern of these mechanisms is that they are driven by a global minimization of the system free energy to reach a desired system configuration. [20] Kinetic energy is usually added to help move the system away from local minima in the associated energy landscape so that the assembly process can essentially continue to run unsupervised until a minimal system free energy configuration can be reached. The ability of the system to run on its own is what gives it the designation *self-assembly*.

Since the proposed goal of this research was to investigate a new method for integrating electrical components onto substrates, the first portion of this review will be focused on die-to-substrate self-assembly, where many parts are assembled onto specific patterned locations on substrates. More specifically, the majority of the literature in this review uses fluidic mass transport as a medium to get the dies to the substrate. Unlike robotic pick-and-place systems, the majority of methods in this review are also parallel in nature, meaning many (or all) of the parts can be assembled simultaneously. In regards to the spatial and temporal availability of the components in proximity to the target substrate sites, fluidic self-assembly can be either deterministic or stochastic in nature. An example of deterministic fluidic self-assembly is an approach implemented by Chung *et al*., where 'railed microfluidics' were used to guide and assemble 50 μm wide polymeric microstructures in fluidic channels. [21] The rails were made up of grooves on the top surfaces of the channels that were complementary to similar fabricated grooves on the microstructures. A large majority of fluidic self-assembly systems, however, are stochastic in nature, and so is the project described later in this thesis. An important but difficult aspect of stochastic die-to-substrate self-assembly is to achieve control over the selectivity and directionality of the binding interactions driving the components. This is typically done by patterning the surfaces on the target substrate and then using chemical affinities, wetting properties, interface energies, or electromagnetic fields to tailor the system to handle components as desired. [20] For the heterogeneous integration of

different types of parts onto the same substrate, programmability is also a commonly desired feature of fluidic self-assembly. Programmability means that someone controlling the experiment can choose in advance which specific binding sites the components in a certain run should assembled onto. This can be achieved through programmed variations in the dies and the binding sites such as different part shapes, [22] different solder melting points, [23] different complementary deoxyribonucleic acid (DNA) sequences, [24] different protein-ligand interactions, [25] or electrically induced programming through electrically de-activated SAMs, [26] electrically heated solders, [27] or programmed electric fields. [28]

Some examples of non-biological mechanisms that can drive fluidic self-assembly include shape recognition (gravitationally driven), capillary forces (molten solder driven, liquid-liquid interface driven), electric fields, electrophoresis, and magnetic fields. Selective adhesion based on biomolecular recognition is another popular approach to achieving such assembly. Examples of selective binding in biology include complementary DNA strands, antibody-antigen pairs, or certain protein-ligand combinations. Although similar research efforts have exploited DNA to self-assemble micron-scale devices, the work in this thesis instead employs a very strong protein-ligand interaction to achieve such assembly.

2.2.1. Shape Recognition (Gravitationally Driven)

In 1994, Berkeley researchers Hsi-Jen Yeh and John S. Smith developed a novel approach for the assembly of trapezoidal-shaped GaAs light emitting diodes (LEDs) ranging in size from 5 μm to 24 μm wide onto silicon substrates. [29] This technique was driven by gravitational forces and worked because of the complementary interlocking three-dimensional shapes designed for the devices and the target sites. Trapezoidal holes in the silicon target substrate were fabricated by ethylenediamine pyrocatechol anisotropic etching, which selectively etches along the {111} plane of (100) silicon substrates to form a 55° angle with the horizontal wafer surface. The LED devices were fabricated from a 10 μm thick GaAs layer deposited on top of an AlAs etch stop/release layer by molecular beam epitaxy. [29] These components were fabricated to have the same dimension and trapezoidal shape as the holes in the target substrate by using ion-milling etching to produce similar side profile angles to the ethylenediamine pyrocatechol etch of the substrate. In later implementations, silicon devices were fabricated with

matching trapezoidal shapes to the silicon target substrates holes by using potassium hydroxide (KOH) anisotropic etching. [30] In a typical assembly, the parts were randomly distributed onto the target substrate, and an external agitation or flow was used to move them around until they fell into shape matched recesses due to gravity, as shown in Figure 2.2A.

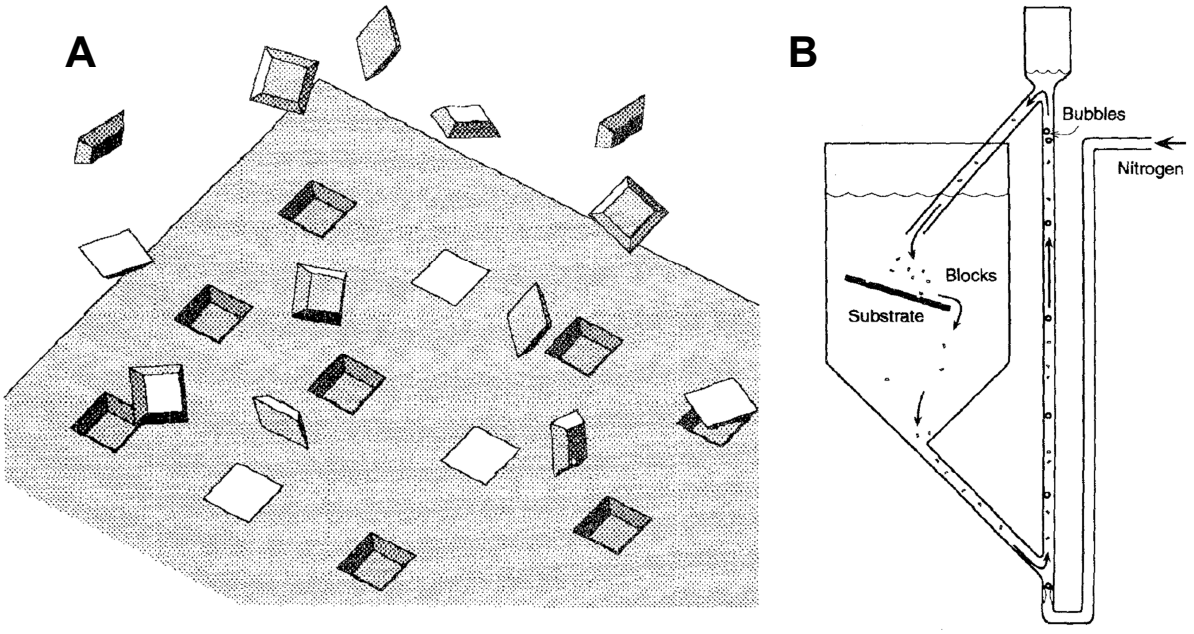

Figure 2.2: (A) Visualization of Yeh and Smith's gravitationally-driven trapezoidal shape matching self-assembly mechanism. (B) Schematic of their bubble pump apparatus for component recirculation. [30]

Once fallen, the components typically remained in place due to gravity, friction, and, van der Waals forces, but electrical interconnections were added after assembly to permanently fix the components in place. Yeh and Smith also developed the first ever self-assembly recirculation apparatus, which improved yield by using a bubble pump mechanism to recirculate unbound components for use in multiple passes, as shown in Figure 2.2B. [30] They patented the original technique and used it as the basis for a company called Alien Technology, which still today specializes in the manufacturing and assembly of radio-frequency identification (RFID) tags. [5], [31] Further modifications to the technique included improved flow and recirculation mechanisms, further variety of shapes and sizes for programmability, hydrophilic and hydrophobic surface treatments for improved selectivity, rounded three-dimensional shapes for more accurate shape matching, [32] and improved methods for identifying and interrogating

multiple assembled RFID tag devices. [33] Present day industrial versions of the technology can reach throughputs of up to 2 million parts assembled per hour. [13]

2.2.2. Capillary Force Driven

In the late 1990's, the George Whitesides group out of Harvard University developed a pioneering approach to the self-assembly of regular, open three-dimensional mesostructures (millimeter-scale) [34], [35], [36] that exploited capillary and hydrophobic effects to reproduce many aspects of supramolecular chemistry (namely bond selectivity and directionality) at the millimeter scale. This approach became the major inspiration for the first capillary driven die-to-substrate fluidic self-assembly method in 2001, by Srinivasan *et al*. [37] In the original Srinivasan proposal, a hydrophilic quartz substrate was patterned with gold target pads that were later functionalized with a 1-octadecanethiol self-assembled monolayer (SAM) to make the gold pads hydrophobic. [37] The substrate was then dipped into a water solution with a film of hydrophobic photopolymerizable methacrylate adhesive on top so that thin films of the adhesive would selectively coat the target pads and not the native substrate surface due to the large wetting contrast. [38] The photopolymerizable methacrylate, a high interfacial energy liquid layer, provided a means for lubrication, self-alignment, and bonding of the chips to be assembled. Gold-coated silicon microtile chips were fabricated from an SOI wafer to be the same size and shape as the target pads. Hydrofluoric acid was used to underetch the buried oxide layer under the microtiles until they were released into the HF solution. Successive dilutions of methanol, and then water, were then used to rinse the microtiles and transfer them into a water solution with higher microtile concentration. Many different shapes and sizes of the microtile devices were tested, ranging from 150 μm to 400 μm in microtile width and from 15 μm to 50 μm in microtile thickness. The gold sides of the microtiles were also functionalized with a 1-octadecanethiol SAM to make them hydrophobic, whereas the silicon side of them was hydrophilic. The assembly was induced by pipetting the functionalized microtile solution onto the target substrate while underwater and using a gentle stream of water to remove unbound parts.

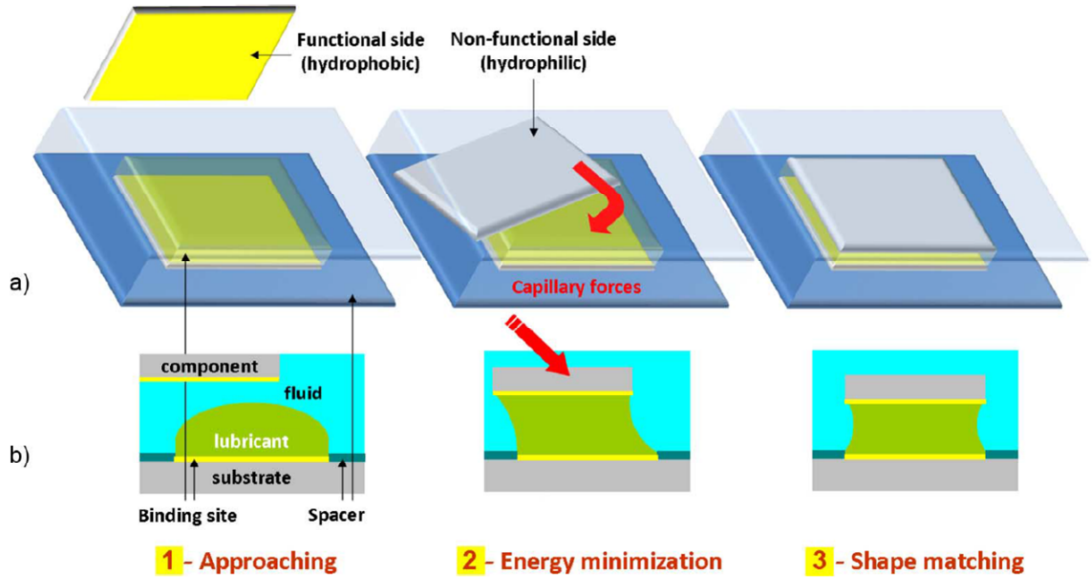

Figure 2.3: The dynamics of capillary force driven die-to-substrate self-assembly in its standard embodiment. (a) shows a top view three-dimensional perspective whereas (b) shows the same sequence from the side view. [15]

Figure 2.3 depicts the fundamentals of Srinivasan's capillary force driven die-to-substrate self-assembly. Once contact between the hydrophobic side of the microtile was made with the hydrophobic target pad film, spontaneous wetting drove the self-assembly and self-alignment of the microtiles. The liquid layer interface attempted to minimize its interfacial energy by maximizing overlap between the microtiles and the target pads, which resulted in highly accurate placement and orientation of the microtiles. Average alignment precisions of less than 0.2 µm and average rotational misalignments of less than 0.3° were achieved. [37] High assembly yields of up to 100% for the 400 µm microtiles were also obtained by performing consecutive pipette and rinse cycles and using a much larger number of fabricated microtiles than target pads. After the fluidic self-assembly, permanent bonding was obtained by ultraviolet exposure of the adhesive through the backside of the transparent quartz substrate. A heat-curable version of the adhesive was also developed for bonding to opaque substrates such as silicon. [39] Mastrangeli *et al*. later introduced a simple technique for achieving perfectly conformal dip-coatings on arbitrary target sites patterned on surfaces. [40] By surrounding the target pads with a relatively thin wetting sidewall, the shape of the fluid drop can be constrained to adhere to all of the geometric features

of the target pad. This technique significantly improved the reproducibility of the dip-coating process and made it much less sensitive to surface defects.

In 2003, Xiong *et al*. further developed Srinivasan's method to add programmability, enabling the heterogeneous assembly of multiple types of components onto the same substrate. [26] Using a similar approach, they fabricated an oxidized silicon target substrate with gold pads coated with a hydrophobic SAM and then dip-coated the substrate with an adhesive lubricant droplet formed on the target pads. They adopted a controllable electrochemical method to desorb the hydrophobic SAM from select gold target pads by applying an electrical potential between the gold and the aqueous environment. [41] By patterning circuits to certain selected pads on the target substrate, some pads were selectively deactivated by SAM desorption before each assembly step. These SAMs could then be reformed afterwards for subsequent batch assembly steps. In their demonstration, an array of multi-coloured 1 mm wide commercial LED components was assembled onto a substrate using a heat-polymerizable adhesive. The electrical connections for each were formed later by solder electroplating to form connections between small metal bases that were patterned on the outer edges of the LEDs as well as just outside of the target pad sites.

Orientation control of assembled parts was shown to be possible by designing the shape of the fluidic droplet. [42] Lin *et al*. demonstrated that a teardrop shape pattern with an elliptical hole could be used to induce unidirectional assembly of 1000 μm wide dies. The teardrop shape was patterned onto both the target substrate and the bottom of the tile-shaped dies, and SAMs were used to make both of these regions hydrophobic. The rest of the substrate and tiles were made hydrophilic and teardrop-shaped droplets were dip-coated from an acrylate-based adhesive onto the target sites. In their demonstration, a 100% unidirectional assembly yield was achieved with a lateral accuracy of 15 μm and a standard deviation of aligned angular orientation of only 0.9°. [42]

In 2005, Liang *et al*. made use of water-coated hydrophilic target pads to self-assemble 1000 μm wide silicon resonator MEMS chips in air. [43] The semi-dry environment helped to avoid stiction issues commonly associated with MEMS devices in fluidic carriers. The air/water interface also has a higher interfacial energy and capillary force than the water/methacrylate interface seen earlier. The patterned

target substrate was dip coated to form water droplets on its pads and then it was mounted upside down above a vibrating diaphragm. The diaphragm was agitated by a sinusoidal wave that imparted kinetic energy into the chips (without substantial damage) so that they would bounce up and make contact with the substrate, sticking and self-aligning to the water-coated target sites. The rest of the substrate was gold coated and covered by a dodecane–thiol SAM to make it hydrophic so that the parts did not adhere to it. An assembly rate of 0.125 parts/second·site was achieved at an assembly yield of 93%. [43]

After many years of refinements and improvements being made to the original capillary force driven technique, Mastrangeli *et al*. studied several failure modes that affected the technique and prevented it from reaching industry-scalable realization. [15] Three-dimensional aggregation of parts and disruption of the fluidic target pad coatings were identified as the most serious impairments to yield. Due to the same interactions that drive the self-assembly processes, such as hydrophobic interactions, direct contact between multiple parts may frequently lead to unwanted aggregations of parts. Air bubbles in the containers were also shown to be a primary cause of aggregation. The impact of flowing parts on the target site fluidic coatings was also cited to reduce yield and alignment capabilities because of distortions in the fluid coatings. Collisions with unbound flowing parts in the solution may also remove correctly bound parts from their target pads.

2.2.2.1. Capillary Forces: Molten Solder Driven

In 2002, Heiko O. Jacobs *et al*. used a low temperature molten solder to perform a similar capillary force induced fluidic self-assembly of 300 μm wide cubic LEDs. [44] In a similar approach to the one first proposed by Srinivasan, the minimization of free energy at the solder-water interface provided the driving force for the assembly and self-alignment. A flexible cylindrical target substrate was patterned with copper squares and dip-coated to leave molten solder on the target pads. The components to be assembled were coated with gold on one side and a small gold contact was patterned on the other. They were gently tumbled in a heated water vial containing the cylindrical substrate. One thousand six hundred silicon cube LEDs were assembled on an area of 5 cm^2 in less than 3 minutes, achieving an assembly yield of 98%. To bring about electrical connectivity, the small top contacts of the assembled LEDs were solder coated by

another dip coating step, and then a flexible transparent thin-film substrate with patterned electrical circuits and metal interconnection lines was manually aligned and mounted on top using a procedure similar to flip-chip bonding. In later years, this group, including Wei Zheng and Jaehoon Chung, demonstrated many more applications based on this molten solder approach, including flip-chip LED assembly with unique three-dimensional contact pad registration, [45] three dimensional LED packaging with complementary metal oxide semiconductor (CMOS) integrated circuits, [46] and programmable self-assembly of multi-coloured LED display segments. [27]

In 2006, Stauth and Parvis demonstrated a hybrid approach to molten solder driven assembly that also employed gravity driven geometrical shape recognition for programmability of heterogeneous silicon parts. [22] Different electrical components, such as single crystal silicon field-effect transistors and diffusion resistors, with sizes in the range of 100 μm were self-assembled onto flexible plastic substrates patterned with recessed binding sites containing multiple gold pads at the bottom. Geometric shapes patterned into a thick SU-8 photoresist coating revealed the recessed binding sites containing multiple patterned gold pads that were later dip-coated with solder. By using different shapes (such as circular, triangular, or rectangular) for different parts and binding sites, selective assembly of the different parts onto programmed locations was achieved through sequential batches. As can be seen from Figure 2.4, the substrate was immersed and tilted in a warm, acidic solution that melted the solder and continuously removed its superficial oxide layers. Laminar fluid flow and controlled agitation of the substrate facilitated the sliding of the devices down and across the substrate, as well as the removed many incorrectly bound devices. In the initial approach, an assembly yield of 97% was achieved with 10,000 parts over a 25 minute period. [22] A recycling apparatus was later developed to automate the process, allowing unbound devices to repeatedly undergo the assembly process until very high yields could be reached. [47] This approach was used to assemble circular AlGaAs-based coloured LEDs onto silicon and glass substrates. [48] While the yield for the assembly step reached as high as 97% within 5 minutes, an overall functional yield of only 62% was reached due to electrical interconnect failure mainly caused by degradation of the solder bumps in the hot acidic environment.

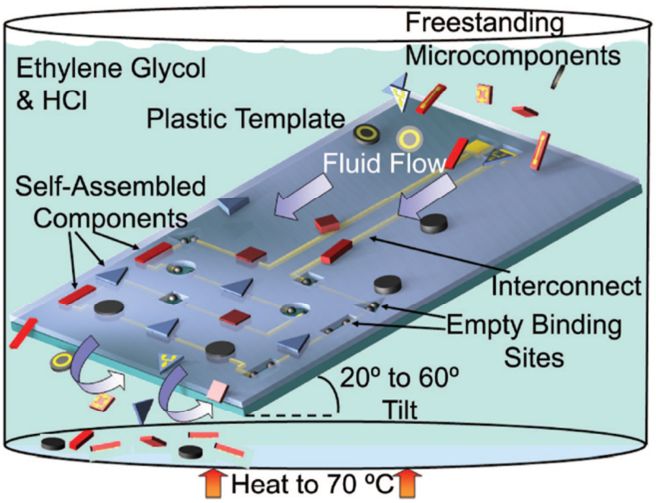

Figure 2.4: A hybrid approach to programmable, stochastic, fluidic self-assembly of microparts developed by Stauth *et al*. This approach is driven by molten solder capillary forces, gravity, and shape matching. [22]

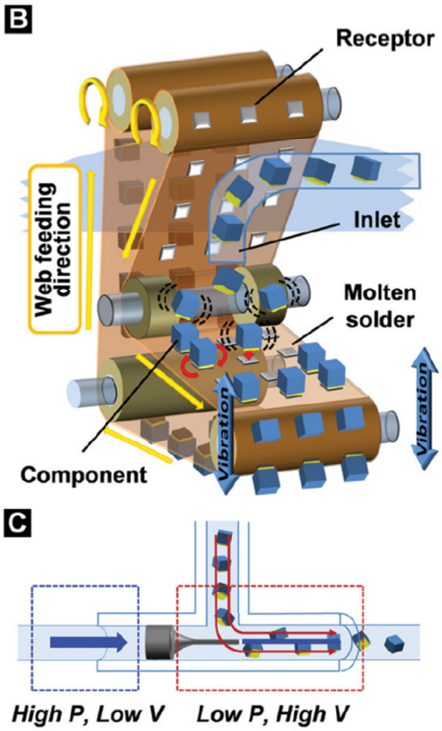

Figure 2.5: (B) Schematic depicting the details of the automated reel-to-reel molten solder driven fluidic self-assembly machine developed by Park, Jacobs, *et al*. (C) Schematic illustrating the jet pump principle used to achieve recirculation of the chips. [49]

In 2014, the Heiko O. Jacobs group further pushed the industry-scalable capabilities of this molten solder driven fluidic self-assembly method by developing an automated machine-like process involving a conveyer belt/reel-to-reel type assembly approach, as can be seen from Figure 2.5. [49] 500 µm wide silicon components were gold coated on one side and fabricated from a 200 µm thick substrate. An inlet dropped the components onto a flexible substrate coated with molten solder pads, where they were assembled by molten solder capillary forces. The conveyor belt then dropped off and the unbound components were released off of the substrate and back into the solution by vibrations in the conveyor belt, along with gravitational forces. There the components were recirculated back to the inlet by a jet pump based circulation system that was designed to leave them undamaged. With a 2.5 cm wide target substrate, this new mechanism was able to assemble 500 µm wide square shaped dies at a rate of 150,000

chips/hour (a factor of 2x better than current robotic pick-and-place machines) at a yield of 99.8%. This industry-capable yield process was also demonstrated to manufacture large area lighting panels incorporating distributed inorganic LEDs. [49]

2.2.2.2. Capillary Forces: Liquid-Liquid Interface Driven

In a recent paper from Robert Knuesel and Heiko O. Jacobs, a new self-assembly mechanism was described that combined molten solder capillary effect forces with the surface tension forces between liquid interfaces to create a novel three-step energy cascade self-assembly technique in which the free energy of the system decreases with each step. This new approach demonstrated improved performance in terms of throughput (62,500 chips/45 s), positional accuracy (0.9 μm, 0.14°), and minimized device size (20-60 μm), beating assembly speeds of state-of-the-art serial robotic chip assembly machines by an order of magnitude. [17] It proved to be the best performing high yield (>98%) chip-to-substrate self-assembly method of its time, eliminating the dependence on gravity and sedimentation found in similar molten solder driven high-yield assembly methods from Jacobs *et al*. [50] In previous methods, the minimum size for electronic components was traditionally limited to >100 μm because gravity-driven sedimentation was required (which is typically not very effective with smaller components). This so-called *energy cascade* technique, however, did not employ gravitational forces, so much smaller components (20-60 μm) could be assembled.

Using a similar procedure to the one described in Chapter 5.1.2 of this thesis, 60 μm wide gold-coated silicon microchips were fabricated from a SOI wafer and then released into solution by buffered oxide etch (BOE) underetching. SAMs played an important part in this work as they were used on both the gold and silicon sides of the microtiles to make one side hydrophilic (Au) and one side hydrophobic (Si) before the microtiles were dried onto a glass substrate by a dehydration bake. As can be seen from Figure 2.6, the self-assembly takes place in a conveyer belt-like fashion at a triple interface between silicone oil, water, and a penetrating solder-patterned substrate that was dipped and pulled upward

through the interface. The components were positioned and transferred onto the solder-coated target substrate via a stepwise reduction of the interfacial energies.

First, the components were pulled through an oil-water interface where they were removed from the glass substrate and remained suspended at the interface. Once in the oil-water interface, the hydrophilic/hydrophobic nature of the SAMs on either side of the microtiles caused them to reorient themselves within the interface to face the appropriate direction (gold side facing water). The temperature of the bath water was heated to 95°C so that solder pads on the target substrate became molten and the pH was lowered to ~2 so that the surface of the molten solder could be constantly cleaned of oxide layers. The third interfacial energy minimization step occurred when the target substrate was vertically slid though the oil-water interface. Cyclical upward and downward translations yielded a dynamic contact angle. During upward motion, the water layer receded across the substrate and became sufficiently thin, which pushed the microtiles into direct contact with the substrate so that the gold faces could connect with the molten solder in a well-aligned manner favored by 400 mJ/m^2. [17] Conversely, during the downward motion, the fluid meniscus became inverted and the microtiles were repelled from the substrate, removing any unassembled or incorrectly bound components. A site-filling ratio of up to 90% could be achieved by a single pass, and 100% site saturation was typically achieved after 5-10 passes.

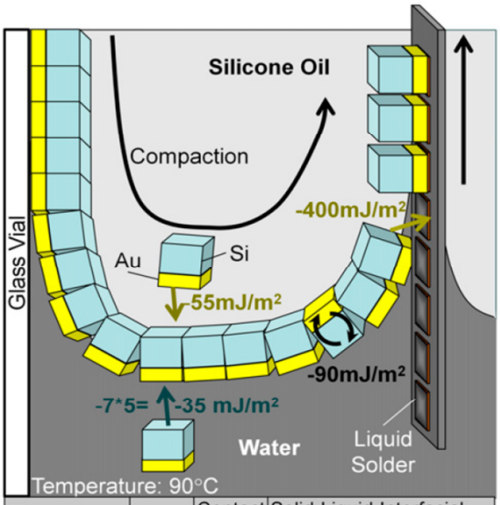

Solid	Liquid	Contact Angle	Solid-Liquid-Interfacial-Energies $\gamma_S - \gamma_L \cos(\theta)$	
Au+MUA (hydrophilic)	Oil	30°	γ_{MUA-Au} - 17 mJ/m²	-55
Au+MUA (hydrophilic)	Water	5°	γ_{MUA-Au} - 72 mJ/m²	-400
Au+MUA (hydrophilic)	Solder	20°	γ_{MUA-Au} - 470 mJ/m²	
Si+GPTMS (hydrophobic)	Water	80°	$\gamma_{Z6040-Si}$ - 13 mJ/m²	-7
Si+GPTMS (hydrophobic)	Oil	2°	$\gamma_{Z6040-Si}$ - 20 mJ/m²	

Figure 2.6: Illustration of surface tension-directed self-assembly of silicon microchips (60x60x20 µm) at a liquid-liquid-solid interface employing an energy cascade to: move components from suspension to the oil-water interface, pre-orient the components within the interface, and assemble the components onto molten solder (95°C) pads through dipping. [17]

Experiments were also conducted with receiving solder domains that had larger dimensions than the microtiles. [51] This produced electrically connected domains of monocrystalline silicon microtiles. Defect-free self-tiling mosaics were demonstrated when the side length of the domain was chosen to be an integer multiple of the microtile size. An assembly rate of 10,000 microtiles per minute was demonstration with less than 3% vacancies in a tiled mosaic of 20 μm wide square microtiles. Triangular mosaics were also demonstrated, and the minimum tile size for this technique was shown to be reducible down to 3 μm^2. [51]

Another significant approach to fluidic self-assembly based on hydrophilic/hydrophobic forces was demonstrated with 500 μm wide photovoltaic microchips by Lavin *et al*. in 2010. [52] These GaAs chips were gold coated on one side and two SAMs were used to control wettability. An octadecane thiol SAM was formed on the gold side to make it hydrophobic, and a trichlorooctadecylsilane SAM was formed on the GaAs side to make it hydrophilic. A glass target substrate was made superhydrophic by silylation and patterned by UV exposure so that hydrophilic target sites could be made. This substrate was covered by a thin layer of water and then a thin layer of toluene and then the chips were added. From the hydrophobic/hydrophilic interactions, the chips oriented themselves at the water-toluene interface above the substrate so that the GaAs side faced down. The tolune layer was then removed, leaving the chips floating on the water layer. When the water was slowly removed by evaporation, it would form into droplets only coating the hydrophilic regions of the target substrate because of its wetting characteristics. This caused the chips to self-assemble only onto the hydrophilic regions and not the superhydrophic regions.

2.2.2.3. Hybrid Microhandling: Robotically Assisted Self-Alignment

The recently proposed method of hybrid microhandling couples the complementary advantages of both capillary force driven and robotic pick-and-place assembly by using a robotic arm to bring the components into close proximity with the fluid-coated receptor sites, after which they are released and allowed to self-align into place by the capillary forces of the droplet. [16] If only rough (~50 μm) alignment

is required, modern robotic pick-and-place machines can serially place parts at a rate of 100,000 parts per hour, and this can be done even faster if direct mechanical contact is not required to release the parts. With the hybrid microhandling method, contact between the component and the fluid-coated receptor site may be enough to completely release to part from the robotic arm, as the capillary force can typically be made larger than the adhesion force between the robotic gripper and the part. A partial parallelization of the process can actually be made if the gripper releases the die as soon as partial overlap and contact is made between the die and the fluid coating of the receptor site. The robotic arm can then move to fetch the next die while the previous is self-aligning by capillary forces. The Quan Zhou group from Aalto University, Finland first demonstrated the approach using a programmable translational stage with the target substrate mounted on it and a microscope mounted above the stage. [16] A piezoelectric diaphragm dispenser was also mounted above the stage and used to drop small droplets of water onto each target pad. Then a tweezer-type robotic microgripper was used to repeatedly grab and drop silicon microtile dies onto the substrate as the translational staged moved through the pattern, as illustrated in Figure 2.7. Programmed assembly of various sized dies ranging from 100 µm wide to 300 µm was successfully demonstrated on a common substrate with an alignment yield of 99.5%. A high-speed camera was used to show that the self-alignment typically finished in a range of time between 50 and 500 ms, with the time range usually depending on how well the die was initially placed.

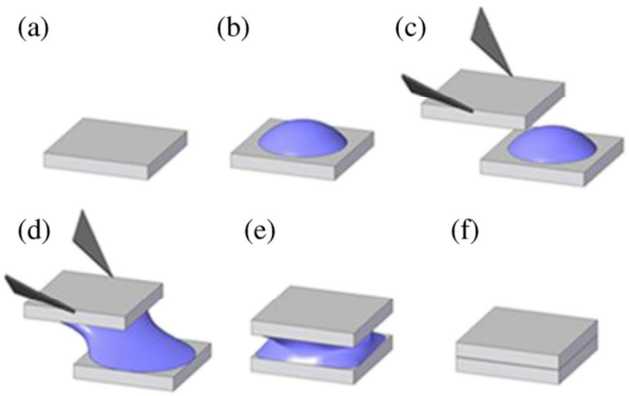

Figure 2.7: Stepwise schematic of the robotically-assisted self-alignment procedure of hybrid microassembly, as originally proposed by Sariola, Zhou, *et al*. [56]

This fast and well-aligned approach was later adapted for larger 730 µm x 730 µm RFID dies with four-pad contact pad patterns on the bottom. [53] This allowed for four different die-to-substrate electrical connections to be made with each die. This approach could be expanded upon to include many more contacts under larger dies. The fact that this form of capillary force driven assembly could be performed

in air with a fluidic medium such as water meant that the fluid could very easily be eliminated by evaporation, and no further rinsing was necessary. [54] By introducing raised target pads and a water misting apparatus, the droplet-dispensing step could be removed as well. [55] Using this mist technique, the aligned stacking of multiple 200 µm x 200 µm SU-8 chips on top of one another was demonstrated. Confinement of the droplet was further improved by introducing fluoropolymer coated target pads protruding out of a rough superhydrophobic substrate surface. [54] The substrate surface was made from black silicon, a nanostructured silicon surface that traps all light inside nanoscale cavities so that the rough surface appears black. The more accurate droplet confinement and larger contact angle provided by this led to improved die alignment in the capillary force driven self-alignment process. A recent study also demonstrated that by increasing the height of the target pad that the droplet was placed on from 70 nm up to 1 µm, consistent improvements in the yield of well-aligned dies were made with each height increase. [56]

2.2.3. Electric Field Driven

Tien *et al*. first demonstrated the use of electrostatic forces to self-assemble microstructures in 1997. [57] They formed charged SAMs on 10 µm wide gold disks to drive the assembly of those disks onto patterned locations functionalized with SAMs of the opposite charge. One year later Böhringer *et al*. demonstrated the first attempt at systematically designing electrostatic potential fields for the parallel assembly of millimeter scale electronic components onto patterned gold electrodes. [58] This assembly was performed in a dry environment, using mechanical vibrations to help the parts overcome friction barriers and eventually reach the target electrostatic traps. In 2002, Lee *et al*. used charged SAMs of 2-mercaptoethanesulfonic acid sodium salt to induce a negative charge onto 4 µm wide gold-coated silicon chips. [59] A 1 V potential was then applied to induce positive

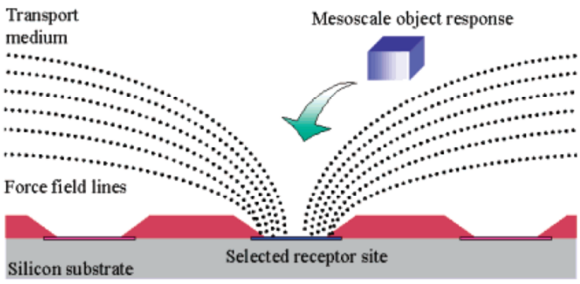

Figure 2.8: Schematic illustration of electric field driven self-assembly. Electrical biasing of the selected receptor site induces fluidic transport of the component onto the desired location. [28]

charge in gold electrodes patterned on a substrate and this induced the chips to self-assemble at a low yield. As can be seen in Figure 2.8, O'Riordan *et al*. used negatively charged beads attached to 50 μm wide GaAs-based LEDs to induce a similar low yield assembly of the LEDs onto charged electrodes. [28] A programmable array of electrodes was used so that specific receptor sites could be chosen for the LEDs to be assembled onto during each run. The integration was completed by evaporating the transport medium and forming metal contacts to the LEDs by solder reflow.

2.2.3.1. Electrophoresis Driven

Electrophoresis is a phenomenon that can be induced by an electric field in liquids containing charged particles. [13] An electric field can induce the motion of charged particles relative to the fluid due to the formation of a charged interface. In 2000, Edman *et al*. used a variant of electrophoresis called electroosmosis to assembled 20 μm wide InGaAs LEDs onto patterned electrodes on a silicon substrate. [60] Although parallelization of this process may have been possible, the initial demonstration was done one chip at a time by placing the chip in a fluid-filled channel on the substrate, inducing electroosmotic flow, and observing it move down the channel towards the target site. Once the LED chip was above the target site, the electroosmotic flow was briefly reversed, forcing the chip into contact with the target site, which consisted of a pair of electrodes. The fluid was then removed and electrical contact was made by solder reflow. Mayer *et al*. later patented a similar technique that used electrophoretic flow to position InP-based diode devices over a substrate and then an electrostatic energy minimization technique was employed to align them into position. [61]

As demonstrated by Lee *et al*., dielectrophoresis has also been used to assemble microscale devices. [62] Unlike electrophoresis, which exclusively acts on charged bodies, dielectrophoresis affects both charged and unchanged bodies. Positive dielectrophoresis and electrothermal effects were used to serially direct the assembly of 10 μm wide silicon resistors onto patterned sites on a target substrate. The resistors contained a pairs of gold-coated electrodes at either end, about the same distance apart as the gap between the long target electrodes. When a sinusoidal AC signal with 10 V and 10 MHz was applied using micromanipulator probes, the resistors in solution were directed to move to between the two long

surface electrodes, as this region contained the largest gradient of the AC field. The same group later used this technique to assemble 15 μm wide three-terminal MOSFET device. [63] Thiol-terminated SAMs on the gold-coated substrate electrodes were also employed to provide additional stability and yield. The thiol ends of these SAMs helped with the immobilization and alignment of the devices because they bonded with gold-coated electrodes patterned on the bottoms of the devices.

2.2.4. Magnetic Field Driven

The magnetic field driven self-assembly of microscale devices was first proposed in 2002 by Clifton Fonstad Jr., who envisioned the approach as a suitable variation of fluidic self-assembly for addressing the integration of III-V compound semiconductor devices. [64] Shet *et al*. expanded upon the initial idea by introducing a long-ranged magnetic field source at the backside of the target substrate, along with recessed target sites that had their own short-range magnets at the bottom. [65] The long-range magnetic force drew the components (coated with a soft magnetic film) close to the target sites so that they would fall into the recessed locations, becoming locked in place by the short-range magnets. The substrate was then inverted to remove any excess unassembled components and the process was repeated until all of the sites were filled. In 2008, Shetye *et al*. experimentally demonstrated the magnetically driven selective self-assembly of 1 mm x 1 mm silicon dies onto target substrate sites in a dry environment. [66] Powder-based samarium-cobalt permanent magnets were embedded both in the chips and in the target substrate, which contained no other guiding template. The substrate was positioned upside down 10 mm above a glass container containing the silicon dies (five times as many dies as target sites) and the glass container was connected to an electromechanical shaker, which was capable of launching the dies into the target substrate. For a 4x4 array of target sites on the target substrate, an average 98.7% yield of attachment was demonstrated for 7-second assembly runs. Vibration of the substrate afterwards was able to induce alignment of the dies into position, as can be seen from Figure 2.9.

In 2011, Morris *et al*. demonstrated a technique that combined the use of capillary forces and magnetic forces to self-assemble 280 µm wide silicon dies containing permanent magnets onto dip-coated molten solder target sites. The target sites also contained permanent magnets underneath them. [67] By simple flow of the components over the target substrate, the magnetic fields helped to guide the dies into place. Using the exact same number of available dies as target sites (a rare occurrence in the field of fluidic self-assembly), an assembly yield of 8% was obtained. When the experiment was performed using the same procedure but without the magnets, an assembly yield of only 0.1% was obtained, demonstrating the effect of the magnets. Another recent demonstration from Park *et al*. used the combined effects of magnetic fields and hydrophilic/hydrophobic forces to induce the assembly of 2 mm wide tiles. [68] A substrate was patterned with neodymium iron boron magnets under each target site, and the tiles were patterned with a 10 µm thick nickel coating to induce magnetic attraction and proper orientation. The target sites were also coated with SAMs to induce hydrophilic/hydrophobic wetting characteristics. The tiles were floated on top of a water-air interface, and the substrate was slowly pulled upwards through the interface at a 45° angle so that the tiles would assemble onto it as it moved. The hydrophilic binding sites against the hydrophobic background of the substrate created a curved meniscus along the substrate that helped the tiles approach the substrate at a favorable angle for binding.

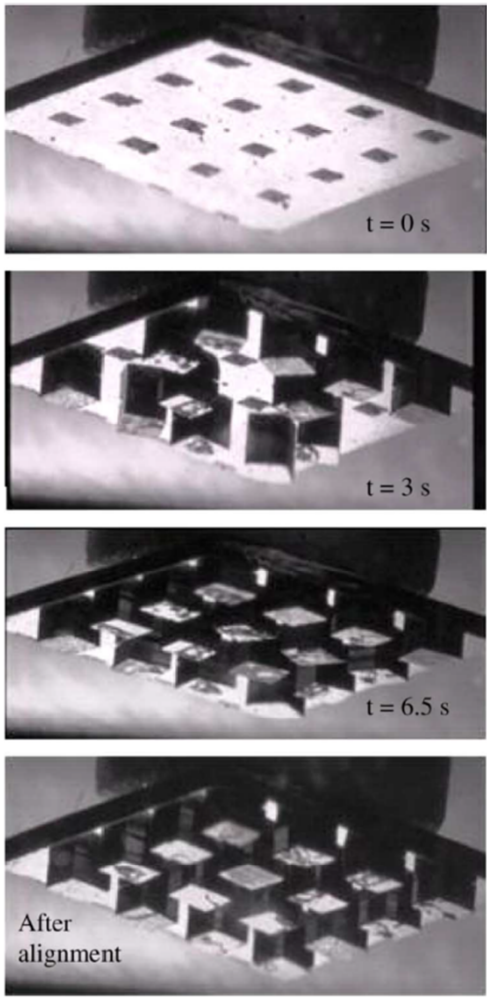

Figure 2.9: Snapshot views of the magnetic field driven self-assembly process developed by Shetye *et al*. The final shot demonstrates how final alignment of the silicon dies can be induced by vibration of the substrate. [66]

2.2.5. DNA Driven

The first demonstration of self-assembly based on DNA interactions was performed by Mirkin et al. in 1996 with 13 nm diameter gold nanoparticles. [69] Only two years later, Esener *et al.* predicted that DNA would be used for the integration of heterogeneous electronic and optoelectronic components onto a common substrate. [9] Esener proposed that the inherent base-pair coding property of DNA and synthesizability could make it a very powerful tool for nanofabrication, and it could function as "a highly selective glue". A later study by the same group demonstrated the selective self-assembly of single-stranded DNA coated nanoparticles with diameters of 110 nm and 870 nm. [70] Covalently bonded SAMs were used for the DNA attachment, and binding selectively ratios of greater than 20 were observed (functionalized surface binding as opposed to clean surface). Calculations showed that at most 350 and 4200 DNA strands respectively were involved in the binding of the small and large particles.

Although there have been a large number of studies based on using DNA to drive the self-assembly of nanoscale devices such as nanoparticles, nanorods, or carbon nanotubes, [71], [72] a few demonstrations have also shown the possibilities of DNA being used to self-assemble microscale devices. Most notably, a research group from Purdue University consisting of authors Bashir, McNally, and Lee proposed and attempted the die-to-substrate self-assembly of microscale silicon integrated circuits. [73] Along with this, Bashir *et al.* also proposed a very clever technique for releasing silicon devices fabricated from SOI devices into solution. Their method involved underetching a sacrificial buffered oxide layer under each silicon device so that only a thin pillar held the devices onto the substrate. Then, the devices were released into solution by bath ultrasonication, which broke the SiO_2 pillars. They also proposed that after the silicon "islands" were released into solution, they could functionalize them with a SAM ending with a single-stranded DNA sequence (oligonucleotide). On a target substrate, they functionalized target gold pads with a similar SAM containing the complementary oligonucleotide. [73] This fabrication technique and the proposed mechanism of DNA driven die-to-substrate self-assembly are both shown in Figure 2.10. Both the sonication release method and the process flow are direct inspirations for the experimental methods described in Chapters 5 and 6 of this thesis.

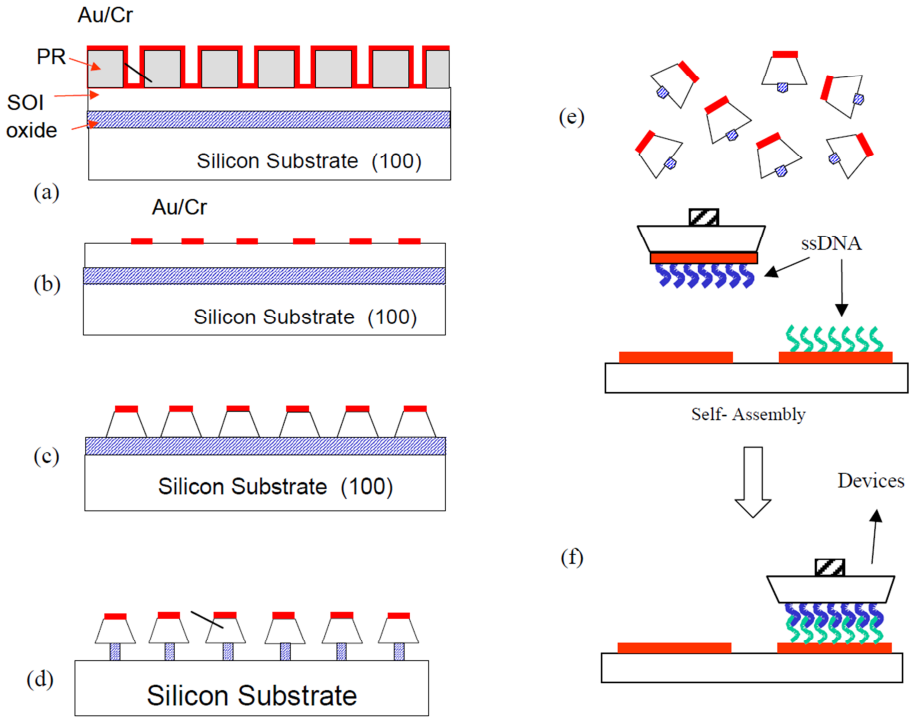

Figure 2.10: Proposed process flow for fabrication and release of silicon islands by sonication and then self-assembly driven by single-stranded DNA, as proposed by Bashir *et al*. The process flow goes as follows: (a) pattern SOI substrate with photoresist and deposit Au/Cr, (b) pattern Au/Cr pads by lift-off (c) etch silicon device layer down to buried oxide layer by potassium hydroxide (KOH) etching, (d) underetch buried oxide layer to leave only narrow pillars holding the tiles onto the handle substrate, (e) release silicon islands into solution by bath ultrasonicating to break the oxide pillars, (f) functionalize the gold side of the silicon islands and gold pads on a target substrate with complementary single-stranded DNA SAMs and induce self-assembly of the islands onto the target substrate. [73]

After proposing this approach in theory, a later study from the group demonstrated that 8.5 µm wide silicon islands could be successfully released into solution by the ultrasonication technique with a 99% yield. [74] The islands were functionalized with two complementary SAMs of single-stranded DNA on their gold faces and an initial demonstration showed pairs of the islands self-assembling together to form duplexes, as shown in Figure 2.11. Attempts at self-assembling the functionalized silicon islands onto functionalized target pads on a substrate, however, were not as successful. Estimations of the forces experienced by the 8.5 µm wide silicon islands during rinsing cycles were made, and it was concluded that the sum of the gravitational, capillary, and fluidic drag forces experienced by the islands may be larger or approximately on the same order of magnitude as the forces resulting from the DNA hybridization. [74] Later experiments involved functionalizing the same 8.5 µm wide silicon islands with charged organic SAMs and employing electric fields to induce their self-assembly. [59] These experiments

produced much larger yields. It was later concluded by Morris *et* al. that although DNA provides an excellent candidate for programmable self-assembly at the nanoscale, the provided hybridization forces may not be sufficient for the technique to be extended to the microscale domain. [6]

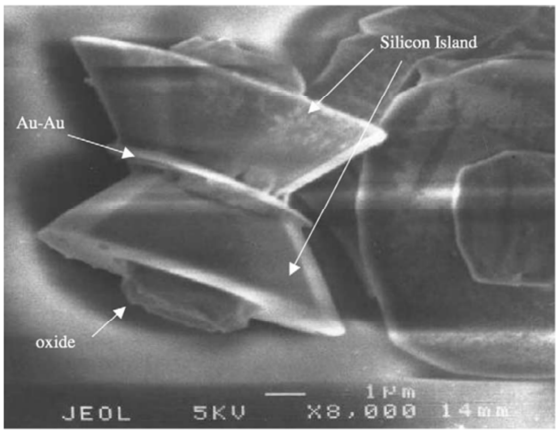

Figure 2.11: An initial demonstration of microscale DNA-driven self-assembly of silicon islands which were functionalized and assembled together to form duplexes. [74]

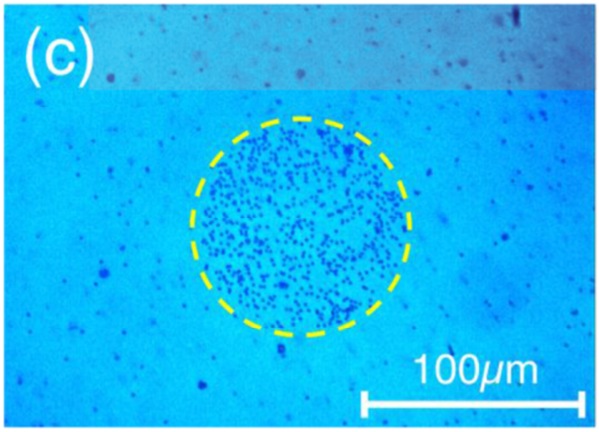

Figure 2.12: Results showing 1 μm diameter polystyrene microspheres self-assembled onto a patterned target circle using two SAMs of complementary single-stranded DNA. [76]

Kusakabe *et al*. developed a novel approach for DNA self-assembly that employed DNA strands of different lengths corresponding to different hybridization temperatures to achieve a layer-by-layer assembly. [75] Different types of synthesized single-stranded DNA with different melting temperatures were used to control the sequence of self-assembly by controlling the temperature of the assembly fluid. Promising results were observed for 60 nm wide gold nanoparticles self-assembling onto a gold-coated substrate, but when the approach was attempted with 5 μm wide silicon micro components, the low yield assembly onto the substrate was not confirmed to be driven by DNA. Recent experiments from Yasuda *et al*. attempted the selective self-assembly of polystyrene microspheres ranging in diameter from 1 μm to 6 μm onto a glass substrate. [76] SAMs were employed to functionalize the microspheres with an oligonucleotide-terminated monolayer and the target sites were functionalized with a complementary oligonucleotide SAM. Although successful assembly was demonstrated, observed yields were relatively low. This can be seen from Figure 2.12, which shows ~500 of the 10 μm diameter microspheres assembled onto a 100 μm circular patterned region.

2.3. Self-Assembly by Protein-Ligand Interactions

2.3.1. Overview of Proteins

Proteins are incredibly complex biological macromolecules that are made from chains of amino acid residues. [77] They are synthesized in the ribosomes of cells from 20 common amino acids that are coded for in the DNA of an organism. The specific linear sequence of these amino acids is known as the protein's primary structure, and it is the most common feature for differentiating between proteins. The amino acid sequence usually dictates how the protein will fold into a specific three-dimensional structure. The avidin protein, for example, is formed from four amino acid subunits, and each of these contains a 128 amino acid sequence that can bind a biotin molecule. [78] There are three other levels of structure (secondary, tertiary, and quaternary) formulated to describe the complex structure of the protein. Together with the specific amino acid sequence, these four levels of structure determine the protein's function. Proteins require such a great level of complexity so that they can perform specific tasks such as catalyzing metabolic reactions, transporting molecules, replicating DNA, or, as exploited in this research, binding specific ligands. [77]

2.3.2. Protein-Ligand Driven Self-Assembly of Micro- and Nano-scale Devices

In similar fashion to DNA driven self-assembly, protein-ligand driven self-assembly has previously only been successful at high yields at the nanoscale. An early proposal on the subject in 2000 suggested that genetically engineered polypeptides, defined as a sequence of amino acids designed to selectively bind to inorganic surfaces, could be used for the functional assembly of nanostructures. [79] In 2004, Arakani *et al*. used SAMs to attach biotin to a patterned silicon/SiO_2 substrate and to attach streptavidin, a biotin-binding protein purified from the bacterium *Streptomyces avidinii*, to magnetic nanoparticles. [80] A 3-aminopropyltriethoxysilane SAM was initially formed on the SiO_2, and then biotin was introduced as the functional group by using a cross-linker of Sulfo-NHS-LC-LC-biotin (where Sulfo-NHS denotes *N*-hydroxysulfosuccinimide and LC denotes "long chain", a seven atom spacer group). Verified by SEM,

the group successfully demonstrated the selective self-assembly of 200 nm wide magnetic nanoparticles onto the substrate.

In 2007, Pierrat *et al*. further extended this approach of streptavidin-biotin protein driven self-assembly by successfully assembling biotinylated gold nanorods (140 nm x 60 nm) onto patterned locations on a glass substrate that were coated with streptavidin. [81] As an initial demonstration, and to determine the best procedure for biotinylating the nanorods, 10 nm wide streptavidin coated gold nanoparticles were successfully self-assembled onto the nanorods in a controlled experiment where the biotinylation reagent concentration was varied. Then the group self-assembled the gold nanorods onto a patterned streptavidin coated substrate area with a density of 150 rods per 100 μm^2 and a 5:1 area selectivity over the uncoated part of the substrate. [81] To functionalize the gold nanorods with a biotin SAM, a thiol reactive biotin derivative called Pierce EZ-Link Biotin HPDP was used. To pattern and coat the glass surface with streptavidin, it was first amino functionalized and then a drop of NHS-terminated biotin-polyethylene glycol (PEG) was added and rinsed off with water after 1 hour. This formed a biotin-terminated SAM over the area of the drop. The substrate was then incubated in methoxy-PEG-succinimidyl propionate to form a SAM on the rest of the substrate area, passivating it so that the streptavidin molecules added later do not stick. The substrate was then rinsed, dried, and then incubated in a 1 mg/mL streptavidin solution to place streptavidin at the end of the SAM.

Because the avidin-biotin/streptavidin-biotin combination has the strongest known protein-ligand interaction, it is typically the most popular combination used to drive self-assembly. However, an issue with the avidin-biotin combination is that it cannot be used for in vivo biomedical applications such as nanoparticle therapy or drug delivery. [25] This is because biotin is widely present in the blood and tissue of most mammals and avidin/streptavidin introduced into the body would bind this biotin and potentially interfere with many natural processes. Nikitin *et al*. used two proteins from *Bacillus amyloliquefaciens* called barnase and barstar to successfully self-assemble microspheres to each other in clusters using the barnase-barstar protein-protein interaction. [25] Together, the two proteins have a very strong non-covalent protein-protein binding system that is only slightly weaker than the avidin-biotin interaction. The

successful particle aggregation was performed with magnetic silica and carboxyl beads ranging in diameter from 0.5 to 3 µm.

In an experiment similar to the one found in Chapter 4 of this thesis, McNally *et al*. successfully self-assembled avidin coated polystyrene microbeads (0.8 µm in diameter) onto a patterned gold substrate functionalized with a double-stranded DNA SAM that contained biotin molecules terminal functional groups. [82] This same avidin-biotin mechanism was also used to self-assemble 8.5 µm wide silicon islands (gold-coated and functionalized on one side) to each other to form duplexes. One silicon island was functionalized with a DNA-biotin chain (biotin functional group) while the other silicon island was functionalized with a DNA-biotin-avidin chain (avidin functional group). An 82% yield of duplexes was achieved with this approach. Further attempts to self-assemble the 8.5 µm wide silicon islands onto patterned and functionalized locations on a substrate proved to have insignificant yield. [82] A schematic of the proposed avidin-biotin die-to-substrate self-assembly mechanism is shown in Figure 2.13.

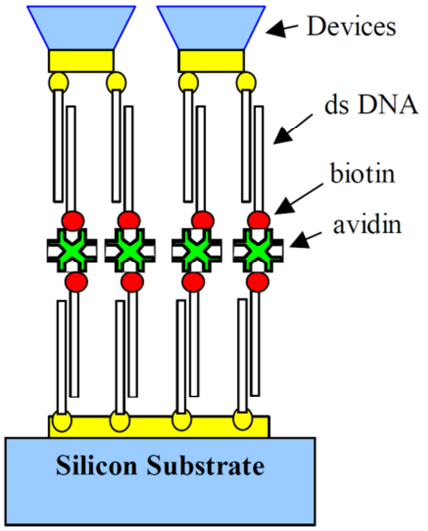

Figure 2.13: Schematic illustration of proposed self-assembly mechanism where biotinylated double-stranded DNA SAMs are functionalized on both the substrate and the devices and avidin is used as the linking element. [82]

2.3.3. The Avidin-Biotin Interaction

Avidin is a tetrameric glycoprotein that is produced in the oviducts of birds, reptiles, and amphibians and found in their egg whites. [83] It was discovered in 1941 by Esmond E. Snell when he noticed that chicks fed an exclusive diet of egg whites developed a severe dermatitis. [84] Despite the availability of biotin in their diet, it was found that they were deficient of the B-vitamin biotin, and the condition was cured by subsequent administration of biotin. Like its bacterial analogue streptavidin (from the bacterium *Streptomyces avidinii*), avidin is believed to act as an antibacterial agent in egg whites by scavenging free biotin from the environment and thereby making it unavailable to bacteria. [85] The

streptavidin protein is believed to be produced by the *Streptomyces avidinii* bacterium to inhibit the growth of competing bacteria. [86] A third biotin-binding protein, NeutrAvidin, is also commercially available, but avidin extracted from egg whites is typically the most cost-efficient form available.

Avidin is very well known for its strong binding interaction with biotin. The bond formation between avidin and biotin occurs very rapidly, and is almost irreversible once formed. It can withstand extremes in pH, temperature, organic solvents, and other denaturing agents without breaking down. [87] For most practical purposes in biology, the bonding between avidin is generally thought to be irreversible, [88] although temperature cycles above 70°C have been shown to break and reform the bond in nonionic aqueous solutions. [89] Avidin is made up of four identical polypeptide chains, and a single avidin protein can bind up to four biotin molecules at a time with a high degree of affinity and specificity. A single avidin protein is roughly cubic in shape, with a molecular weight of 68 kDa and molecular dimensions of approximately 4.0 x 5.0 x 5.5 nm^3. [83] The biotin binding sites are located in two pairs on opposite faces of the cubic molecule. [90] Avidin and biotin have one of the strongest protein-ligand binding interactions known to date, with a dissociation constant K_d near 10^{-15} M. [8] Relying on multiple interactions such as sulfur-threonine binding, carboxyl-peptide hydrogen bonding, and a network of hydrogen bridges between the biotin ureido group and amino acid residues in the avidin, [91] the affinity of this binding interaction is equivalent to 21 kcal/mol. [92] This is a significant strength because, although it is a non-covalent interaction, it is on a similar scale to many covalent interactions. For example, the semi-covalent gold-sulfur thiolate bond, which is used numerous times in this work to form SAMs on gold, has a binding energy of 44 kcal/mol. [93]

Biotin, a vitamin also known as Vitamin H, Vitamin B7, or Coenzyme R, is present in small amounts in all eukaryotic cells and is critical for a number of biological processes including cell growth, the metabolism of carbohydrates, and the citric acid cycle. [94] As can be seen from Figure 2.14, the biotin molecule has a valeric acid side chain, which can be easily derivatized to incorporate a variety of reactive groups; these groups can be used to tag the biotin molecule onto a wide range of other molecules. [95], [96] When the valeric acid side chain is used, the functionality, and more specifically, the avidin-binding

capabilities, of the biotin molecule are typically not impaired. Since the avidin protein has four biotin-binding sites, it can also be chemically modified and attached to other molecules without losing its ability to bind biotin. Biotin is a relatively stable and small molecule (244.31 Da), so when it is tagged onto other molecules or macromolecules, it typically does not affect their biological activity. [97] Since the avidin protein can not only bind to biotin, but also to biotin-tagged molecules, macromolecules or, in the case of this research, biotin-tagged microscale devices, the avidin-biotin system has a large range of applications and has been widely used in biochemical, biomedical, and biotechnological research for many years. [98]

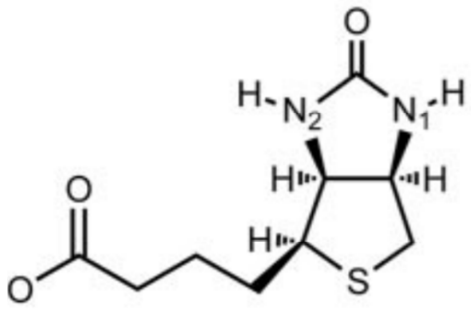

Figure 2.14: Molecular structure of the biotin molecule. The valeric acid side chain on the left side is commonly used to incorporate various reactive groups that can attach the biotin molecule onto other molecules without impairing the functionality or avidin-binding capability of the biotin molecule itself. [95]

Biotin can be very easily be tagged on to many molecules without interfering with their functionality. Therefore, it is very commonly used in research to label biomolecules such as proteins, lipids, or DNA, for specific detection in the future via the avidin-biotin interaction. The avidin-biotin system has been effectively used in the following major laboratory methods: protein detection, nucleic acid detection, immunoprecipitation, and pull-down assays. [99] Protein detection methods such as immunohistochemistry, Western Blotting, and enzyme-linked immunosorbent assays (ELISA) are commonly used to monitor protein purification, production, and expression levels, while nucleic acid detection methods such as Northern and Southern blotting are commonly used for determining the presence, abundance, or sequence changes in specific polynucleotides. Immunoprecipitation is a method of isolating and concentrating a particular protein from a sample of many different proteins. It can be greatly simplified and enhanced by using avidin-biotin strategies. Finally, pull-down assays are used to determine the interaction of two or more proteins by using a "bait" protein to recover additional interacting "prey" proteins. [99] Some other industry-standard applications that employ the avidin-biotin

system include cell-surface labeling, fluorescence-activated cell sorting (FACS), electrophoretic mobility shift assays (EMSA), scintillation proximity assays (SPA), amplified luminescence proximity homogeneous assays (AlphaScreen), surface plasmon resonance assays (SPR), and many lab-on-a-chip systems. [96], [100]

The avidin-biotin system was actually the first protein-ligand system to be used for the purposes of immobilizing macromolecules onto solid surfaces. [101] There are numerous examples of affinity-based systems that immobilize avidin proteins onto solid target surfaces and then biotinylate a macromolecule of interest so that it can also be immobilized onto the surface via the avidin-biotin interaction. This immobilization can be used for many purposes such as detection, capture, isolation, retrieval, or assembly. There are numerous protocols for tagging macromolecules with biotin, and virtually all biologically active compounds such as antibodies, proteins, receptors, cells, phages, enzymes, inhibitors, hormones, nucleic acids, drugs, and toxins have demonstrated the ability to be biotinylated for immobilization purposes. [101], [102] Common surfaces that avidin proteins can be easily immobilized onto include Sepharose and plastic surfaces such as petri dishes. With the use of self-assembled monolayers, however, avidin can be immobilized onto a variety of surfaces such as metals, semiconductors, insulators, and organic surfaces. [101] The work described in this thesis is very similar in concept to the well-explored technique of biotinylating a large molecule and then immobilizing it onto a solid surface using interactions with avidin proteins on that surface. This project, however, expands that concept to a much larger scale of components being immobilized.

2.4. Self-Assembled Monolayers

Self-assembled monolayers (SAMs) are the ordered, densely packed organic assemblies formed spontaneously on solid surfaces by adsorption of molecular constituents from the solution or gas phase. [103] They tend to readily form on the surfaces of bare metals and metal oxides because the SAM adsorbates lower the free energy of the interface between the metal/metal oxide and the ambient environment, and can act as a physical or electrostatic barrier to decrease the reactivity of the surface atoms. [104] SAMs are typically molecular chains made up of a head group (having a specific binding

affinity for the substrate) at one end, a tail/spacer group comprising the middle section, and a functional/terminal group at the end furthest from the substrate surface. The functional group is named so because it typically determines the surface properties of the organic interface. By specifically choosing the functional group, SAMs provide a simple, flexible, and convenient method for tailoring the interfacial properties of a solid surface. As can be seen in Figure 2.15, an illustration of the formation kinetics of a typical SAM, they can spontaneous organize themselves into well-ordered arrays and can (sometimes epitaxially) form into crystalline structures. [105] To minimize the free energy of the organic layer, the molecular chains adopt angled conformations that allow for high degrees of van der Waals interactions (and in some cases hydrogen bonds [106]) with neighbouring the molecular chains. [107]

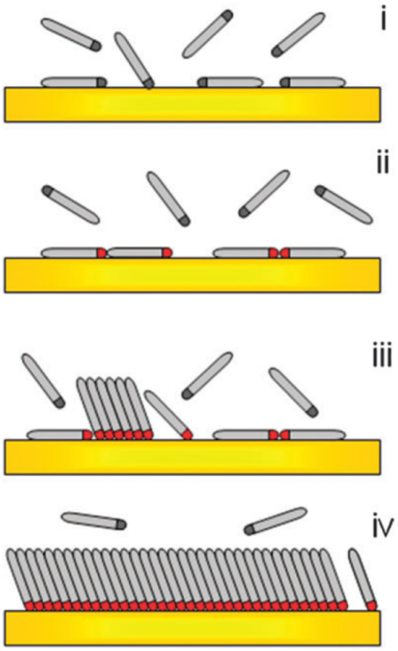

Figure 2.15: Scheme of the different steps taking place during SAM formation on a metal surface: (i) physisorption, (ii) lying down phase formation, (iii) nucleation of the standing up phase, (iv) completion of the standing up phase. [105]

The predominantly most extensively studied class of SAM is the adsorption of alkanethiols onto noble and coinage metals such as gold, silver, copper, palladium, platinum, and mercury. [103] Although thiols typically have a strong affinity to all of these noble metals, gold has been the most studied and is considered to be the standard for SAM formation. In a 2005 review by Love *et al.*, five main characteristics were outlined to explain why gold is the most popular SAM substrate: It is easy to obtain as a thin film or as a colloid, it is exceptionally easy to pattern with a combination of lithography and chemical etchant techniques, it is a reasonably inert metal (does not react with atmospheric O_2 or most chemicals) that binds thiols with a predictable high affinity, it is a commonly used substrate for many existing analytical techniques such as spectroscopies, quartz crystal microbalances, and ellipsometry, and finally, it is compatible with cells without evidence of toxicity. [103] Silver is the next most studied SAM substrate after gold, but it readily oxidizes in air and is toxic to cells in colloid form. [108], [109] Palladium

appears to be a practical alternative that demonstrates some performance characteristics superior to gold. [110]

The most common protocol for forming alkanethiol SAMs on gold is to immerse a clean substrate into a dilute (1-10 mM) ethanolic solution of thiols for 12-18 hours at room temperature. [103] From millimolar solutions, dense coverages of the surface with the adsorbates can be obtained in seconds, but a slow reorganization process maximizes the density of the molecules and minimizes the defects in the SAM. [111] Love *et al.* also outlined four main reasons for the widespread use of ethanol as a SAM-forming solvent: it solvates a large variety of molecules with varying degrees of polar character and chain length, it is inexpensive, it is available in high purity, and it has low toxicity. [103] Furthermore, electrochemistry and contact angle measurements have suggested that SAMs formed from thiol solutions in nonpolar organic solvents are typically less organized than SAMs formed in ethanol. [112], [113]

Mixed monolayer SAMs containing two or more heterogeneous molecular chains may be formed by the co-adsorption of different thiol-terminated molecular chains in solution together. [103] Using two types of chains, for example, if the two chains have similar molecular weights and chemical functionalities, then the mole fraction of the two adsorbates in the SAM will usually reflect the mole fraction of the two adsorbates in solution. However, if the molecular weights are different, then the ratio of the two chains in the mixed monolayer may turn out to be quite different from the ratio of the two adsorbates in solution. This is typically due to different binding kinetics of the two thiol adsorbates. [114] The smaller chain may be able to adsorb to the surface much quicker than the larger chain, so the ratio of the smaller chain adsorbates to the larger ones might be much greater than expected in the final mixed monolayer. As will be seen in Chapter 4.1.2 of this thesis, another way to control the ratio of adsorbates in a mixed monolayer SAM is to sequentially add the adsorbate reagents in individual steps. The first reagent is adsorbed from a low concentration solution so that there is not enough present to saturate the surface. [115] Then the second reagent is added in a later step, saturating the surface.

3. Self-Assembly of Biotin-Functionalized Gold Nanoparticles

This chapter outlines and discusses a set of experiments performed with biotin-functionalized gold nanoparticles self-assembling onto avidin-functionalized target gold pads. These experiments were performed as a proof of concept for avidin-biotin driven die-to-substrate self-assembly, as well as to develop an adequate procedure for forming a biotin-binding self-assembled monolayer (SAM) on gold with avidin as the functional group.

3.1. Experimental

3.1.1. Experimental Overview

In Chapter 5, an experimental technique is outlined for the avidin-biotin driven fluidic self-assembly of silicon microtiles onto target gold pads patterned on a silicon substrate. In that experiment, the microtiles were coated with a biotin SAM on one side and the target gold pads were coated with an avidin SAM. Prior to this microtile self-assembly experiment, preliminary experiments were conducted with biotin-functionalized gold nanoparticles to develop and verify an adequate working procedure for forming the avidin SAM on the gold pads. These preliminary experiments, outlined in this chapter, were conducted with biotin-functionalized gold nanoparticles that were purchased from a company called Cytodiagnostics.

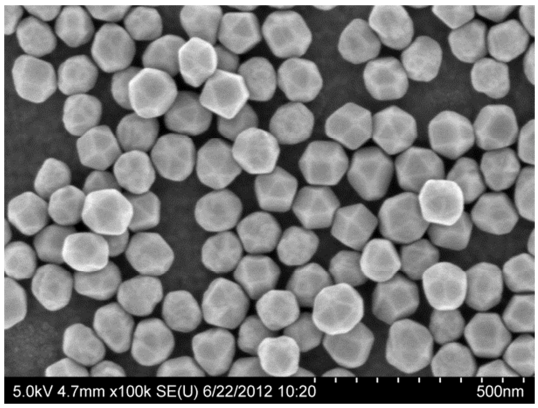

Figure 3.1: SEM image of Cytodiagnostics' 100 nm wide biotin-functionalized gold nanoparticles illustrating their platonic structure. It should be noted the nanoparticles in this image were not self-assembled using the avidin-biotin interaction, but were immobilized onto a substrate by allowing a droplet to evaporate.

Quasi-spherical biotin-functionalized nanoparticles with 100 nm average diameter were purchased and shipped pre-functionalized in aqueous solution. As can be seen from Figure 3.1, the biotinylated nanoparticles are not perfectly spherical in structure, but have a platonic structure with flat triangular or

square faces. The biotin SAM on the outer surface of the nanoparticles was specified by the manufacturers to be a mixed monolayer made up of two polyethylene glycol (PEG) chains. A longer (10 kDa) biotin-PEG-SH chain was formed on the gold nanoparticle surface in a ~1:100 ratio with a shorter (5 kDa) methoxy-PEG-SH backbone chain. PEG ligands are commonly used on gold nanoparticles because they offer extra stability to dense nanoparticle concentrations by providing a large amount of electrostatic/steric repulsion between the nanoparticles, so they are less likely to aggregate. [115]

3.1.2. Target Substrate Fabrication

Chapters 3, 4, 5, and 6 of this thesis all utilize the same target pad substrates, the fabrication procedure for which is specified in this section. The target substrates are 9 mm x 6.5 mm silicon wafer pieces which contain patterned thin-film gold pads that are deposited by evaporation and patterned by photolithography/lift-off. To fabricate these substrates, a 100 mm wide 'prime' polished silicon wafer was first piranha cleaned (H_2SO_4 and H_2O_2) and then placed in a YES™ HMDS oven to form a hexamethyldisilazane monolayer on the wafer, which made its surface hydrophobic to promote the adhesion of photoresist. Immediately after this, Waycoat® HPR-504 photoresist was spun on at 4000 revolutions per minute (RPM) for 40 seconds to form a ~1.25 μm thick layer and then soft baked at 115°C for 90 seconds to drive off the solvent and harden the resist. The wafer was allowed to rehydrate for 30 minutes prior to exposure, which was performed on an ABM™ mask aligner (Oscar). Vacuum contact was used to ensure close contact between the wafer and the photomask. The photomask pattern provided blockage of the ultraviolet light source all over the wafer, but left patterned square and rectangular shaped holes of varying sizes to be exposed. The positive photoresist was then dissolved away in those areas by developing in 354 developer. For these substrates, a typical exposure time of 2.2 seconds was used, and the substrate was subsequently developed for 17 seconds. After thorough deionized water rinsing and drying, the wafer was taken to an electron beam evaporation system in the U of A's Nanofab (Gomez). 8 nm of a chromium adhesion layer and then 35 nm of gold were deposited over the entire wafer at 10^{-7} Torr pressure. Since gold does not readily oxidize, the chromium adhesion

layer greatly improves the adhesion of the gold to the silicon substrate, which has a native oxide surface. After deposition, the gold pads on the wafer were formed by sonication lift-off of the photoresist. The wafer was ultrasonicated in an acetone bath for 30 minutes, removing any still on the substrate and leaving patterned gold pads behind on the silicon substrate. After rinsing the wafer in isopropyl alcohol (IPA) and then drying, another photoresist layer was spun onto the wafer and baked. The purpose of this protective layer was to keep the gold pads clean and undamaged while the wafer was diced into smaller substrates by a dicing saw. The protective photoresist layer was always left on the substrates right up until just before they were used, keeping them clean and protected from dirty non-cleanroom environments. Immediately prior to the chemical functionalization of the target substrate, the protective photoresist layer was rinsed away by acetone. A variety of target patterns were obtained from one wafer, including 5 μm and 25 μm wide squares, and rectangles of these widths and varying lengths. For gold nanoparticle experiments in this chapter, 25 μm wide gold pads were typically used.

3.1.3. Avidin SAM on Target Substrate Gold Pads

The procedure for forming an avidin SAM on the gold pads of the target pad substrate was based on a similar procedure used by Ding *et al*. on gold electrodes. [116] The functionalization procedure is schematically illustrated in Figure 3.2. To start, the protective photoresist layer on the gold pad target substrate was cleaned off with two cycles of rinsing with acetone and then IPA. Then the substrate was dried with nitrogen and placed in a 1.5 mL microcentrifuge tube filled with a 1 mM solution of 11-mercaptoundecanoic acid (MUA) in absolute ethanol. The thiol group on one end of the MUA acted as a head group and spontaneously attached to the gold pads to form an MUA SAM with carboxyl functional groups. The substrate was left in the MUA for 50 minutes to allow the SAM to form.

After 50 minutes, the substrate was taken out, rinsed with water, and placed in a 1.5 mL activator solution without drying. The activator solution was comprised of 50 mM 2-(*N*-morpholino)ethanesulfonic acid (MES) buffer (added first), 100 mM 1-ethyl-3-(3-dimethylaminopropyl)carbodiimide (EDC), and 50 mM *N*-hydroxysulfosuccinimide (Sulfo-NHS), all dissolved in cooled high performance liquid chromatography (HPLC) grade water. This solution was always prepared immediately prior to use

because some of the reagents (EDC in particular) are very unstable in aqueous environments. [117] The purpose of the activator solution in the SAM formation was to activate the carboxyl functional groups of the MUA so that they could be conjugated to primary amine groups on the avidin proteins that were added later. As can be seen in Figure 3.2, the EDC forms an active *O*-acylisourea intermediate on the end of the MUA. [118] With the help of Sulfo-NHS, this *O*-acylisourea ester will readily react with a primary amine group on an avidin protein to form an amide bond, leaving behind an isourea by-product. The Sulfo-NHS enhances the coupling efficiency while the MES buffer maintains a constant pH.

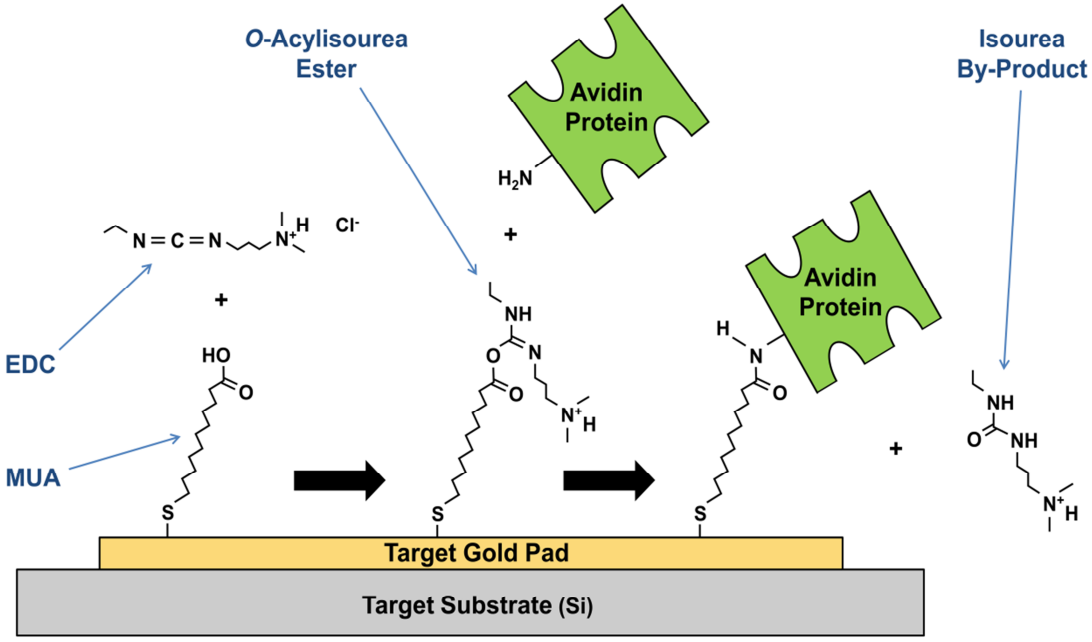

Figure 3.2: Schematic illustration of the procedure used to form an avidin SAM on the target gold pads. This 3-step illustration first shows the thiol adsorption of MUA onto the target gold pad to form an MUA SAM. The second step involves the addition of EDC to form an *O*-acylisourea intermediate on the end of the MUA. In the third step, the primary amine group on an avidin protein replaces the *O*-acylisourea intermediate so that the avidin becomes the functional group of the SAM while an isourea by-product is released.

After 40 minutes in the activator solution, the substrate was then rinsed with water and transferred into 1 mL of 1 mg/mL avidin stock solution that had been freshly thawed from the freezer. The avidin stock solution was made from lyophilized powder avidin (from egg white) dissolved in 1x (pH 7.4) phosphate buffered saline (PBS) solution with 0.05% polysorbate 20 surfactant. In this avidin solution,

the proteins formed amide bonds with the activated carboxyl groups on the end of the MUA SAM, so that avidin became the new functional group of the SAM. The substrate was left in this avidin solution for 60 minutes before being rinsed with water and placed in 1.5 mL of 1M glycine solution for 10 minutes. This glycine step was predicted by Ding *et al.* to help reduce non-specific binding and improve the selectivity of binding. [116] A likely explanation for why this would be is that the glycine forms a positive ionic layer on the Si/SiO_2 surface, which helps neutralize the surface charge so that fewer components non-selectivity stick to the substrate. Rinsing the substrate with a solvent like IPA after the assembly should then dissolve the glycine layer and remove some non-specifically bound nanoparticles with it. After the glycine step, the substrate was water rinsed again and dried. At this point, the substrate was placed in an empty 25 mL beaker and was ready for a drop of biotin-functionalized gold nanoparticles to be added for self-assembly.

3.1.4. Self-Assembly Procedure

The biotin-functionalized gold nanoparticle solution was gently vortexed prior to use. Then, a 5 μL volume of the nanoparticle solution was pipetted and dropped onto the center of the avidin-functionalized target gold pad substrate. The top of the beaker was then covered with parafilm and left to sit for 10 minutes, giving the nanoparticles time to self-assemble onto the pads. After 10 minutes, the parafilm was removed and a spray bottle was used to fill the beaker with HPLC water, sprayed at the center of the nanoparticle droplet first. Then, the substrate was picked up with a pair of Nalgene™ polypropylene forceps and rinsed thoroughly with HPLC water and then isopropyl alcohol (IPA), both from spray bottles. In some variations of the procedure, the substrate was then sonicated at a low intensity setting in a beaker of IPA. Using forceps, the substrate was clamped and held in the beaker with the gold pads facing down. After the IPA rinsing and/or sonicating, the substrate was dried with nitrogen and imaged with a scanning electron microscope (SEM). Variations in the rinse/sonication method produced direct variations in the final selectivity and yield of the self-assembled gold nanoparticles.

3.1.5. Yield and Selectivity Measurement

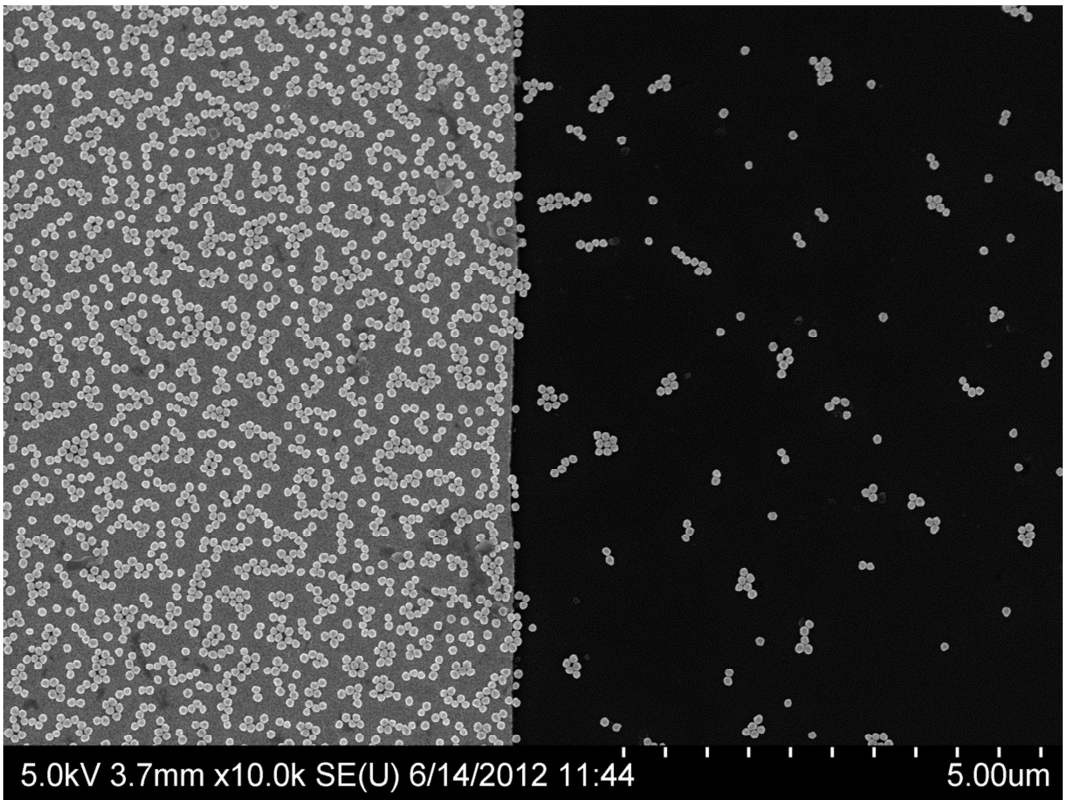

Figure 3.3: Sample SEM image of 100 nm biotin-functionalized gold nanoparticles selectively self-assembling onto the target gold pad (left) with much lower yield assembly onto the background silicon substrate (right).

A Hitachi S-4800 SEM microscope was used to image and characterize each substrate. To start, an unmagnified image of each substrate was taken to outline the area of the droplet (5 μL) of gold nanoparticle solution that was dropped onto the substrate. This image was later used to calculate the exact area of the droplet with the image processing program ImageJ by drawing an ellipse over the drop area and calculating the area based on a pixels/mm scale derived from the SEM scale bar. Then, individual target pads were imaged at a magnification of 10,000X and a 5.0 kV extra high tension (EHT) accelerating voltage. For each substrate, at least 6 SEM images were taken on target pads chosen at random locations across the substrate. These images were later analyzed in ImageJ to count the number of nanoparticles on and off the target pad in each image to produce yield and selectivity data. The image analysis results from each substrate were then averaged to produce the data in Table 1 of the results

section, with the error values resulting from the standard deviations in the data. As can be seen from Figure 3.3, an example SEM image used in the analysis, each image was taken on the right edge of a target gold pad, so that the left half of the image showed the gold pad and the right half of each image showed the background silicon substrate.

The steps to the ImageJ analysis of each target pad image were as follows: First a line was placed on the scale bar of the SEM image to set the scale in ImageJ to pixels/μm. Next, the threshold of the image was adjusted and applied so that only the nanoparticles appeared black and the background gold/silicon appeared white. Then the *noise despeckle* function was used to remove noise from the image, followed by the *binary watershed* function to ensure proper 1-pixel wide gaps between adjacent nanoparticles. The image was then cropped into two sections (one for nanoparticles on the gold target pad and one for nanoparticles off the target pad and on the background silicon) and the area of each section was measured. Then the *analyze particles* function was used to count the particles in the cropped area using a size setting of 0.005-0.02 μm^2 and a circularity setting of 0.1-1.

From ImageJ's count values, the assembled particle density on and off the pads could then be calculated by dividing the counted nanoparticles by the measured area of the section where the particles were counted. By generating a mask of the counted particles from the analyze particles function and then using the *measure* function, the percent area covered by assembled particles could also be determined. Figure 3.4 illustrates some of the steps in the ImageJ analysis performed on the SEM image from Figure 3.3. Figure 3.4A is at the step after the ImageJ threshold function has been used to make the nanoparticles appear black and the background appear white. This makes it possible for ImageJ to count the number of nanoparticles (based on size and circularity) using the analyze particles function. Figure 3.4B is from after the analyze particles function had counted all of the particles. The red area inside of each particle is actually written text numbering that the program adds to identify the count of each individual particle.

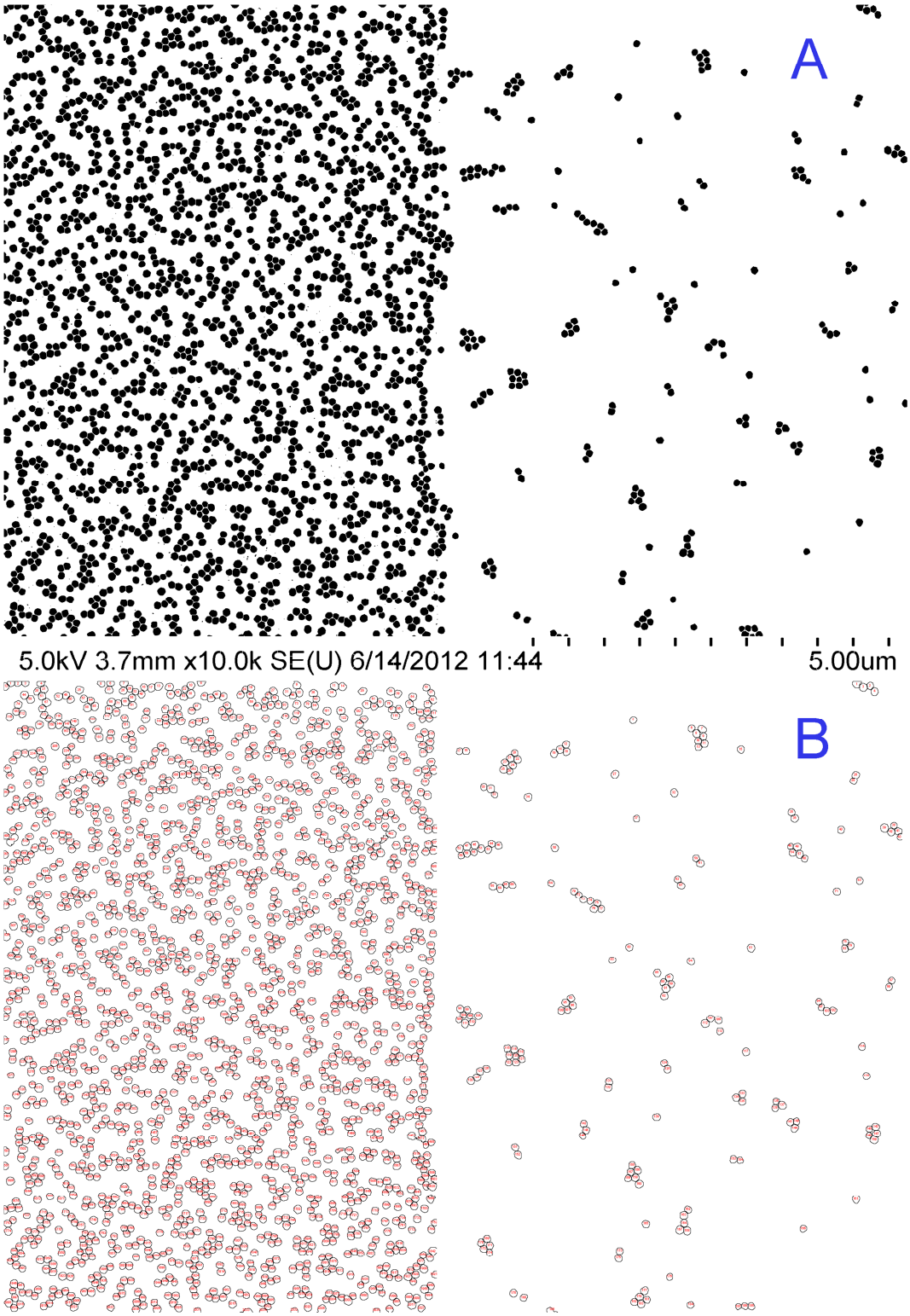

Figure 3.4: Illustration of some of the steps to the ImageJ nanoparticle counting analysis. (A) The threshold function is used to make the nanoparticles appear black and the background (gold or silicon) appear white. (B) After the analyze particles function is used to count the number of assembled nanoparticles, ImageJ can identify exactly which nanoparticle is counted for each number with red text inserted inside the outline of each nanoparticle.

The first four columns in Table 1 were calculated directly from the last two steps of the ImageJ analysis (once for the on pad section and again for the off pad section). The next four columns are simple comparison calculations to provide numerical figures for comparing the on pad and off pad values and determining the selectivity of the gold nanoparticles to preferentially assemble onto the functionalized target gold pads. The area selectivity figures were calculated from the analysis of the percent area covered, and the count selectivity figures were calculated from the particle count analysis. The on pad:off pad ratios are straightforward, calculated by dividing the average on pad values by the average off pad values. The percent of assembled particles on pad figure, however, looks at the total number of particles observed both on and off the target gold pad and gives a percentage of how many out of the total were observed on the target pad. Standard arithmetic error propagation formulas were used to calculate the corresponding error values for these figures from the standard deviation values of the original data. The final column, the assembly yield of nanoparticles in the droplet, was calculated from the following equation, (3.1):

$$Assembly\ Yield_{Nanoparticles\ in\ Droplet} = 100\% \times \frac{N_{Nanoparticles\ Assembled\ onto\ Target\ Pads}}{N_{Total\ Nanoparticles\ in\ Droplet}}$$

$$= 100\% \times \frac{Assembled\ Particle\ Density_{Average} \times Area_{Target\ Gold\ Pads}}{Volume_{Droplet} \times Density\ of\ Nanoparticles_{Droplet}}$$

$$= 100\% \times \frac{Assembled\ Particle\ Density_{Average} \times \frac{1}{9} \times Area_{Droplet}}{Volume_{Droplet} \times Density\ of\ Nanoparticles_{Droplet}}, \quad (3.1)$$

where the average assembled particle density is the value from Table 1, the area of the droplet was measured from an unmagnified SEM image, the target gold pad area is 1/9 of the droplet area because that is the fraction of the substrate area that was taken up by the target pad pattern, the volume of the droplet was 5 μL, and the concentration of nanoparticles in the droplet was 1.92×10^{11} particles/mL, as specified by the manufacturer.

3.2. Results & Discussion

Table 1: Summary of Main Results from Gold Nanoparticle Self-Assembly Experiments

Rinsing Method	Percent Area Covered by Assembled Particles (%)		Assembled Particle Density (Particles/µm^2)		Assembled Particle Area Selectivity		Assembled Particle Count Selectivity		Assembly Yield of Nanoparticles in Droplet
	On Pad	Off Pad	On Pad	Off Pad	(% of Assembled Particles On Pad)	(On Pad:Off Pad Ratio)	(% of Assembled Particles On Pad)	(On Pad:Off Pad Ratio)	(% of Particles in Droplet Assembled onto Target Pads)
IPA Rinse	**30.3** ± 1.0	**2.7** ± 0.6	**37.2** ± 0.9	**3.3** ± 0.8	**91.7** ± 4.4	**11.1:1** ± 2.3	**91.9** ± 3.5	**11.3:1** ± 2.6	**7.9** ± 0.2
Sonication in IPA and then IPARinse	**21.0** ± 4.1	**0.2** ± 0.2	**24.8** ± 4.7	**0.3** ± 0.2	**98.8** ± 27.1	**85.4:1** ± 56.2	**98.8** ± 26.5	**83.5:1** ± 58.4	**4.8** ± 0.9
7:3 IPA:Water Rinse	**31.7** ± 1.4	**4.5** ± 1.2	**35.1** ± 0.5	**5.7** ± 1.4	**87.5** ± 6.0	**7.0:1** ± 1.9	**86.0** ± 3.5	**6.1:1** ± 1.5	**6.7** ± 0.1
Acetone Rinse	**26.3** ± 6.7	**3.3** ± 1.7	**31.8** ± 5.0	**4.3** ± 2.1	**88.8** ± 30.8	**7.9:1** ± 4.6	**88.1** ± 19.3	**7.4:1** ± 3.7	**6.0** ± 1.0

Although many experimental variations were tested, Table 1 outlines some key results from the experiments performed using the procedure outlined above and variations in the rinsing method that followed the self-assembly. This experimental procedure and subsequent rinsing/sonication methods produced the best yield and selectivity results to date. As can be seen from the first two rows of results from the table, the best assembly yield result was achieved with the IPA rinse method and the best assembled particle count selectivity result was achieved with the low intensity IPA sonication method. In the IPA rinse method, where the substrate was simply rinsed with an IPA spray bottle after the procedure

from section 3.1.4, the average density of assembled particles on the gold target pads was 37.2 particles/μm^2, meaning an extrapolated yield of 7.9% of the particles in the droplet were assembled onto the target pads. In this highest yield result, ImageJ calculated the percent area of the target pad covered by nanoparticles to be 30.3%. To compare this number to the maximum possible result, the highest theoretical percent area coverage for a densely packed monolayer of equal diameter nanoparticles on a surface is 90.7%. This was shown by Conway *et al*., who demonstrated that the densest possible two-dimensional packing of equal diameter circles is the honeycomb hexagonal lattice, and the packing density is equal to $\frac{\pi}{2\sqrt{3}}$, or 90.7%. [119]

Although very high density and yield values were achieved, the IPA rinse method produced an assembled particle count selectivity ratio of only 11.3:1 of the nanoparticles assembling onto the avidin-functionalized gold pad areas as opposed to the surrounding silicon substrate. In the IPA sonication method, where the substrate was bath ultrasonicated upside down at a low power setting in a beaker filled with IPA before further IPA rinsing with a spray bottle, an improved average assembled particle count selectivity ratio of 83.5:1 was observed. However, although the count selectivity was greatly improved in this method, the average assembled particle density was reduced to 24.8 particles/μm^2 ($\sim \frac{2}{3}$ of the observed density in the IPA rinsing method), corresponding to a yield of only 4.8% of the particles in the droplet assembling onto the target pads.

A direct comparison of these two best-performing self-assembly attempts can be seen in the SEM images in Figure 3.5. There are 3,000X and 10,000X magnified SEM images of sample gold target pads from each of these two runs, with the IPA rinse method on top and the IPA sonication method on the bottom. As can be visually seen from the bottom right image, the IPA rinse method, although slightly reducing assembled nanoparticle density when compared to the IPA sonication method, produces a much better selectivity of nanoparticles on the target gold pad instead of the background silicon substrate. However, as can be seen in the bottom left image of Figure 3.5, the IPA sonication method does result in a few small sections of nanoparticles ripped off of the target gold pad. From this observation, and the

increase in the standard deviation values from the IPA rinse method to the IPA sonication method, we can conclude that the bath sonication method leads to less uniform overall coverage of the target pads.

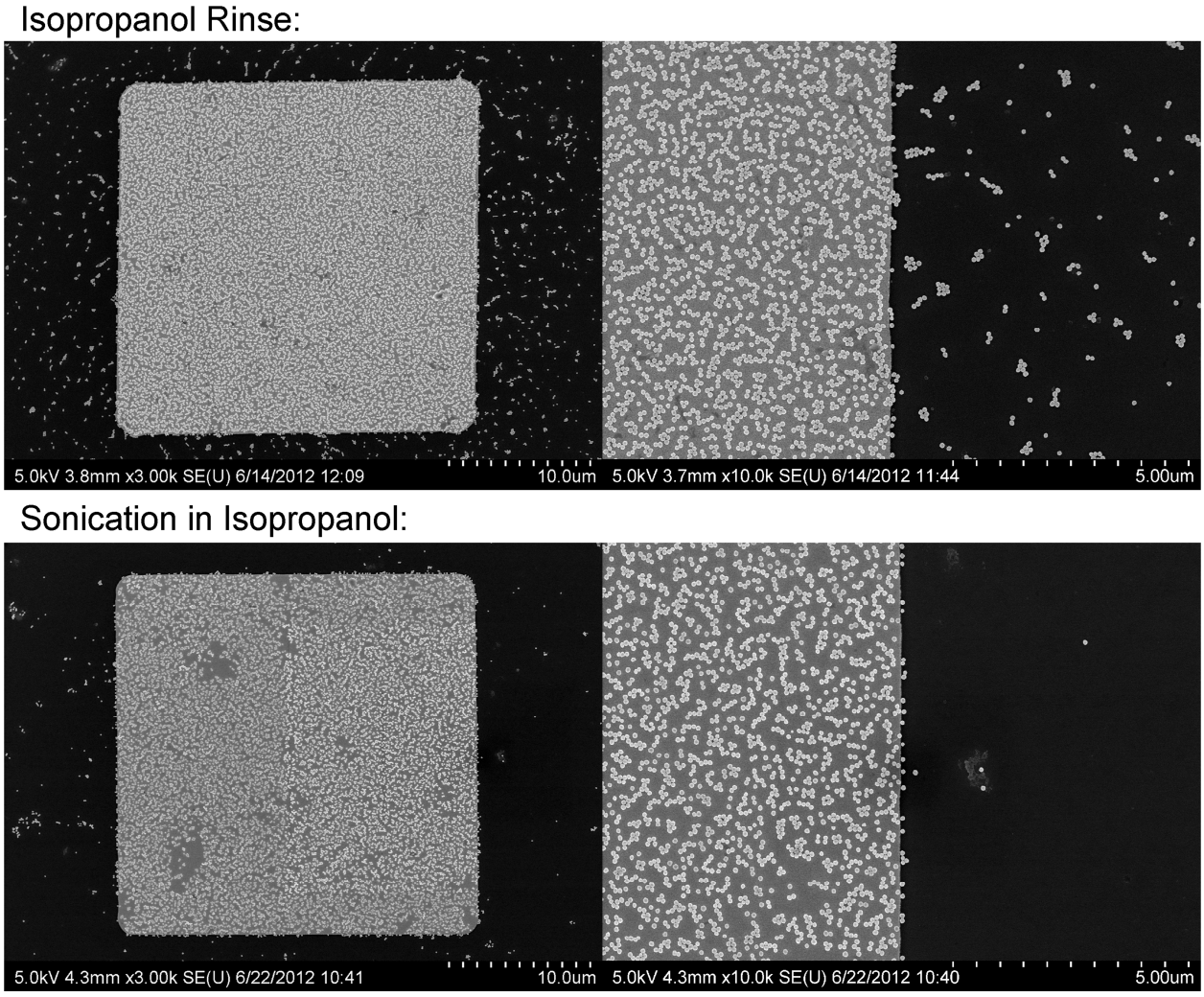

Figure 3.5: A comparison of two of the most successful self-assemblies of 100 nm wide biotin-functionalized gold nanoparticles onto avidin-functionalized target gold pads. The exact same avidin SAM formula was used for both results and the only experimental variation was the rinsing/sonication procedure afterward. In the upper two images, the substrate was rinsed with isopropyl alcohol (IPA) and no sonication was performed. In the lower two images, the substrate was submerged in an IPA bath and then sonicated at a low intensity setting for 5 minutes, followed by further IPA rinsing. The two images on the left are 3,000X magnified images showing the entire 25 μm x 25 μm target gold pad while the two images on the right are 10,000X magnified for the particle counting analysis.

3.2.1. Variations to the Experiment

There were many small variations to the experimental procedure outlined in section 3.1 that were experimentally tested to see if yield or selectivity could be improved. However, the best observed results

were obtained when the experiment was performed exactly as described in section 3.1. For example, some experimental variations that reduced the yield of assembled nanoparticles included piranha cleaning the gold pad substrate prior to the avidin SAM formation (which induced noticeable roughing in the gold layer) or using *N*-hydroxysuccinimide (NHS) instead of *N*-hydroxysulfosuccinimide (Sulfo-NHS) during avidin SAM formation. The most noticeable experimental variation that reduced the nanoparticle assembly yield, however, was the use of old or expired reagents, namely avidin, EDC, Sulfo-NHS, and the biotin-functionalized gold nanoparticle themselves. Although very careful storage precautions were taken, these reagents in particular still have very short shelf lives, and high assembly yields could not be achieved with reagents aged past 6 months. For example, the EDC and Sulfo-NHS powders are very moisture sensitive, so they were stored in heat sealed moisture barrier bags with desiccant pouches. The EDC (in moisture barrier bag) and avidin-PBSP solutions were stored frozen at -20°C, while the Sulfo-NHS (in moisture barrier bag) and biotin-functionalized gold nanoparticles were stored refrigerated at 4°C. For all four of these reagents, controlled experiments were performed in which the same procedure was used and all new reagents were used, but one of the reagents was replaced with an old (expired) version of it. For all four of these reagents, the SEM analysis afterwards demonstrated lower assembly yield when the respective older reagent was used.

Some other experimental variations resulted in poor assembled particle selectivity between the gold pads and the silicon substrate. These experimental variations included: a Hexamethyldisilazane (HMDS) coat on the substrate prior to avidin SAM formation, dissolving the avidin in PBS without polysorbate 20 added to make the avidin functionalization solution, excluding the glycine step at the end of the SAM formation procedure, rinsing with only water after assembly, and sonicating in water after the assembly sequence. An interesting experimental variation that could potentially improve the assembled particle count selectivity was inspired by the fact that, once formed, the avidin-biotin bond can withstand great extremes in pH. [87] Experiments with substrates that had already gone through the self-assembly procedure (and already had biotin-functionalized gold nanoparticles assembled onto the avidin-functionalized gold pads) demonstrated that dipping the substrate (inverted) in a beaker of highly acidic

buffered oxide etch (BOE: a mixture of ammonium fluoride and hydrofluoric acid) solution did not reduce the density of assembled nanoparticles on the target pads, even after rinsing with water following the BOE dip. A controlled experiment with SEM images taken on the same traditional gold pad substrate before and after the BOE dip demonstrated that the yield and selectivity results were virtually unaffected.

In another experimental variation, before the target gold pads were deposited on the silicon substrate, a 100 nm thick layer of sacrificial SiO_2 was deposited on the substrate by low pressure chemical vapour deposition (LPCVD). Then, using the same procedure as described in section 3.1.2, the target gold pads were deposited and patterned on top of the SiO_2. They were subsequently functionalized with an avidin SAM and had biotin-functionalized gold nanoparticles self-assembled onto them using the standard procedure. Initially, the selectivity of the assembled nanoparticles was very poor in this experiment, but after a 4 minute dip of the inverted substrate (pads facing down) in a BOE solution, the 100 nm SiO_2 layer was removed and a large majority of the off-pad nanoparticles were removed with it. Using this method, the average off-pad particle density was extremely low and an assembled particle count selectivity ratio of 240:1 was achieved. This substrate is pictured in Figure 3.6. Unfortunately, this experiment was attempted using aged reagents that were about 1 year old, so the assembly yield was not as high as the results obtained with fresh reagents, pictured in Figure 3.5.

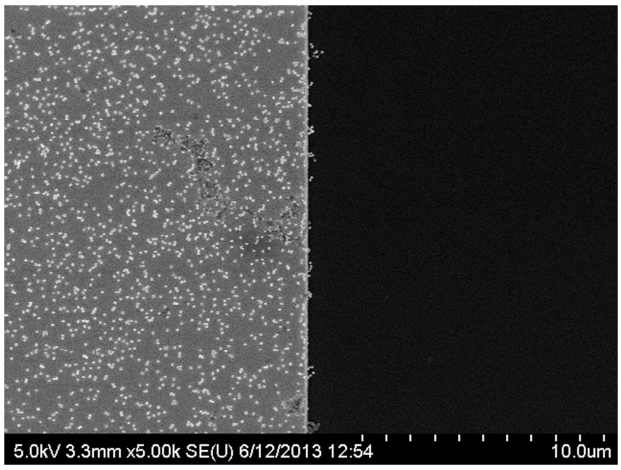

Figure 3.6: SEM image of a sample that had a sacrificial SiO_2 layer deposited by PECVD on top of the silicon substrate before the gold pads were deposited and patterned. This substrate had biotin-functionalized gold nanoparticles self-assembled onto its avidin-functionalized gold pads by the procedure outlined in section 3.1. After the after the assembly, however, the SiO_2 layer was wet etched away by a dip in BOE, which removed a large majority of the non-specifically bonded nanoparticles on the background substrate.

In another experimental variation, a control experiment was performed with the exact same sequence as described in section 3.1, but in this iteration the PBSP solution that was used for the avidin

functionalization step contained no avidin. This experiment resulted in an average assembled particle density of less than 0.05 particles/μm^2, indicating that the self-assembly of the biotin-functionalized nanoparticles onto the gold pads was driven by the avidin-biotin interaction. And since there was also a far lower density of gold nanoparticles sticking to the silicon substrate as well during this experiment, it is hypothesized that the avidin protein may be sticking to the silicon substrate in trace amounts during the avidin SAM formation procedure and causing nanoparticles to stick to the silicon. This may be a large factor in the observation of some assembled nanoparticles on the background silicon substrate, as can be seen in Figure 3.5.

Experiments were also attempted with smaller biotin-functionalized gold nanoparticles that were purchased from the same company (Cytodiagnostics). Although the 100 nm wide nanoparticles performed the best, trials were also attempted with 60 nm, 30 nm, and 10 nm. From the observed SEM results, the assembly yield and target pad coverage results appeared to decrease as the nanoparticle diameters decreased. For 100 nm, 60 nm, 30 nm, and 10 nm diameter assembled nanoparticles, the average pad area coverage results were 30.3%, 28.9%, 7.3%, and 0.20% respectively. The 10 nm wide biotin-functionalized nanoparticles performed exceptionally poorly in terms of assembly density and pad coverage. This is likely because of the extreme curvature of the surface of such small nanoparticles. There would be very little surface area of the nanoparticle making contact with the target substrate, so the formation of only a few avidin-biotin bonds would be possible. This reduction of contact area from scaling down greatly reduces the attainable binding forces between the nanoparticles and the target pads.

3.3. Conclusion

The main purpose of the experiments in this chapter was to test out the capability of the avidin-biotin interaction to drive the die-to-substrate fluidic self-assembly of nanoscale components. The experiments were also used to develop an adequate procedure for forming a biotin-binding SAM on gold with avidin as the functional group. The experiments demonstrated successful results with 100 nm diameter biotin-functionalized gold nanoparticles self-assembling onto avidin-functionalized gold pads with a dense assembly yield and a strong selectivity of binding to the target pads as opposed to the

surrounding silicon substrate. Through repeated experimental variations, the details of the procedure were optimized, with the best results obtained using the experimental method outlined in section 3.1. The best assembly yield and selectivity results were obtained using two different rinsing procedures that were performed after the assembly. A method where the target pad substrate was simply rinsed with IPA after assembly demonstrated the highest yield of assembled nanoparticles (7.9%) and a moderate count selectivity ratio of 11.3:1. However, another method, where the target pad substrate was sonicated in IPA at a low intensity setting after the assembly, demonstrated an improved selectivity result of 83.5:1, but at the cost of reducing the assembly yield down to 4.8%, corresponding to a reduction in the observed nanoparticle density of $\sim \frac{2}{3}$ compared to the results produced by the IPA rinsing method. The experimental procedure that was used to form the avidin SAM on the target gold pads was later used in the silicon microtile self-assembly experiments of Chapter 5.

4. Self-Assembly of Avidin-Coated Polystyrene Microspheres

This chapter outlines and discusses a set of experiments performed in which avidin-coated polystyrene microspheres were self-assembled onto functionalized target gold pads. The purpose of these experiments was to develop a procedure for forming a reliable, avidin-binding self-assembled monolayer (SAM) on gold with biotin as the functional group.

4.1. Experimental

4.1.1. Experimental Overview

In a similar fashion to the experiments in Chapter 3, where biotin-functionalized gold nanoparticles were used to develop an avidin SAM procedure by testing its ability to self-assemble the gold nanoparticles, this chapter instead uses avidin-functionalized particles to develop a procedure for forming a biotin SAM on gold and test its ability to self-assemble the avidin-functionalized particles. The experimental procedure for forming the biotin SAM was developed through much experimental iteration until the best foreseeable self-assembly results were obtained. Once developed, the avidin SAM procedure from Chapter 3 and the biotin SAM procedure derived in this chapter were both employed in the microtile self-assembly experiments of Chapter 5.

Three sizes of pre-functionalized avidin-coated polystyrene microspheres were purchased from Spherotech Inc. (Chicago) in batches with diameter ranges of 0.7 μm-0.9 μm, 1.0 μm-1.9 μm, and 3.0 μm-3.9 μm. The respective mean diameters of these batches were 0.82 μm, 1.34 μm, and 3.08 μm. These mean values will be used to refer to each batch in this Chapter. The avidin-coated microsphere solutions were self-assembled onto functionalized gold pads in a very similar manner to that described in Chapter 3.1.4. A small volume of the solution was dropped onto the target pad substrate, left to self-assemble, and then rinsed off after 10 minutes. Because such conducive self-assembly results were obtained with the commercially purchased biotin-functionalized gold nanoparticles in Chapter 3, the biotin SAM functionalization procedure developed in this chapter was based on the SAM on the biotin-functionalized

nanoparticles. That SAM was specified by the manufacturers to be a mixed monolayer made up of longer (molecular weight of 10 kDa) biotin-PEG-SH chains in a ~1:100 ratio with a shorter (5 kDa) methoxy-PEG-SH backbone chains, where PEG is short for polyethylene glycol and -SH denotes a thiol group. The biotin SAM developed in this chapter was also made up of 10 kDa biotin-PEG-SH chains and 5 kDa methoxy-PEG-SH backbone chains. Both of these reagents were purchased in powder form from Nanocs. Simple molecular weight calculations can show that the 10 kDa biotin-PEG-SH chains contain ~220 PEG units while the 5 kDa methoxy-PEG-SH chains contain ~111 PEG units, indicating they are much shorter.

4.1.1. Target Substrate Fabrication

The target pad substrates used in this chapter were fabricated using the procedure from Chapter 3.1.2. The 9 mm x 6.5 mm silicon substrates were patterned with 35 nm thick square gold pads that were deposited by evaporation and patterned via lift-off. For this set of experiments, 25 μm wide rectangular gold pads with various lengths were used.

4.1.2. Biotin SAM on Target Substrate Gold Pads

The procedure used for forming the biotin SAM on gold in this section generates a similar mixed monolayer to the one that was on the commercially purchased biotin-functionalized gold nanoparticles from Chapter 3. It was specifically based on a similar mixed monolayer forming technique used by Perrault *et al*. for gold nanoparticles. [120] The procedure forms a mixed monolayer comprised of two PEG chains: a longer biotin-PEG-SH chain (10 kDa) and a shorter methoxy-PEG-SH chain (5 kDa), both of which were purchased from Nanocs. The mixed monolayer was intended to space apart the biotin molecules at the surface to improve binding yields with avidin proteins. The longer biotin-terminated chain presents the biotin molecules at the surface of the monolayer for binding while the shorter methoxy-terminated chain acts as a backbone. This backbone acts to support the biotin chains and fill the gaps between and underneath the biotin molecules, spacing them out along the surface of the gold. This packing conformation can be thought of as a "trees and grass" model, where longer chains (trees) support larger molecules (biotin, in this case) extending overtop of shorter smaller-molecule chains (grass), which fill in the gaps between the trees. [115] Both chains have a thiol group at one end that spontaneously binds

to gold surfaces when in ethanol solutions. Because the binding kinetics for the two different PEG chains are considerably different, two individual surface functionalization steps were performed: one for each PEG chain.

A few one-step functionalization methods were attempted in the initial stages of this experiment, but this led to very poor results. For example, when the methoxy-PEG-SH and biotin-PEG-SH were dissolved in absolute ethanol in a 100:1 molar ratio, and then the target substrate was functionalized in this solution, the following self-assembly of the avidin-coated microspheres led to reverse selectivity results, meaning the avidin microspheres would preferentially bind to the unfunctionalized silicon substrate over the functionalized gold pads. Similar results were observed if no methoxy-PEG-SH reagent was used at all. Furthermore, an experiment in which no functionalization was performed at all demonstrated better self-assembly yields than the two previously described biotin SAMs did. In Perrault *et al.*'s biotin-PEG-SH/methoxy-PEG-SH mixed monolayer procedure, a three-step functionalization method was used to form the monolayer. [120] Their SAM also used 10 kDa biotin-PEG-SH chains and 5 kDa methoxy-PEG-SH chains. They first introduced the methoxy-PEG-SH at a very low concentration so that it could only form a SAM at a maximum density of 0.3 molecules/nm^2. Then they introduced the biotin-PEG-SH at a concentration that was possible to form a 0.6 molecules/nm^2 density SAM, and finally another more concentrated methoxy-PEG-SH step was used to saturate the nanoparticle surface with 10 molecules/nm^2 possible from the concentration. [120]

A schematic illustration of the mixed monolayer biotin SAM used in this thesis and its two-step sequential formation can be seen in Figure 4.1. The gold surface was first exposed to the biotin-PEG-SH chains at low concentration so that the SAM would form with the biotin molecules spaced apart at the surface of the monolayer and not crowding each other. Then the substrate was exposed to the methoxy-PEG-SH chains at a higher concentration to fill in the gaps and saturate the surface, acting as a backbone for the biotin chains. This spacing out of the biotin molecules on the target pad surface was inspired by Huang *et al.*, who showed that biotin mixed monolayer SAMs with diluted biotin top units less spatially crowded by neighbouring biotins demonstrated better binding capacities with avidin proteins. [121] This

phenomenon was explained by Canaria *et al*., who, with similar biotin mixed monolayers made from much shorter PEG chains, showed that when the biotin:backbone ratios became greater than 1:2, the SAMs become disordered, with biotin units buried in the monolayer. [122]

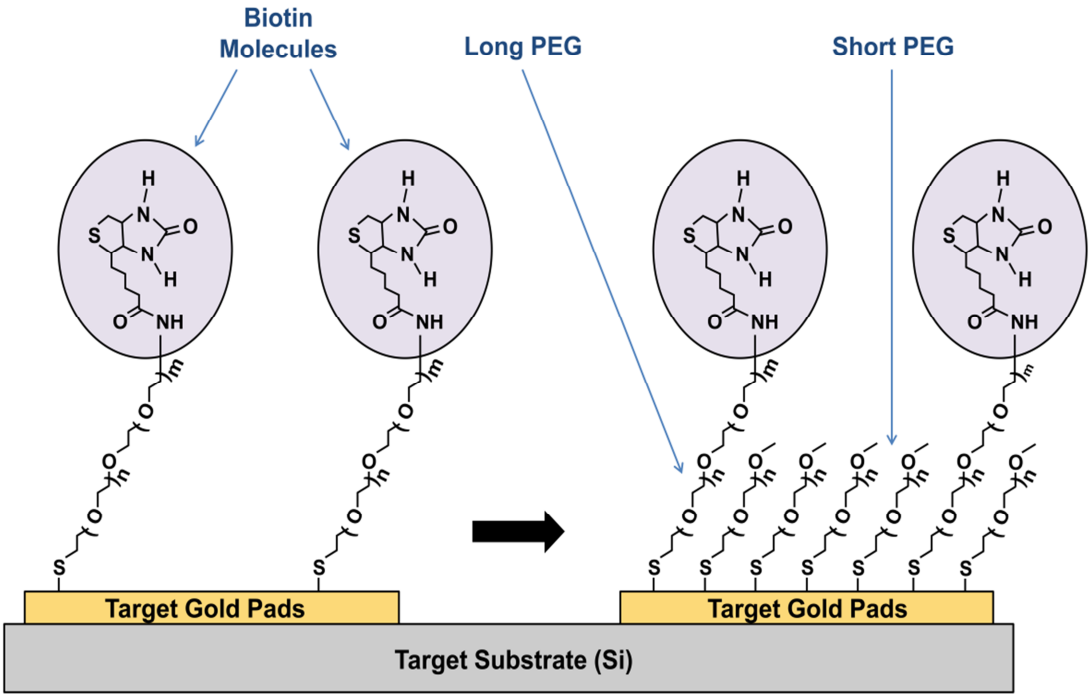

Figure 4.1: Schematic illustration of the procedure used to form the biotin SAM on the gold pads of the target substrate. The sequential addition of longer biotin-PEG-SH chains (molecular weight of 10 kDa) and then shorter methoxy-PEG-SH chains (5 kDa) forms a mixed monolayer SAM with spaced apart biotin molecules available at the surface of the monolayer. From the molecular weights of these PEG chains, it can be estimated that n in the figure is approximately equal to 111, while m is approximately equal to 108.

Although many experimental iterations were used to develop the final experimental procedure for forming the biotin mixed monolayer, the main variable of investigation was the concentration of the biotin-PEG-SH reagent that was used, as this variable proved to have a major impact on the self-assembly results. For all three of the avidin-coated microsphere sizes that were purchased, the same self-assembly experiment was performed five times using five chosen concentrations of this biotin-PEG-SH reagent to determine which reagent concentration was best for forming a reliable, avidin-binding SAM. Thus, in total, 15 of these substrates underwent the self-assembly experiment of this chapter and the subsequent imaging analysis procedure.

To start the experimental procedure, 3.33 mg/mL stock solutions of the biotin-PEG-SH and methoxy-PEG-SH reagents were made by dissolving 5 mg of the respective reagent powders in 1.25 mL of absolute ethanol and 0.25 mL of high-performance liquid chromatography (HPLC) water. Although vortexing was used to mix these solutions, the small amount of water was required to fully dissolve the powder reagents. The biotin-PEG-SH was then pipetted and diluted into five different 1.5 mL microcentrifuge tubes to form the five functionalization solutions, all of which contained different concentrations of biotin-PEG-SH. For each microsphere size tested, 1 μL, 3 μL, 5 μL, 7 μL, and 9 μL amounts of the 3.33 mg/mL biotin-PEG-SH stock solution were pipetted into the five microcentrifuge tubes and each was topped up to 1.5 mL with absolute ethanol. This resulted in five functionalization solutions with concentrations of 2.22 μg/mL, 6.67 μg/mL, 11.11 μg/mL, 15.56 μg/mL, and 20.0 μg/mL respectively.

Five of the target gold pad substrates were then cleaned off by two cycles each of acetone/IPA rinsing, and then dried and placed in their respective functionalization tubes. All five of these tubes were taped to a vortexing table and gently agitated at a speed of 200 RPM. These substrates were left vortexing with the gold pads facing up for 2 hours to allow time for the biotin-PEG-SH SAM to form on the gold pads. For each substrate, the methoxy-PEG-SH functionalization solution was prepared the same. A 10 μL volume of 3.33 mg/mL stock solution was pipetted into a 1.5 mL microcentrifuge tube and topped up with absolute ethanol, resulting in a 22.22 μg/mL functionalization solution. This was predicted to be a high enough concentration to fully saturate the gold pad surface with methoxy-PEG-SH molecules. After 2 hours of biotin-PEG-SH SAM formation, the five gold pad substrates were transferred into the five methoxy-PEG-SH microcentrifuge tubes without rinsing. These tubes were also taped to the vortexing table and left vortexing at 200 RPM for 40 minutes.

4.1.3. Self-Assembly Procedure

After 40 minutes was allowed for the bottom methoxy-PEG-SH layer of the mixed monolayer SAM to form, the substrates were sequentially pulled out of the functionalization tubes, rinsed with HPLC water from a spray bottle, dried with nitrogen, and then a 20 μL volume of the respective avidin-

coated microsphere solution was dropped onto each substrate. They were each contained in a small empty beaker covered with parafilm while they were left to sit for 10 minutes to allow the microspheres to self-assemble. After 10 minutes, the substrates were rinsed with a bottle of HPLC water aimed at the center of the microsphere drop, and then removed from the beaker for further rinsing. They were then dried and mounted onto SEM stubs to be for imaged and analyzed.

4.1.4. Assembled Microsphere Density Calculation

A LEO™ 1430 SEM microscope was used to image and characterize each microsphere-assembled substrate. All images were taken at magnifications ranging from 2000X-4000X, and a 10.0 kV EHT accelerating voltage was used in the SEM. For each sample, at least 5 SEM images were taken of various target pads chosen at random locations across the substrate. These images were then analyzed in the image processing program ImageJ to count the number of microspheres on each target pad in a similar manner to Chapter 3.1.5. From the ImageJ analysis, the average density of assembled microspheres could be determined for each of the five variations of the biotin-PEG-SH reagent concentration. The results of this analysis are included in Table 2, as well as plotted in Figure 4.5. The results in the table are average values calculated from the 5 images taken and analyzed at each reagent concentration/microsphere tested, with the error values resulting from the standard deviations of the data. For the 3.08 μm diameter microspheres, since the microspheres were so large and the assembled counts were so low, this analysis was actually performed with optical microscope images and manual counting. For the analysis of the other two microsphere sizes (0.82 μm diameter and 1.34 μm diameter), the ImageJ software extension Fiji was also used to generate x, y coordinates for the centroids of each of the microspheres that were counted during the ImageJ particle analysis. These coordinates were later used to analyze the clustering patterns of the assembled microspheres on the target pads, as detailed in section 4.1.5.

Similarly to the ImageJ analysis described in Chapter 3.1.5, the steps to the ImageJ analysis for the self-assembled avidin-coated microspheres were as follows: First, a line was placed on the scale bar of the SEM image to set the scale in ImageJ to pixels/μm. Next, the threshold of the image was adjusted and applied so that only the nanoparticles appeared black and the background gold/silicon appeared white.

The image was then cropped to the size of the target gold pad, and the exact dimensions of the cropped image were measured by the line tool to determine the dimensions of the area being analyzed. The *noise despeckle* and the *binary watershed* functions were then used to remove any noise and ensure proper 1-pixel wide gaps between any adjacent microspheres. The *analyze particles* function was then used with the ImageJ Fiji extension to count the assembled microspheres using a size setting of 0.75-4 μm^2 for the 1.34 µm diameter microspheres and 0.25-3 μm^2 for the 0.82 µm diameter microspheres. A circularity setting of 0.2-1 was also used for both analyses to remove any non-circular discrepancies in the images such as dust particles. The assembled microsphere density for each gold pad could then be calculated by dividing the counted microspheres by the area of the cropped image. With the ImageJ Fiji extension, the area and *x*, *y* coordinates of the centroids of each of the counted microspheres were also produced.

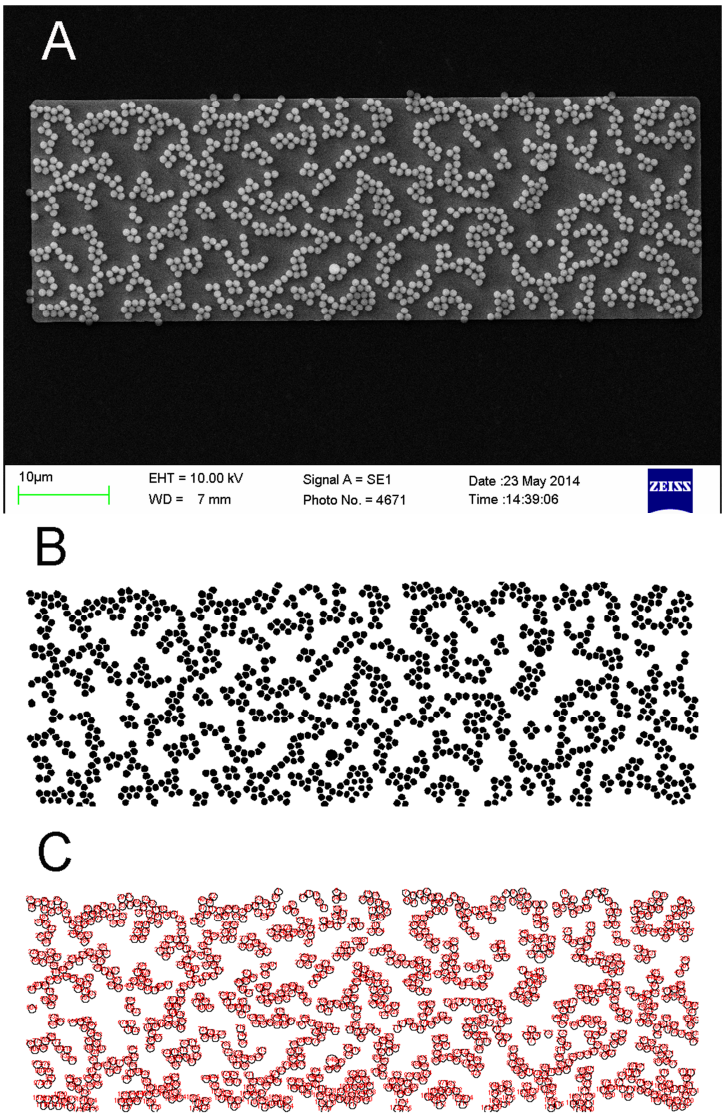

Figure 4.2: A visual depiction of some of the steps involved in the ImageJ microsphere counting analysis. (A) An original SEM image taken on a random target gold pad on a 11.11 µg/mL biotin-PEG-SH concentration sample from the 0.82 µm diameter microsphere batch. (B) The same image after using ImageJ's threshold, crop, noise despeckle, and watershed functions. (C) The image after the ImageJ analyze particles function has been used to count the number of assembled microspheres, with the count of each microsphere indicated by red text inserted inside the outline of each one.

Some of the steps to the ImageJ analysis are outlined visually in Figure 4.2, which demonstrates the analysis on one of the higher assembled microsphere density samples from the 0.82 μm diameter batch.

4.1.5. Clustering Analysis

As can be seen from Figure 4.2, and later in Figure 4.4, significant clustering of the assembled microspheres can be observed. In order to assess this clustering, the *x*, *y* centroid coordinates (in μm units) of all of the counted microspheres in selected images were analyzed. For the 0.82 μm diameter and 1.34 μm diameter batches, 3 out of the 5 SEM images taken for each of the 5 biotin-PEG-SH reagent concentrations tested were selected to have a histogram analysis performed, and a histogram plot was generated for each of these. These 3 were selected based on assembled particle densities closest to the average of the 5 images in the set. To perform the histogram clustering analysis, the following steps were taken: The area and centroid coordinate data for each of the counted microspheres was first pasted into an excel spreadsheet and then transpose-pasted along the orthogonal axis. Then an array of distance values was then computed for every possible pairing of counted microspheres in the image. Equation 4.1 was used to compute the centroid-to-centroid distance between each possible pairing of microspheres:

$$Distance_{Centroid-to-Centroid} = \sqrt{(x_2 - x_1)^2 + (y_2 - y_1)^2}. \quad (4.1)$$

Due to the 2-dimensional nature of the array, this distance value was computed twice for every possible pair. This was accounted for later by dividing the histogram count values by 2. For *N* counted microspheres in an image, the unique number of pairings between microspheres is equal to $\frac{(N)(N-1)}{2}$.

The average diameter of all of the microspheres in the image was calculated by averaging the area data of each counted microspheres, which was also provided by Fiji. A set of bin values was then computed based on multiples of the average diameter. For example: Bin *1d* would include all of the centroid-to-centroid distance values ranging from 0 μm to the average diameter of all the microspheres (*1*×*d*), Bin *2d* would include all of the centroid-to-centroid distance values ranging from *1d* to 2 times the average diameter of all the microspheres (*2*×*d*), and so on. A histogram plot and count was then constructed from these bin ranges and all of the computed centroid-to-centroid distance values. To

account for each value being computed twice, the histogram count values were all divided by 2. An example histogram plot (computed from a 1.34 µm diameter sample) can be seen in Figure 4.3. As can be seen from the plot, there is a significant number of pairs of microspheres with centroid coordinates that are between *1d* and *2d* away from each other. These can be considered 'near neighbour' microspheres, and are the most important indicators of clustering. Therefore, the values in the *2d* bins of each histogram are the focus of this analysis.

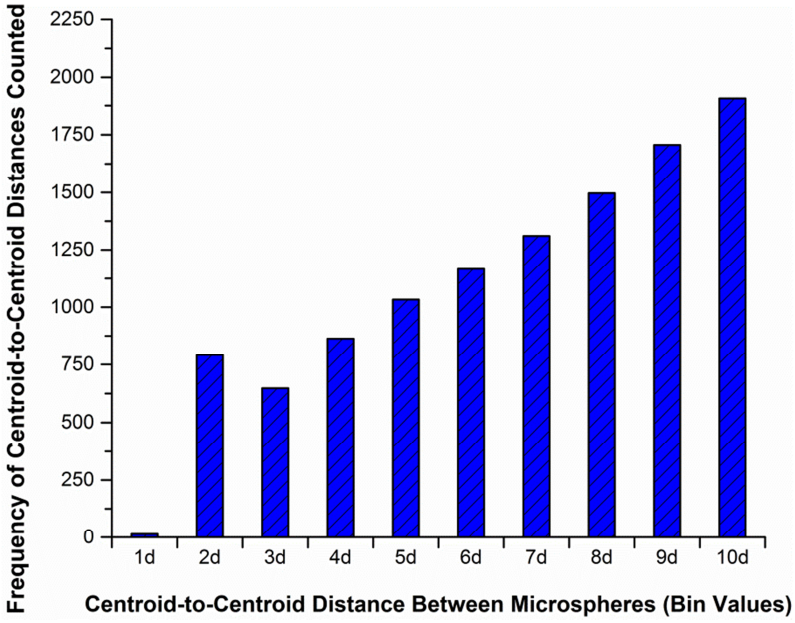

Figure 4.3: An example histogram plot where the centroid-to-centroid distances between all of the possible pairs of assembled microspheres on a target pad were computed and placed into distance bins that were selected to be multiples of the average microsphere diameter on the target pad. This sample histogram was generated from an image in the 1.34 µm diameter microsphere batch.

Since the target gold pad was only 25 µm wide in the y-direction (L_y), the boundary effects of the pad edges have a strong influence on the number of centroid-to-centroid distances that are greater than $\frac{1}{2}$ of this shortest target pad dimension, which is *10d* in the case of the histogram in Figure 4.3. Therefore, only bin ranges of less than $\frac{1}{2}$ of the shortest target pad dimension were analyzed. Also, in future histograms, the values for the frequency of centroid-to-centroid distances counted were divided by $(N-1)/2$ so that a per-particle average distribution of distances could be calculated. This variable is

labeled in the histogram of Figure 4.6 as the average number of neighbouring microspheres found within a distance bin range.

4.2. Results & Discussion

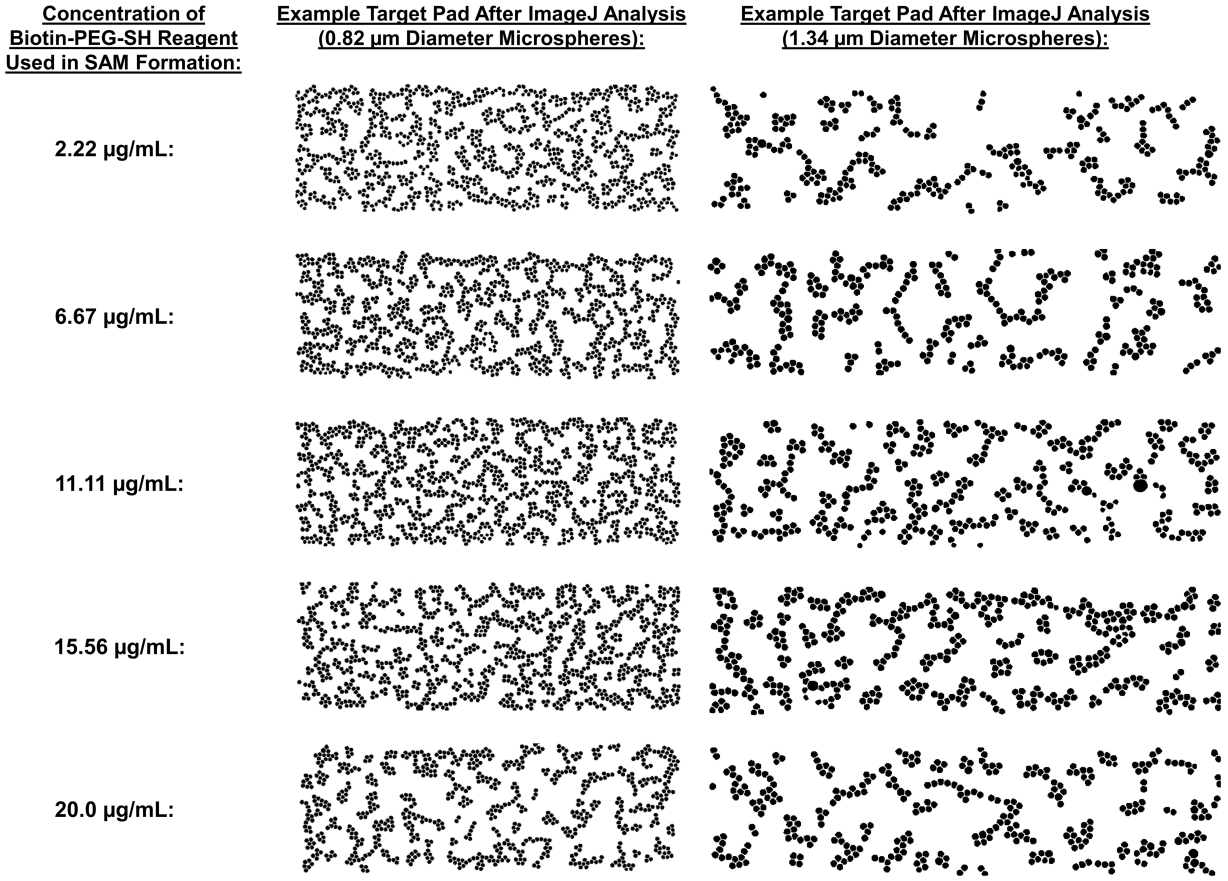

Figure 4.4: A visual summary of the ImageJ counting analysis performed on the 0.82 µm diameter and 1.34 µm diameter microsphere batches. Based on the closest match to the average self-assembled microsphere density, one ImageJ-modified image from each of the biotin-PEG-SH reagent concentrations tested was chosen for this figure. Viewing them next to each other, the effect of the SAM formation reagent concentration on the final self-assembly density can be seen visually.

A visual summary of the results of the ImageJ microsphere counting analysis for the 0.82 µm diameter and 1.34 µm diameter microsphere batches can be seen in Figure 4.4. The figure shows one ImageJ-modified target pad image from each of the five biotin-PEG-SH reagent concentrations that were tested for the two microsphere sizes. The specific target pads in the figure were chosen based on having the closest assembled microsphere densities to the average of the five images analyzed for each reagent

concentration/microsphere size. Therefore, those images show a visual summary of how the density of microspheres on the target pads changed as the biotin-PEG-SH reagent concentration was varied. Although the 1.34 µm microspheres did not self-assemble as densely as the 0.82 µm microspheres, both sets of images show that the best performing biotin-PEG-SH reagent concentrations were somewhere in the middle of the field of values tested. A numerical summary of the results of this ImageJ counting analysis can be found in Table 2, which also includes the assembly results from the experiments with 3.08 µm diameter microspheres. The ± error values in the table were calculated from the standard deviations of the averaged assembled microsphere density results.

Table 2: Summary of Results from Avidin-Coated Microsphere Self-Assembly Experiments

Concentration of Biotin-PEG-SH Used in SAM Formation (µg/mL)	**Average Assembled Microsphere Density (Microspheres/µm^2)**		
	0.82 µm Diameter Microspheres	**1.34 µm Diameter Microspheres**	**3.08 µm Diameter Microspheres**
2.22	**0.578** ± 0.010	**0.118** ± 0.005	**0.0007** ± 0.0006
6.67	**0.584** ± 0.046	**0.127** ± 0.009	**0.0029** ± 0.0007
11.11	**0.623** ± 0.029	**0.163** ± 0.010	**0.0074** ± 0.0014
15.56	**0.584** ± 0.019	**0.164** ± 0.015	**0.0238** ± 0.0049
20.0	**0.536** ± 0.065	**0.140** ± 0.023	**0.0100** ± 0.0015

For the best performing result from the 0.82 μm batch (achieved at a biotin-PEG-SH concentration of 11.11 μg/mL), further imaging was performed around the surrounding silicon substrate so that a yield and selectivity analysis could be performed using the same methods as Chapter 3.1.5. For this sample with the highest average microsphere density of 0.623 microspheres/μm^2 on the gold pads, a much lower average microsphere density of 1.17×10^{-4} microspheres/μm^2 was found on the surrounding silicon substrate. This meant for a very high count selectivity ratio of 5300:1 in favour of microspheres assembling onto the pads as opposed to off of them. The assembly yield of all of the microspheres in the 20 μL drop, however, was much lower than the best results of Chapter 3. Using Equation 3.1, the average assembly yield on the best performing 0.82 μm batch sample was calculated to be 0.098% ± 0.005%. Although it was a well performing result, this assembly yield was low because the concentration of microspheres in the manufacturer provided solution was so high. For microspheres with diameters greater than 8x those of the gold nanoparticles from Chapter 3, the manufacturer specified concentration of this 0.82 μm microsphere solution was 1.65×10^{11} microspheres/mL. This figure very similar in magnitude to the concentration specified for the gold nanoparticles in Chapter 3.

The results from Table 2 are plotted in Figure 4.5, which visually shows the pattern of how the self-assembled microsphere density varied with respect to the concentration of the biotin-PEG-SH reagent used for the SAM formation. It should be noted that this plot is not to scale. Since different microsphere sizes were used in the three batches that were tested (0.82, 1.34, and 3.08 μm average diameters), the assembled microsphere densities (microspheres/μm^2) were significantly different between the three batches. Therefore, in order to plot all three together and visually deduce the pattern between all three batches, different scales on the *y*-axis were used for each. In Figure 4.5, the 0.82 μm diameter (red) and 1.34 μm diameter (green) assembled microsphere densities are plotted using the scale on the left hand side of the graph (with a break in the axis). Since its assembled microsphere density values were so much lower, the 3.08 μm diameter batch (blue) was plotted using the scale (also pictured in blue) on the right side of the graph. By using these three different scales for each microsphere size, the trends in each data set can be compared next to each other. All three sets of data exhibit a peak in assembled microsphere

density. The 1.34 µm and 3.08 µm microspheres performed best when the 15.56 µg/mL reagent concentration was used, whereas the 0.82 µm microspheres performed best when the 11.11 µg/mL reagent concentration was used. Another trend that can be seen from the graph is that the optimal reagent concentration appears to decrease as the microsphere diameter decreases.

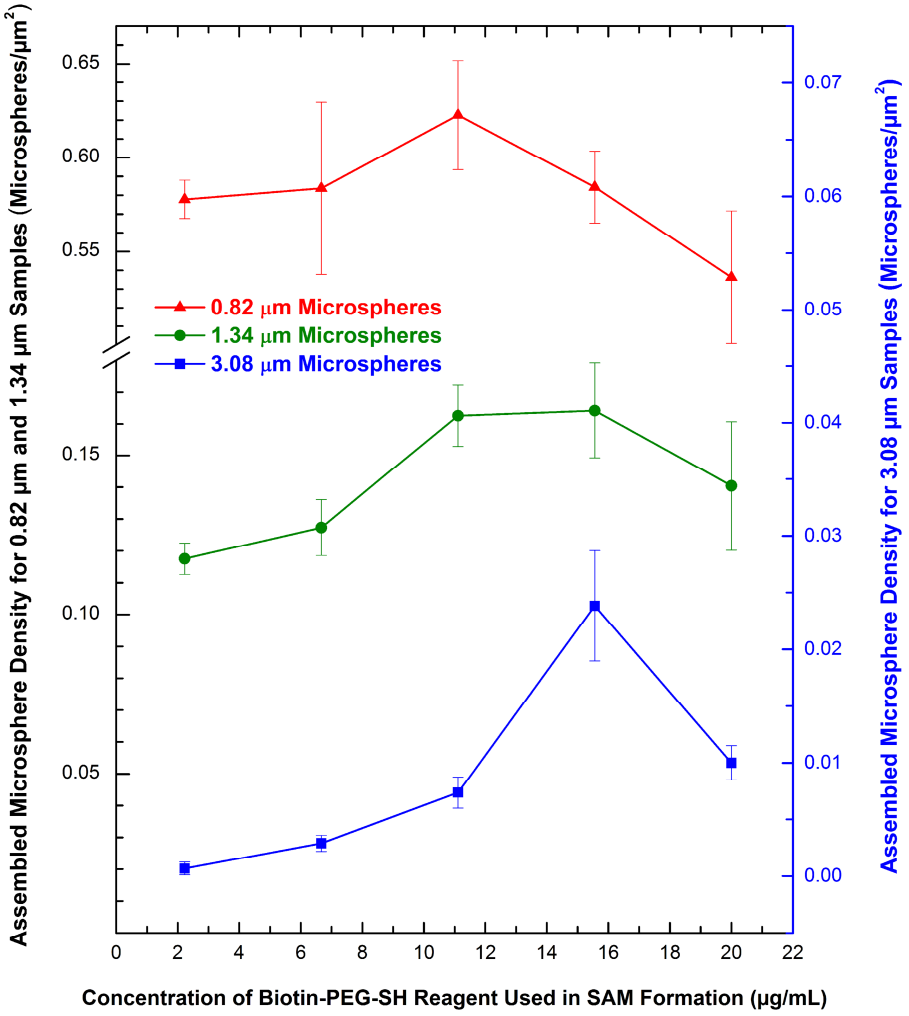

Figure 4.5: This graph of the results from Table 2 plots the average assembled microsphere density (from ImageJ analysis) vs. the concentration of biotin-PEG-SH reagent that was used during the SAM formation. The results from all three microsphere sizes that were tested are included in this plot. It should be noted, however, that they are all scaled differently so that they can all be shown on the same plot.

In the silicon microtile self-assembly experiments of Chapter 5, a few biotin-PEG-SH reagent concentrations were also tested. The best self-assembly yield and selectivity results, however, were actually achieved using a lower reagent concentration of 8.89 µg/mL. This deviation can be explained by

the fact that a different sized substrate (the SOI microtile substrate) was functionalized with the biotin-PEG-SH/methoxy-PEG-SH mixed monolayer in these experiments. Different volumes of SAM formation solutions were used, and the new substrate likely had a lower per area proportion of gold surface area exposed due to the different gold border on the pattern. Since the performance of the mixed monolayer SAM was so sensitive to the amount of reagent used, it is very difficult to predict the optimal amount for a certain experiment without testing a range of concentrations, like the experiment in this chapter. Moreover, even after performing experiments like this one, the exact optimal reagent concentrations cannot necessarily be adapted towards different devices geometries; they only provide a helpful approximate range. When using large volumes of functionalization solution (1.5 mL in this case) and low concentrations of reagents, only a small proportion of the molecules present in the solution will actually take part in the SAM formation. This is what makes it so difficult to predict parameters like the optimal reagent concentration or the total number of reagent molecules that should be present in the SAM solution. When forming SAMs on devices that have a very large exposed functional surface area compared to the volume of functionalization solution, such as the dense colloidal solution of gold nanoparticles that Perrault *et al*. used a similar SAM forming procedure for, a much higher proportion of the available SAM forming molecules in the solution will attach to the gold. [120] Therefore, a more precise reagent concentration could be calculated based on the available gold surface area and the desired molecular density of the SAM.

For example, in this experiment, a 9 mm x 6.5 mm silicon substrate with ~16% of its area patterned with gold was functionalized. Therefore, there was $\sim 9.5\times10^{12}$ nm^2 of available gold area to be functionalized. Using 1.5 mL of the 11.11 µg/mL concentration biotin-PEG-SH (10 kDa) functionalization solution, there would be $\sim 1\times10^{15}$ molecules of biotin-PEG-SH in the solution. If 100% of these molecules took part in forming the SAM, there would be ~105 molecules/nm^2 of the biotin-PEG-SH on the gold surface. However, in Perrault's study on forming similar biotin-PEG/methoxy-PEG mixed monolayers on gold nanoparticles for the purpose of binding with avidin, it was found that the optimal reagent concentration of biotin-PEG-SH molecules in the solution was one that allowed for a maximum

molecular density ~0.6 molecules/nm^2 on the surface of the gold. [120] Assuming that a similar order of magnitude was also optimal in this experiment, it can be concluded that less than 5% of the available biotin-PEG-SH molecules in the 1.5 mL solution actually took part in the SAM formation. This is because such a large volume of low concentration reagent solution was used in order to fully submerge the 9 mm x 6.5 mm substrate in the solution. There are other methods requiring much lower proportions of reagent volumes to the available surface area that may be used to form SAMs like this one. For example, a small volume of high concentration solution can be dropped onto the substrate and then spread over the surface by a cover slip placed on top. However, this method is not suitable for the SOI microtile substrates of Chapter 5 because the substrates are so fragile. Anything that can break the SiO_2 pillars and release the microtiles from the substrate before the sonication release step is detrimental to the yield of the final self-assembly. This is the reason why the method of submerging the substrate in a low concentration reagent solution was chosen for this experiment.

4.2.1. Clustering Analysis

Following the procedure outlined in section 4.1.5, histogram plots were constructed for each of the biotin-PEG-SH reagent concentrations that were tested in the 0.82 μm and 1.34 μm microsphere batches. The purpose of these histogram plots was to analyze the amount of clustering in each sample by looking at the average number of neighbouring microspheres within specific sets centroid-to-centroid distance bin ranges. The *2d* bin (containing counts for centroid-to-centroid distances ranging from 1x the average microsphere diameter to 2x the average microsphere diameter) was the focus of the analysis, as this bin showed the average number of 'near neighbour' microspheres that were very close to each other. For each reagent concentration, the histogram plots (like the one in Figure 4.3 for example) were constructed for three out of the five images taken. These three images were chosen because their assembled microsphere density results most closely matched the average results of the 5.

To compare the amount of assembled microsphere clustering that occurred between each reagent concentration, a reference data set was required. Therefore, for each of images that were analyzed and each of the histograms that were created, a second theoretical histogram was created to represent a

random distribution of the same number of microspheres across the target pad. Equation 4.2 was used to compute the average number of neighbouring microspheres that were expected to be counted in each bin in this random distribution histogram:

$$N_{bin,\,predicted\ average} = \frac{(L_y - \frac{2Bin_{upper}}{\pi})}{L_y} \cdot \frac{\pi N_{assembled}\,(Bin_{upper}^2 - Bin_{lower}^2)}{L_x L_y}. \qquad (4.2)$$

This equation includes a correction factor to account for the boundary effects of the 25 µm wide target pads. Its derivation and a detailed explanation of each variable are included in section 8.1 of the appendix chapter. Equation 4.2 was used to generate the random distribution data (pictured in red) in the histogram of Figure 4.6, which compares this predicted data directly side-by-side with the observed data from the histogram in Figure 4.3 (pictured in blue).

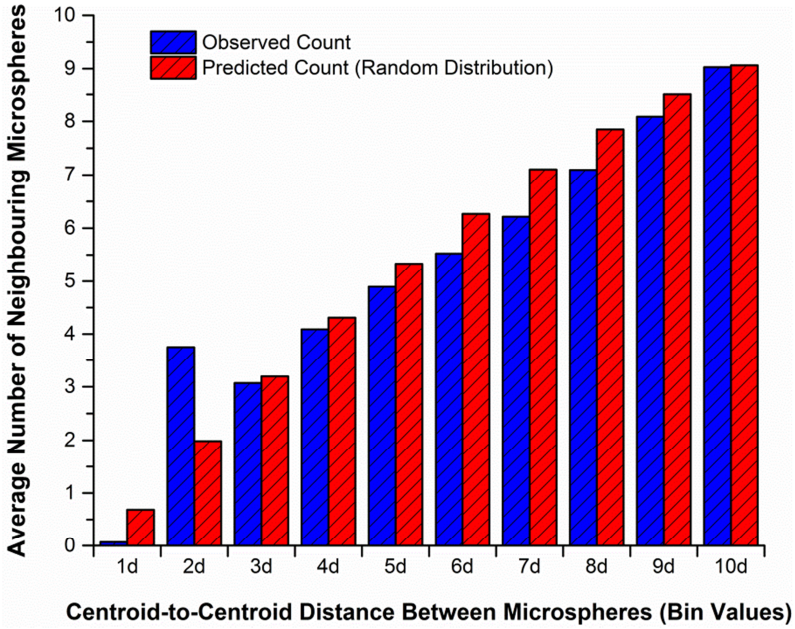

Figure 4.6: The same neighbouring microspheres histogram from Figure 4.3 (in blue) but with an added random distribution histogram (red) inserted next to it for visual comparison.

A general observation that can easily be seen from Figure 4.6 is that the observed histogram is very similar to the random distribution histogram with the exception of the *1d* and *2d* bins. The *1d* bin is different because the random distribution histograms do not account for the fact that the microspheres cannot overlap with each other on the target pad surface. This is why there is a significant count in the *1d*

bin of the predicted histogram and then only a very small count in the observed histogram of microsphere pairs that were so close that their centroid-to-centroid distances were less than the average diameter of the sample. The *2d* bin, however, is a very useful reference for comparing the observed amount of clustering to the theoretical random distribution of the same number of microspheres. The difference between the two values in the *2d* bin indicates how much the distribution of assembled microspheres differs from a random distribution in the number of near neighbour (adjacent) microsphere pairs counted. The ratio between the *2d* bin values is a good quantification of the amount of clustering and aggregation that is taking place because a high count of near neighbour microsphere pairs would mean a large amount of aggregation of the microspheres.

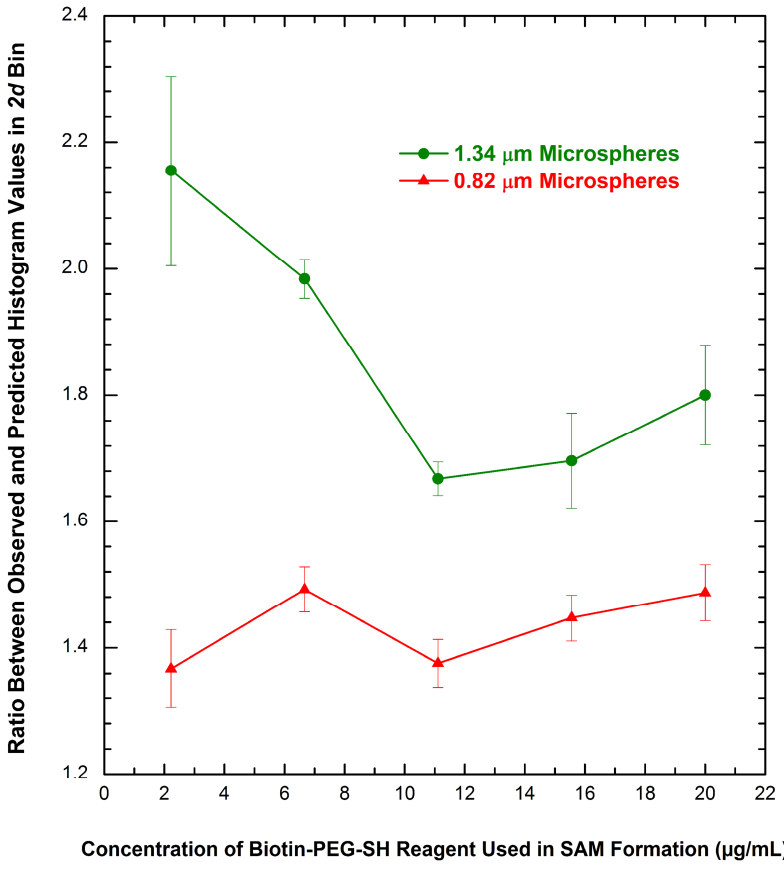

Figure 4.7: Plot of the average ratio between the observed and predicted (random distribution) histogram *2d* bin values vs. the concentration of biotin-PEG-SH reagent that was used during the SAM formation step for the 0.82 µm and 1.34 µm microsphere batches.

For each histogram that was constructed, this *2d* bin ratio was calculated, and the average values of these ratios for each of the different biotin-PEG-SH reagent concentrations tested were plotted against the reagent concentrations in Figure 4.7. The error bars in the plot were computed from the standard deviations in the averaged data. A significant trend was not observed from the 0.82 μm microspheres values. However, the shape of the curve for the 1.34 μm microspheres is very reminiscent (albeit inverted) of the curve from Figure 4.5, which plotted assembled microsphere density vs. biotin-PEG-SH reagent concentration. Inspired by the similarity of these two curves, another graph was constructed where the *2d* bin ratio values for each of the analyzed 1.34 μm microsphere images were plotted against the respective assembled microsphere density of each image.

As can be seen in Figure 4.8, this graph turned out to be linear in nature. A linear fit was employed in Origin to find a slope of -8.72 ± 0.75. Therefore, for the 1.34 μm microspheres, the *2d* bin ratio was directly proportional to the assembled microsphere density with a negative proportionality constant. Because the *2d* bin ratio increases as the assembled microsphere density decreases, this means that the number of near neighbour microsphere pairs increases. Therefore, there is more clustering. Hence, we can conclude from these results that as the assembled microsphere density decreases, the clustering of the microspheres becomes more pronounced. Stated inversely, as the assembled microsphere density increases, clustering of the microspheres becomes less pronounced. This is intelligible because if the assembled microsphere density increased to a maximum point where the entire substrate was completely covered wall to wall with microspheres and no free space, the observed histogram results would exactly match the random distribution results. The entire target pad would be one big cluster at that point so that ratio between the *2d* histogram bins of your observed and predicted results at such high densities would level out to 1. The reason why this relationship was not as clearly observable with the 0.82 μm microsphere data is likely because the assembled microsphere densities in those images were already so high that the differences between the clustered microspheres and the random distribution data were already quite small. As can be seen from Figure 4.7, the *2d* bin ratio values from that set of data were much lower than the ratio values from the 1.34 μm microsphere data set.

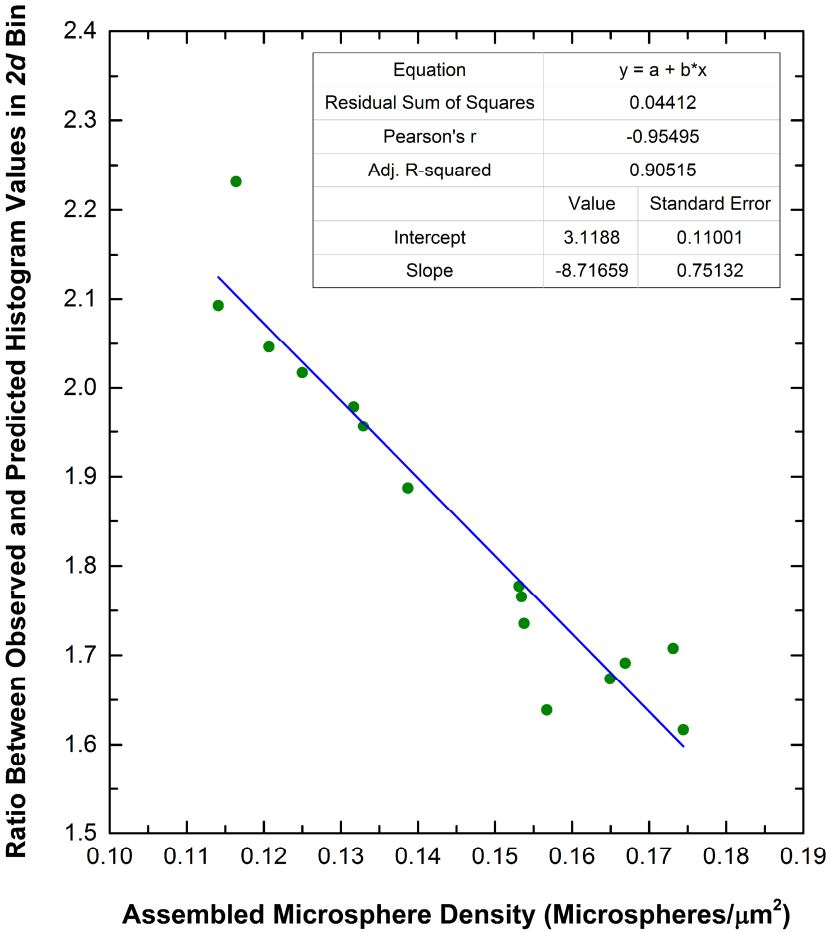

Figure 4.8: Plot of the ratio between the observed and predicted (random distribution) *2d* bin histogram values vs. the assembled microscope density of each of the 1.34 μm microsphere target pad images that was analyzed for clustering. As can be seen from the graph, the values are linearly correlated with each other with negative proportionality constant. A linear fit placed on the data using Origin resulted in a slope of –8.72 ± 0.75.

4.3. Conclusion

The main purpose of the experiments in this chapter was to develop a procedure for forming a reliable, avidin-binding SAM on gold with biotin as the functional group. This procedure was later employed in the experiments of Chapter 5, which involved functionalizing gold-coated silicon microtiles with a biotin mixed monolayer SAM to drive their self-assembly onto avidin-functionalized target sites on a substrate. The performance of the mixed monolayer biotin SAM that was realized in this chapter was evaluated by attempting to selectively self-assemble avidin-coated polystyrene microspheres onto biotin-functionalized gold pads on a target substrate. By using the experimental method outlined in section 4.1, highly selective self-assembly was achieved at a high assembly density, especially with 0.82 μm diameter

microspheres. Three different batches of microspheres with different average diameters were tested. The microspheres with an average diameter of 0.82 μm assembled with the greatest pad coverage and density, followed respectively by the 1.34 μm and 3.08 μm batches. A key parameter in the avidin binding properties of the mixed monolayer biotin SAM turned out to the concentration of the biotin-PEG-SH reagent that was used to form the SAM. With all three of the microsphere batches, experiments were performed that directly compared the resulting assembly density of the microspheres as the biotin-PEG-SH reagent concentration was varied through 5 different concentrations. All three batches demonstrated a peak in the assembly density at reagent concentrations in the range of 9-18 μg/mL, and a trend towards lower concentrations was observed in the data as the microsphere diameter decreased. A clustering analysis was also performed using histograms to compare the average number of near neighbouring pairs of microspheres in each image. From the 1.34 μm batch images, this analysis found that as the assembled microsphere density increased, the clustering of the microspheres became less pronounced when compared to a random distribution of the same number of assembled microspheres on a pad.

5. Avidin-Biotin Driven Die-to-Substrate Self-Assembly of Silicon Microtiles

This chapter outlines and discusses a set of experiments performed with silicon microtiles that were functionalized and self-assembled onto functionalized target gold pads using the avidin-biotin protein-ligand interaction. The semi-covalent sulfur-gold integration was used to form self-assembled monolayers (SAMs) on both the silicon microtiles (gold-coated on one side) and the target gold pads. The avidin protein was the functional group of the target gold pad SAM and biotin was the functional group of the silicon microtile SAM.

5.1. Experimental

5.1.1. Experimental Overview

The microtile fabrication procedure and the self-assembly experimental process are both outlined in the process flow diagram in Figure 5.1. Starting with a silicon-on-insulator (SOI) wafer, gold-coated silicon microtiles were fabricated by sputtering gold onto the silicon device layer, patterning with photoresist to mask squares that would later become microtiles, and then etching both the gold layer and the silicon device layer until the square microtiles were left on the buried oxide layer. The underlying SiO_2 layer was then etched to significantly undercut the microtiles such that they remained supported only by slim SiO_2 pillars. The microtiles were then functionalized with a SAM containing biotin molecules as the functional group. During this functionalization, a target pad substrate patterned with square gold pads was also functionalized with an avidin SAM, which would later be used to bind the biotin-functionalized microtiles. The target pad substrate was made of silicon and was patterned with target pads with the same dimensions as the microtiles (5 μm squares). Once the microtiles were fully functionalized with the biotin SAM, they were released by bath ultrasonication into a solution of phosphate buffered saline (PBS) containing 0.05% polysorbate 20 (PBSP). The sonication was employed to fracture the SiO_2 pillars that anchored the microtiles to the handle portion of the SOI substrate. The avidin-functionalized target pad substrate was then placed in this PBSP solution so that the biotin-functionalized microtiles could be

assembled onto it. Timed cycles of stirring and settling were employed in this assembly step to land the microtiles on the target substrate where they selectively attached to the functionalized gold pads via the avidin-biotin interaction.

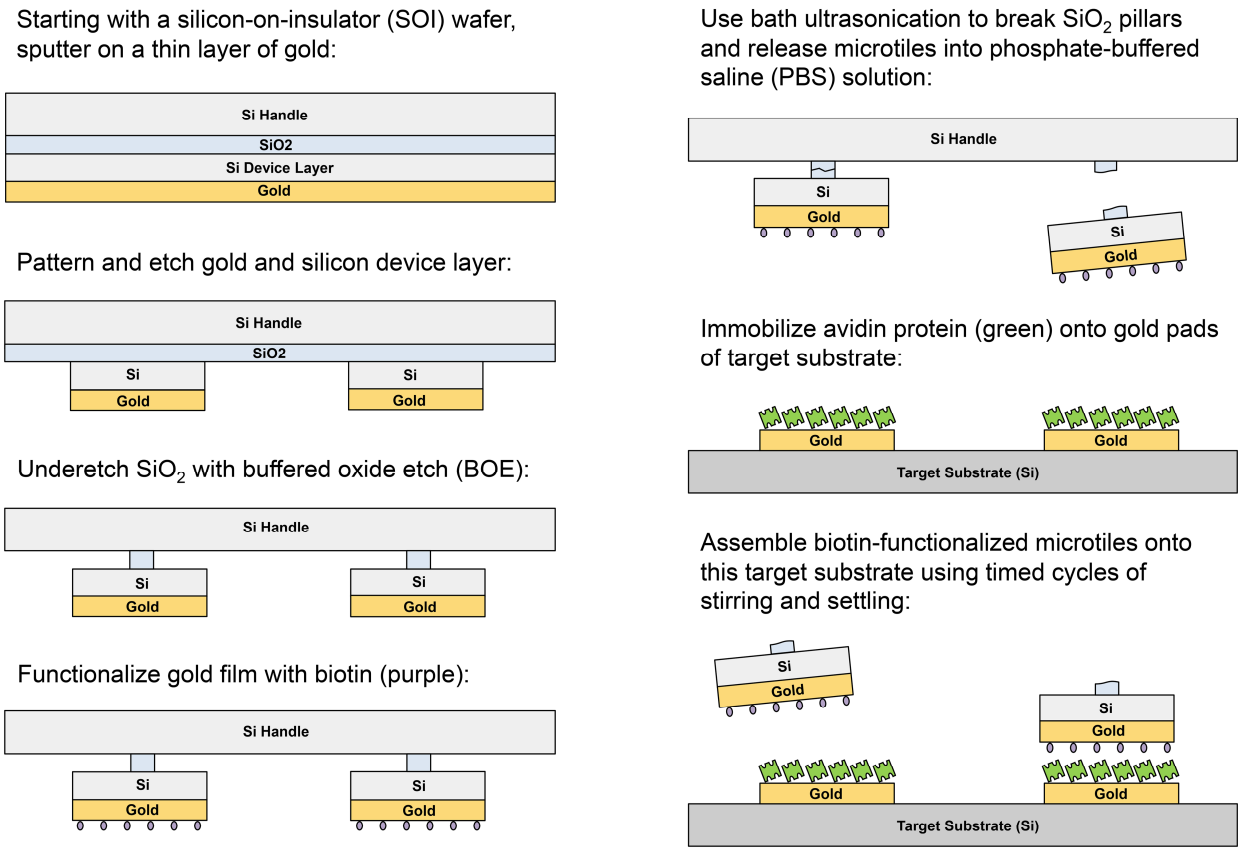

Figure 5.1: Process flow diagram illustrating the entire experimental procedure from microtile fabrication to target substrate and microtile functionalization and finally the assembly of the released microtiles onto target gold pads on the target substrate.

5.1.2. Silicon Microtile Fabrication

In order to investigate the self-assembly capabilities of the avidin-biotin interaction at the microscale, silicon microtiles were fabricated as model components for nanoelectronic integrated circuit chips of the future. These model 'nanochips' were simply microscale silicon tiles, which could also be relevantly sized models for future NEMS chips or nanosensor chips. Square 5 µm x 5 µm microtiles with tile heights of 1.8 µm were the primary device geometries investigated, but rectangular and larger 25 µm wide geometries were fabricated and tested as well. The silicon microtiles were fabricated from p-doped

<110> SOI wafers purchased from Ultrasil that contained a 1.8 µm thick silicon device layer on top of a 2 µm thick buried oxide layer. Once received, the wafer was unpackaged in a cleanroom and cleaned with piranha solution (H_2SO_4 + H_2O_2). It was then spin-coated with a protective layer of Waycoat® HPR-504 photoresist and soft baked at 115°C for 90 seconds to harden the resist. The wafer was then diced into 1 cm x 1.5 cm pieces with a Disco DAD-341 dicing saw. For best results with the dicing saw, it was crucial to ensure that no air bubble were allowed to form between the wafer and the tape that holds the wafer while dicing. These air bubbles can trap silicon dust during the dicing process and can greatly disrupt the cleanliness of each substrate, which is critically requirement for successful microtile assembly. With the 5 µm square pattern, one 1 cm x 1.5 cm substrate could produce roughly 558,000 microtiles.

The purpose of the pre-dicing photoresist layer was to protect the device surface of the SOI wafer from the dirty non-cleanroom environment of the dicing saw, as well as any silicon dust that was released during the dicing process. After dicing, the SOI wafer was taken back into the cleanroom where each 1 cm x 1.5 cm substrate was rinsed with two cycles of acetone/IPA (to remove the photoresist) and then piranha cleaned again. The substrates were then mounted (typically 4-8 at a time) onto a silicon wafer using photoresist and then sputtered with an 8 nm adhesion layer of chromium (42 seconds at 7 mTorr, 150 W) followed by 50 nm of gold (3.5 minutes at 7 mTorr, 80 W) with a planar magnetron sputter system (Floyd). The substrates were then removed from the sputtering wafer, cleaned with acetone/IPA, and patterned one at a time by photolithography. HPR-504 photoresist was spun on at 4000 RPM for 40 seconds to form a ~1.25 µm thick layer and then soft baked at 115°C for 90 seconds to drive off the solvent and harden the resist. The substrates were allowed to rehydrate for at least 30 minutes prior to exposure. Since the substrates were rectangular, a significantly thick edge bead effect was formed at the corners, with two of the corners having more prominent and wider edge beads. Edge beads in non-circular substrates are caused by the viscosity and surface tension properties of the photoresist, which dictate the contact angle and increased photoresist thickness at the solid-liquid-gas interface on the edge of a substrate. [123] Substrates with corners typically suffer from thicker edge beads, which can cause asymmetry in the photolithography because thicker resists require different exposure/development times.

This can be seen from the corners of the substrates in Figure 5.2, which depicts an SOI substrate at various stages of the fabrication procedure.

For consistency between results, the same ABM™ mask aligner (Oscar) in the U of A Nanofab was always used. Since such a small substrate was to be patterned, and the desired pattern on the photomask was not in the center of the mask, a vacuum chuck could not be used to hold the substrate in place during photolithography. The contact vacuum could not be used either. Therefore, the substrate was brought into contact with the photomask using only the mechanical force of the chuck being raised into substrate contact with the photomask, also known as soft contact. This lithography mode cannot provide the minimized feature sizes that are available from vacuum/hard lithography, but with carefully selected exposure and development times, it proved to be sufficient for patterning 5 μm wide squares. The soda lime glass photomask contained an array of 5 μm wide chromium squares (separated by 10 μm) that provided blockage for squares of positive photoresist on the underlying substrate and protected these squares from exposure by the ultraviolet light source. The rest of the photoresist on the substrate was exposed and dissolved away later by developing. Since the contact was not very strong, the lithography process was very sensitive to fluctuations in the cleanroom environment and fluctuations in the strength of the ultraviolet source. Therefore, for each batch of substrates that were fabricated, a few test substrates needed to be exposed and developed first to determine the ideal exposure and development times for that day. For the 5 μm square pattern, typical exposure and development times ranged from 1.7-1.8 s and 26-29 s, respectively, while for the 25 μm square pattern, exposure and development times in the range of 1.9 s and 22 s were optimal. After developing in 345 developer, the substrate was thoroughly rinsed with water and then dried. Figure 5.2A shows an overhead view of a gold-coated SOI substrate just after photolithography has been performed.

The patterned photoresist squares were used to mask and protect the pads against three consecutive etch steps, so that microtiles could be formed. The gold layer was first wet etched away by an 11 second dip in a pre-made etchant solution containing potassium iodide, iodine, and water. The substrate was then dipped in a chromium etchant solution comprised of ceric ammonium nitrate, nitric acid, and water for 18

seconds, so that the Au/Cr film was entirely etched away and only remained in the squares protected by the photoresist pads. As can be seen from Figure 5.2B, the silicon device layer was uncovered at this point. The substrate was then mounted onto a spare wafer again using photoresist so that it could be handled and etched by a reactive-ion etching tool.

With the photoresist pads still on and protecting the squares from etching, the silicon device layer was etched all the way down to the buried oxide layer by an inductively coupled plasma reactive-ion etching tool (STS™ ICP-RIE). As can be seen from Figure 5.2C, this left gold-coated silicon microtiles on top of the buried SiO_2 layer. An unswitched RIE process similar to a Bosch etch was used in the ICP-RIE to obtain a continuous anisotropic etch of the silicon with near vertical sidewalls. In the unswitched recipe, a passivation polymer layer (C_4F_8) was continuously deposited while SF_6 plasma continuously etched the silicon. This SF_6 plasma contained directional ions that attacked and etched the passivation layer and the silicon device layer in the vertical direction so that a near vertical etch through the silicon was performed while the sidewalls remained protected by the passivation layer. As can be seen from Figure 5.3B, the sidewalls of the microtiles appear rough and spongy. This is likely due to the passivation polymer breaking down too quickly during the process and not forming a thick enough layer on the sidewalls to completely protect them from the isotropic etching nature of the SF_6 plasma. After 2.5 minutes of this reactive ion etch, the etch typically made it all the way through the silicon to the buried SiO_2 layer. The

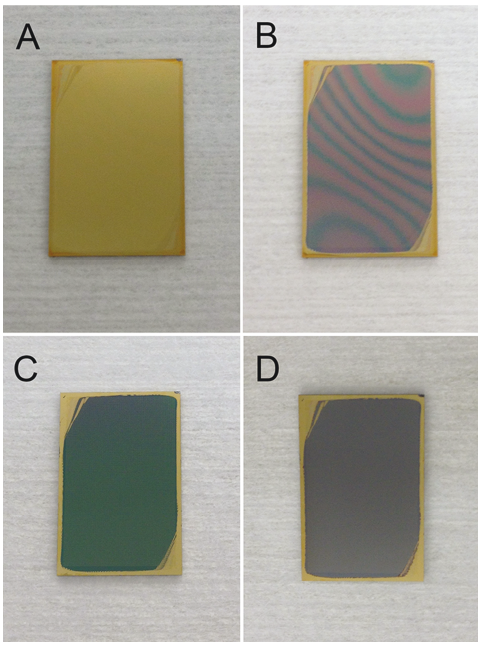

Figure 5.2: Photographs taken from directly above the SOI substrate as it goes different stages of processing. (A) After Cr and Au are sputtered on top of the Si device layer and then the substrate is patterned by photolithography. (B) After Au/Cr wet etching. (C) After Si reactive-ion etching. (D) After BOE undetching of the oxide, leaving the handle Si substrate visible.

photoresist and any residual passivation polymer were then cleaned off of the microtile substrate by low intensity sonication in an acetone bath for 5 minutes.

To release the microtiles into solution, the SOI substrate was held submersed with the gold side of the microtiles facing down in a buffered oxide etch (BOE) solution to wet etch away the buried SiO_2 layer around and underneath the microtiles until only narrow pillars of SiO_2 were left holding the microtiles in place. Once narrow enough, a large majority of these pillars could be later broken in an ultrasonication bath so that most of the microtiles are released into the sonication solution. This can be seen from Figure 5.3, which shows two scanning electron microscope (SEM) images of substrates with microtiles that have been underetched and then bath ultrasonicated so that most of the microtiles have broken off of the substrate, and only a few remain in place. This demonstrates the amount of undercutting and narrowing of the SiO_2 pillars that was required for a high yield of microtiles to be released into the sonication solution. This approach of releasing devices by breaking anchor point pillars via ultrasonication was inspired by a similar approach by Bashir *et al*. [73] A major benefit of this release method was the ability to directly transfer the microtiles into most liquid mediums.

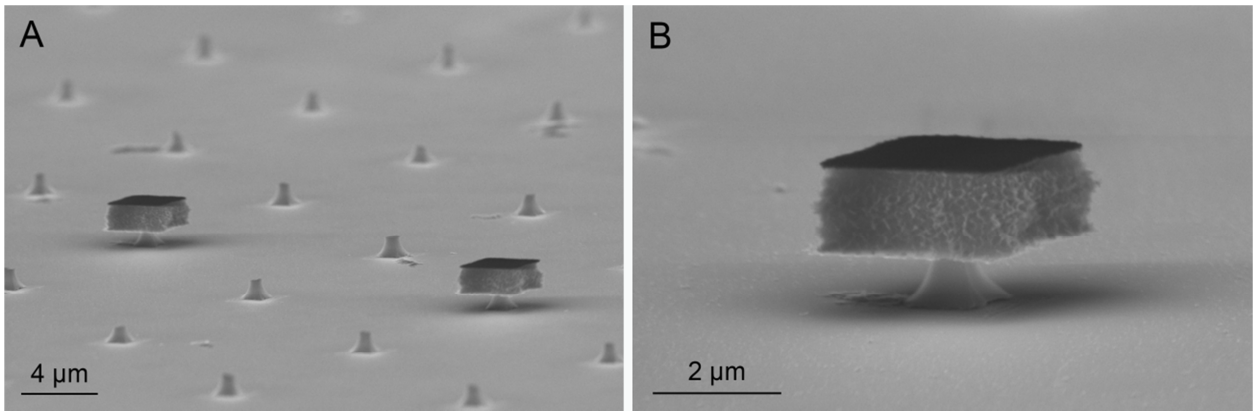

Figure 5.3: SEM images of silicon microtiles fabricated from an SOI wafer. (A) Silicon microtiles with buried oxide layers that have been etched by BOE so that only a narrow pillar of SiO_2 holds the microtile. The substrate in this figure has already undergone bath ultrasonication so most of the microtiles have been released into solution. (B) A closer look at an underetched microtile illustrating the amount of underetching required to break off the tiles with a very high yield during sonication.

For this experiment, the microtiles were released into the final self-assembly medium, which was chosen to be a 1x (pH 7.4) phosphate buffered saline (PBS) solution with 0.05% polysorbate 20 surfactant added (PBSP). When releasing the microtiles into this PSBP solution, the highest attainable release yield was observed when the microtiles were BOE underetched until approximately 15% of them were already released from the substrate due to the underetching and water rinsing alone. At this visual etch-stop point, the oxide pillars were thin enough that 50 minutes of bath ultrasonication in PBSP could release a large majority of the microtiles into solution so that only ~5% of the microtiles remained on the substrate, meaning an approximate release yield of 80%. This was the highest yield observed in PBSP, but yields of over 95% were achieved by sonicating into water or just PBS. Due to slight variations in the average width of the microtiles from batch to batch, the required BOE wet etch time for high yield release needed to be individually determined for each substrate through repeated short cycles of BOE wet etching, rinsing, drying, and observing under a microscope. It usually took ~50 minutes of BOE wet etching to reach this visual etch-stop point where only 85% of the microtiles remained. Figure 5.2D illustrates what the substrate looked like from above at this point in the procedure, with the handle silicon layer of the SOI wafer visible. After BOE underetching and copious water rinsing, the SOI microtile substrate was brought to a chemistry lab for the biotin-SAM formation on the gold sides of the microtiles.

5.1.3. Target Substrate Fabrication

The target gold pad substrates used in this chapter were fabricated by the procedure outlined in Chapter 3.1.2. The 9 mm x 6.5 mm silicon substrates were patterned with 35 nm thick square gold pads that were deposited by evaporation and patterned via photolithography and lift-off. A variety of silicon microtiles were fabricated from SOI wafers (5 μm squares, 25 μm squares, 5 μm x 10 μm rectangles, etc.). For a typical microtile assembly run, the pattern on the target pad substrate exactly matched the pattern on the SOI substrate, so that the microtiles were the exact same size as the target pads upon which they were to land. Some of the target pad substrates also included 500 μm wide gold border sections, as well as regions with various larger pad sizes, as can be seen in Figure 5.6 and Figure 5.7.

5.1.4. Avidin SAM on Target Substrate Gold Pads

The procedure for forming an avidin SAM on the gold pads of the target substrate was the exact same procedure as the one described in Chapter 3.1.3 of this thesis, as this procedure had previously produced great results for binding biotin-functionalized gold nanoparticles. The experimental procedure was initially tested and developed by self-assembling commercially functionalized gold nanoparticles onto the avidin-functionalized gold pads. The avidin SAM formation was based on a similar procedure used by Ding *et al*. on gold electrodes. [116] The functionalization procedure is schematically illustrated in Figure 3.2, which shows the sequential addition of reagents. After the protective photoresist layer on the gold pad target substrate was rinsed off with two cycles of acetone/IPA rinsing, the first step to the SAM formation process was immersing the target pad substrate in a 1 mM solution of 11-mercaptoundecanoic acid (MUA) dissolved in absolute ethanol to form an MUA SAM on the gold pads. Next, the substrate was rinsed and then submersed in a solution of 2-(*N*-morpholino)ethanesulfonic acid (MES), *N*-hydroxysulfosuccinimide (Sulfo-NHS), and 1-ethyl-3-(3-dimethylaminopropyl)carbodiimide (EDC), which formed active *O*-acylisourea intermediates at the ends of the MUA SAM molecules. Finally, the substrate was rinsed again and submersed in a 1 mg/mL avidin protein stock solution so that avidin could become the functional group at the end of the SAM. The *O*-acylisourea esters would react with free amine groups on the avidins to form amide bonds, leaving isourea by-products behind. This avidin functionalization step took place over 60 minutes. After this, the substrate was rinsed with water and placed in a glycine solution for 10 minutes to end the chemical functionalization sequence. After the glycine, the substrate was water rinsed again and then dried. At this point, it was ready to be placed in the final assembly solution containing the functionalized silicon microtiles, which were released into a PBSP solution during this functionalization process.

5.1.5. Biotin SAM on Gold-Coated Silicon Microtiles

The procedure for forming a biotin SAM on the gold-coated microtiles was a direct adaptation of the procedure that was developed in Chapter 4.1.2 of this thesis through self-assembly experiments with avidin-coated polystyrene microspheres. The main difference between this functionalization procedure

and the one described in Chapter 4.1.2 is that, instead of forming this biotin mixed monolayer on a gold pad silicon substrate, this procedure was performed on an SOI substrate with gold-coated microtiles fabricated on it. The other main difference is that the SOI microtile substrate used in this section was larger than the target gold pad substrates of Chapter 4, so larger volumes of functionalization solutions were required. The SOI microtile substrate had approximately 4 times as much gold-patterned surface area on it as the target gold pad substrate, so 4 times as much reagent volume was used in each step. At the point in the fabrication procedure when the microtiles were ready for functionalization, they were still attached to the handle substrate by thin oxide pillars, as described in section 5.1.2. The biotin-terminated SAM formed on the microtiles was a mixed monolayer SAM composed of a longer biotin-PEG-SH chain (10 kDa) and a shorter methoxy-PEG-SH chain (5 kDa). As can be seen from Figure 5.4, which illustrates the two steps of the sequential mixed monolayer formation procedure, the mixed monolayer followed a "trees and grass" structure, with longer biotin-PEG-SH chains (trees) supporting larger biotin molecules that extended over shorter, narrower methoxy-PEG-SH chains (grass).

Based on the experiments from Chapter 4, a few different concentrations of the biotin-PEG-SH reagent were tested, but a concentration of 8.89 µg/mL proved to be the best performing choice for the die-to-substrate self-assembly of the silicon microtiles. When the fabrication of the microtile SOI substrate was complete, the substrate was brought to a chemistry lab for functionalization, keeping the exposure time to the non-cleanroom environment to a minimum. To make the biotin-PEG-SH functionalization solution, a 16 µL volume of 3.33 mg/mL biotin-PEG-SH stock solution (prepared in the same way as in Chapter 4.1.2) was pipetted into a clean 50 mL centrifuge tube. This equates to $\sim 3.2 \times 10^{15}$ molecules of the biotin-PEG-SH. The tube was then topped up to 6 mL with absolute ethanol and vortexed to mix. The 1.0 cm x 1.5 cm SOI microtile substrate was then gently placed into the bottom of the upright tube with the gold sides of the microtiles facing up. The SAM was left to form on the gold-coated microtiles over a period of 2 hours while the solution was gently agitated by a vortexer at 200 RPM (with tape keeping the tube/substrate upright). The methoxy-PEG-SH functionalization solution was prepared by pipetting 40 µL of 3.33 mg/mL stock solution into another clean 50 mL centrifuge tube. This

tube was also filled with 6 mL of absolute ethanol to make a final methoxy-PEG-SH concentration of 22.22 µg/mL, the same concentration that was used in Chapter 4.1.2. Without rinsing, the SOI microtile substrate was transferred into this new functionalization solution and also left gently vortexing at 200 RPM for 40 minutes. After 40 minutes, the microtiles were fully functionalized and ready to be released into the final assembly solution (PBSP). The microtile substrate was rinsed with water, clamped with Nalgene™ polypropylene forceps, and held microtile-side down in a 50 mL centrifuge tube filled with 27.5 mL of PBSP for the sonication release.

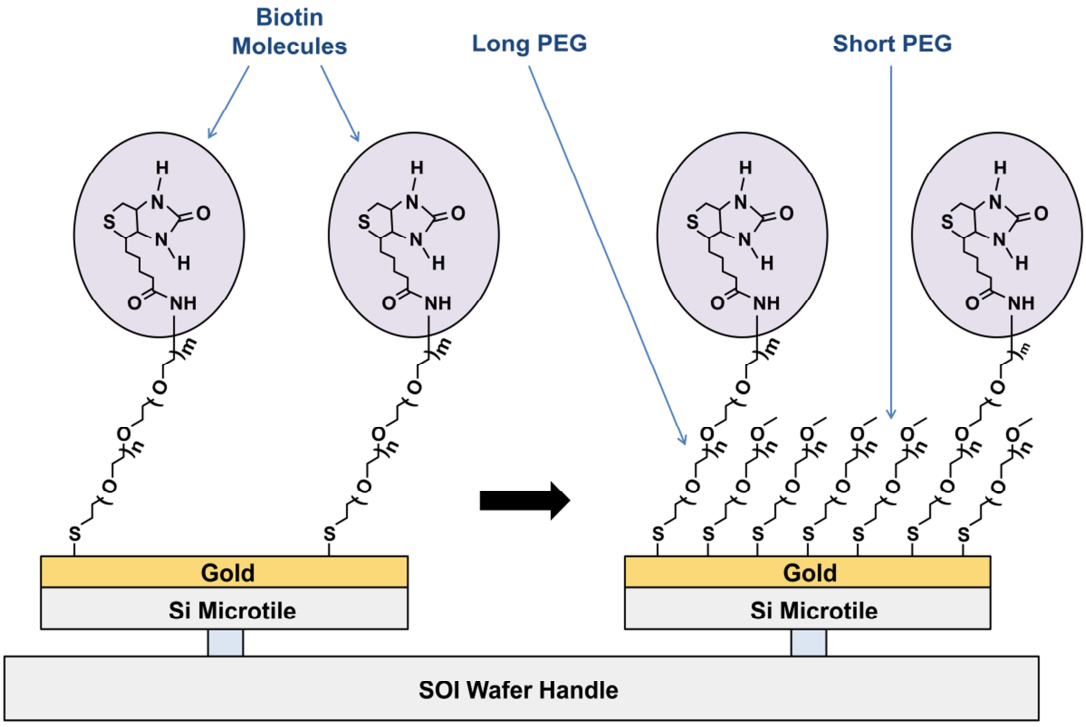

Figure 5.4: Schematic illustration of the procedure used to form the biotin SAM on the gold-coated silicon microtiles (while they remained fixed on the handle substrate by thin SiO_2 pillars). The sequential addition of longer biotin-PEG-SH chains (molecular weight of 10 kDa) and then shorter methoxy-PEG-SH chains (5 kDa) formed a mixed monolayer SAM with spaced apart biotin molecules available at the surface of the monolayer. From the molecular weights of these PEG chains, it can be estimated that n in the figure is approximately equal to 111, while m is approximately equal to 108.

5.1.6. Microtile Sonication Release Procedure

The biotin SAM functionalization of the gold-coated microtile substrate was performed concurrently with the avidin SAM functionalization of the target gold pad substrate. The biotin SAM

functionalization, however, was completed about 90 minutes before the avidin SAM functionalization was finished. This was to allow time for sonication release of the microtiles from the SOI substrate into solution. Using the yellow stand and PBSP-filled 50 mL centrifuge tube pictured in Figure 5.5A, as well as forceps holding the microtile substrate upside down in the centrifuge tube solution, these components were all placed in a bath ultrasonicator filled with water. The water level reached the same height as the 27.5 mL of PBSP in the centrifuge tube. Many bath sonicators were tested for this release process, but a 280 W Elmasonic S30H sonicator from the NINT cleanroom demonstrated significantly higher yield results that any other. The sonication forces were able to break the majority of the SiO_2 pillars so that the microtiles were released into the PBSP solution, which was the final solution for the assembly process to take place in. After 50 minutes of sonication at 35°C, the microtile substrate was removed and lightly rinsed, leaving most of microtiles in the PBSP solution. After leaving the tube to sit for 10 minutes so that the microtiles could settle to the bottom, the volume of PBSP in the tube was pipetted from 27.5 mL down to 10 mL by pipetting from the top.

5.1.7. Microtile Self-Assembly Procedure

After the microtiles were released into solution and the volume of the microtile solution was pipetted down, the gold pad target substrate was ready to be placed into that microtile solution so that the self-assembly process could start. After the glycine step of the avidin SAM procedure, the gold pad substrate was rinsed with water, gently dried with nitrogen, placed on a cleanroom wipe to dry, and glued onto an SEM stub with Krazy Glue®. While waiting for the glue to quickly dry, a small magnetic stir bar (1/8”) was placed into the centrifuge tube and the microtiles in solution were stirred for 10 seconds. The SEM stub was then placed on a lathed cross-shaped holder that had a hole drilled in the middle of it to fit an SEM stub. The substrate, SEM stub, and cross holder were then all placed into the PBSP filled centrifuge tube that contained the microtiles. With the SEM stub in the cross holder, the substrate could sit flat in the centrifuge tube (gold pads facing up) while a magnetic stir bar underneath could stir the solution. This is advantageous because the stir bar can mix microtiles up into the solution above the gold pad target substrate, and then it can be turned off to allow the microtiles to settle onto the substrate due to

gravity. Images of the self-assembly set-up, including the magnetic stirring hotplate, 50 mL centrifuge tube, magnetic stir bar, cross holder, SEM stub, and target pad substrate, can all be seen in Figure 5.5.

A timer apparatus was built to control when the stir bar was active. A magnetic stirrer controlled the stir speed (set to 235 RPM) and the timer apparatus controlled when the magnetic stirrer turned on and off. The timer apparatus was built by a previous Master's student, Jason Ng. [124] A circuit diagram schematic of it can be found in Figure 8.2 of the appendix. For this experiment, the magnetic stirrer repeatedly cycled on and off in 1 minute intervals over 24 hours. The induced lifting and settling of the microtiles brought about their assembly and attachment to the target gold pads. After 24 hours and some final settling time, the target gold pad substrate was removed from the solution, rinsed with HPLC water from a spray bottle, and dried with nitrogen.

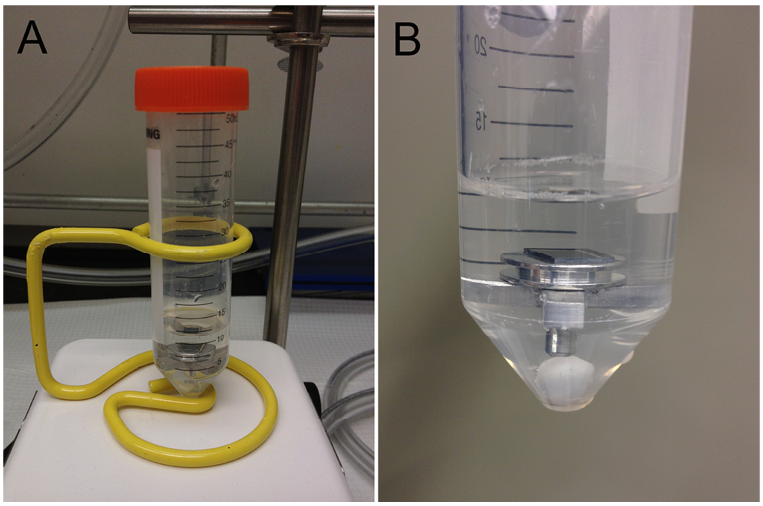

Figure 5.5: Photographs of self-assembly setup. (A) Magnetic stirring hotplate with a centrifuge tube on it being held vertically by a yellow stand. (B) A closer look at the contents of the centrifuge tube (from bottom to top): 1/8" magnetic stir bar, cross-shaped holder, SEM stub, target gold pad substrate super-glued onto SEM stub.

5.1.8. Yield-Reducing Experimental Variations

The experimental procedure outlined above was developed over many months of trials and experimental variations. The procedure described was the iteration that demonstrated the best microtile assembly yield and selectivity results to date. Many experimental variations were found through testing to be disadvantageous to the final assembly yield. These experimental variations are as follows: excluding polysorbate 20 in the final PBS assembly solution, using a high concentration of biotin-PEG-SH reagent during the biotin SAM formation, using evaporation as opposed to sputtering to deposit the target

substrate gold pads, centrifuging the microtile solution before pipetting the volume down to 10 mL, and using older (expired) reagents.

It was observed through experimental variations that higher microtile release yields (up to 95% as opposed to 85%) were possible when sonicating into just PBS instead of PBS with 0.05% polysorbate 20. This is likely because the polysorbate surfactant may exhibit a mild dampening effect on the sonication, so that the SiO_2 pillars must be very narrow in order to break them with a high yield. Experimental attempts where the functionalized microtiles were released into just PBS, and the same PBS solution was used for the final assembly step, demonstrated low assembly yield and selectivity. Therefore, the inclusion of this surfactant may be very important for the avidin-biotin binding mechanism to work. However, in further experimental variations where the microtiles were released into PBS and then the polysorbate was added to the solution for the assembly to take place, selectivity was improved but observed yields were still low. It is postulated that the polysorbate surfactant may also serve to protect the self-assembled monolayers (SAMs) on the microtiles from damage during the ultrasonication step.

Initial microtile assembly experiments were attempted using much larger concentrations of the biotin-PEG-SH reagent, as it was initially hypothesized that saturating the surface with biotin molecules would be beneficial. However, as was also found through experiments with avidin-coated microspheres in Chapter 4, a lower biotin-PEG-SH concentration in the range of 10 µg/mL produced the best self-assembly results. The reason for this is predicted to be that as the number of biotin molecules in the PEG SAM becomes more concentrated, the SAM becomes more disordered, with biotin units possibly buried in the monolayer. This has been observed in previous studies of similar biotin mixed monolayers. [122], [125]

The target pad substrates were always fabricated by photolithography, deposition, and then lift-off, but two gold-chrome deposition sources were experimented with to deposit the pads. Controlled experiments with both showed that pads deposited by evaporation performed better in terms of microtile assembly yield than pads deposited by sputtering. One possible explanation for this is that the crystal structure or atomic arrangement in the evaporated gold layer may be better suited for a well-structured avidin SAM. Another possible reason is that the multidirectional sputtering process left behind small

ridges on the pad edges when lift-off was performed. These small ridges (verified by SEM) could be large enough to impair the ability of the microtiles to come in close enough contact with the pads for the two SAMs to meet and bind in some microtile orientations. It is predicted that a smooth and very flat gold surface on both the target pads and microtiles is essential for high yield assembly with this SAM-based binding mechanism.

To perform the release of the microtiles into solution via bath ultrasonication, the microtiles needed to be released into a volume of 27.5 mL, so that the height of that volume of solution in a 50 mL centrifuge tube would match the height of the water in the sonicator. After this step, the volume of microtile solution was reduced down to 10 mL for final assembly by pipetting from the top. In an attempt to not lose any microtiles during the pipetting, it was hypothesized that the tube could be centrifuged at a low RPM setting to force all of the microtiles to the bottom. Experiments employing this centrifugation of the tube before pipetting resulted in significant reduction in yield. This is likely because the centrifugation forced all of the microtiles to stack onto each other at the bottom of the tube, which likely caused damage to the SAMs. In the best performing procedure, the tube containing the microtiles was left to settle for at least 10 minutes before pipetting instead of centrifuging.

Since many of the reagents used in this experiment are time sensitive, using fresh reagents greatly improved the microtile assembly yield. The key experimental reagents to have fresh (within the last 6 months) for the experiment are avidin, Sulfo-NHS, EDC, and the surface reactive PEG derivatives biotin-PEG-SH and methoxy-PEG-SH. All of these were stored frozen at -20°C, with the exception of Sulfo-NHS, which was stored refrigerated at 4°C. Although many of the solutions in the experiment can be made in large volumes and then stored for reuse as stock solutions, it was found by experiment that the Sulfo-NHS/EDC/MES carboxyl activator solution must be prepared in water immediately before usage. The Sulfo-NHS and EDC powder-form reagents are very moisture sensitive, so they were stored in heated sealed moisture barrier bags with desiccant pouches. The EDC reagent in particular is very unstable in aqueous environments. [117]

5.1.9. Yield and Selectivity Measurement

In order to determine the yield and selectivity of microtiles assembled onto target gold pads across the entire substrate for the most successful run, two counts were required: the total number of microtiles that had landed on gold pads and the total number of microtiles that had landed on the background silicon substrate (not on the gold pads). To perform this count, the target substrate was mounted onto a software controlled X-Y translation stage under a confocal microscope and the entire substrate was imaged by controlled stepping. This was achieved using an Olympus LEXT Confocal Microscope at 10X magnification and the following imaging settings: size of 768, profile of 64, and brightness of 242. After the substrate was rotationally aligned in the X and Y directions, it was carefully stepped over and captured in 30 images (5 rows and 6 columns). Since the gold pads were patterned in an array, each image was taken so that it contained exactly two rows or columns of gold pad overlap with the image adjacent to it. The total on/off pad microtile count was performed by manual visual inspection of each image. To avoid counting with large numbers, each image was further cropped into four sections, counted, and then entered into a spreadsheet for totaling the counts at the end. To avoid count overlap between images, any microtiles in the bottom two rows or right two columns of each image were omitted from counting unless they included the bottom or right edges of the substrate. A microtile was considered 'on' (successfully assembled onto) a target pad if its area overlapped any portion of the square gold pad in the microscope image. On the other hand, a microtile was counted as 'off' if it did not at all overlap the gold pad, and it was entirely located on the surrounding silicon area.

To verify accurate stepping and imaging across the substrate, digital photostitching software called PTGui was used to accurately stitch all 30 images together. This confirmed that exactly two rows/columns of gold pad overlap were included between each image across the substrate, as no errors in image overlap were found during photostitching. To perform the photostitching in PTGui, the following settings were used: focal length of 17,300 mm, focal length multiplier of 1, rectilinear lens type, exposure correction setting enabled, and at least 5-10 control points entered manually between each adjacent pair of images. In addition, to further verify the manual microtile count, an ImageJ analysis was performed on

the entire panorama photostitch. A threshold of 82 was used to convert the original confocal microscope photostitched image to binary, and this threshold left all of the pads and silicon white while all of the microtiles were black. Therefore, the ImageJ analysis could be used to count all of the microtiles on the substrate, on or off the target pads. The pixel/μm scale in ImageJ was set using the 5 um width of a random pad and the *analyze particles* function was used to count the total number of microtiles. A size setting of 23-60 μm^2 and a circularity setting of 0.05-1 were used for the ImageJ particle count. This image analysis resulted in a count that equaled the exact sum of the manual counts for microtiles on and off the pads, confirming the accuracy of the manual count. The photostitched confocal microscope images and the results of the ImageJ analysis can both be seen in Figure 8.3 of the appendix. A very similar technique of taking microscope images, photostitching them together, and then using ImageJ to count the total number of microtiles was also used for the large area (border area) microtile counts discussed in the beginning of Chapter 5.2.

5.2. Results & Discussion

The microtile assembly experiment outlined above was performed many times, with generally reproducible results, although two particular runs performed far better than any of the others. The SEM images shown in Figure 5.6–Figure 5.9 were all taken from these two runs. A LEO 1430 SEM microscope was used to capture these images using a 20.0 kV EHT accelerating voltage. A variety of sizes and shapes were tested for the microtiles and as well for the target features onto which the microtiles were assembled. Figure 5.6 shows an SEM image demonstrating the selective self-assembly of 5 μm square silicon microtiles on a large patterned gold section of a silicon substrate. The yield of microtiles assembled onto the gold portion (pictured grey) is very high compared to the yield of microtiles assembled onto the silicon section (pictured black).

Over the entire substrate, the density of microtiles assembled onto the gold section was calculated to be 999 microtiles/mm^2, and the selectivity of the microtiles assembling onto the gold section over the silicon section was calculated to be 23.5:1. These values were calculated by taking microscope images across the substrate, photostitching the images together using PTGui, and then counting the number of

microtiles on each of the two sections (gold or silicon) using ImageJ. Figure 5.7 also demonstrates the strong selectivity of microtiles attaching to patterned gold areas over the background silicon substrate when the target areas were larger than the 5 µm microtiles.

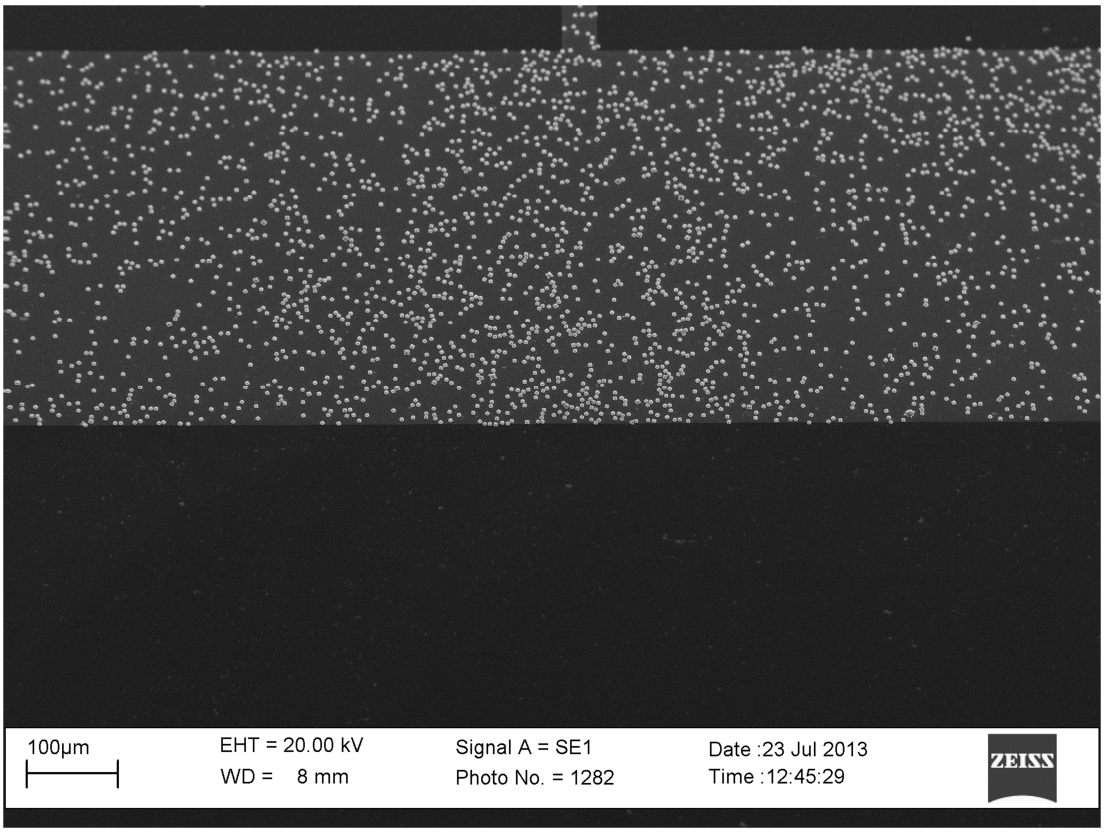

Figure 5.6: SEM image of 5 µm square silicon microtiles selectively self-assembled onto a large gold area (pictured grey) instead of the silicon substrate (pictured black). An assembled microtile density of up to 999 tiles/mm^2 was achieved on large gold areas.

Figure 5.8 demonstrates 5 µm silicon microtiles that have landed on target gold pads of the same size (5 µm squares). Figure 5.8A demonstrates the typical range of tile position and alignment that can be seen across the substrate. In the best performing run, there were very few microtiles left on the silicon substrate and not attached to a gold pad. Although most of the microtiles were found on top of target gold pads, the alignment and the degree of overlap between each gold pad and the microtile greatly varies across the substrate. Figure 5.8B shows a microtile completely overlapping and very well aligned with its square gold pad. This was not a rare occurrence across the substrate, but the majority of microtiles were not as well aligned.

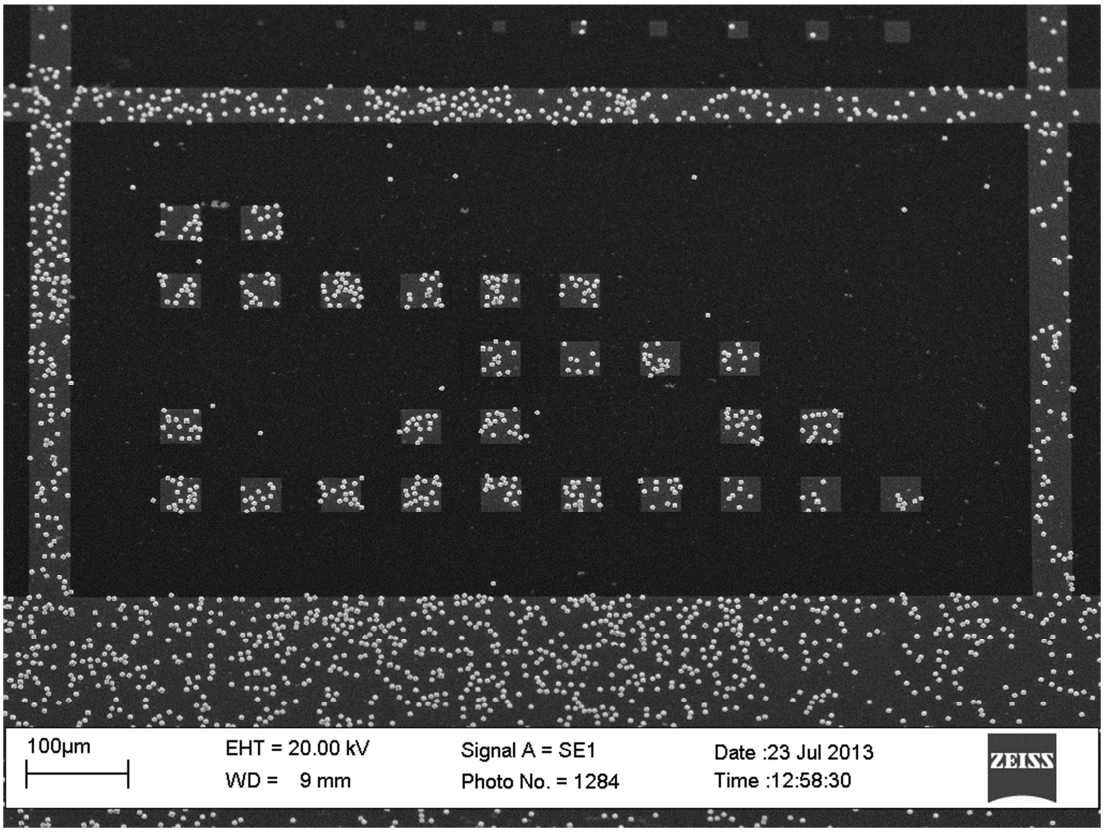

Figure 5.7: SEM image of 5 µm square silicon microtiles selectively assembled onto wide gold pads and stripes with high selectivity.

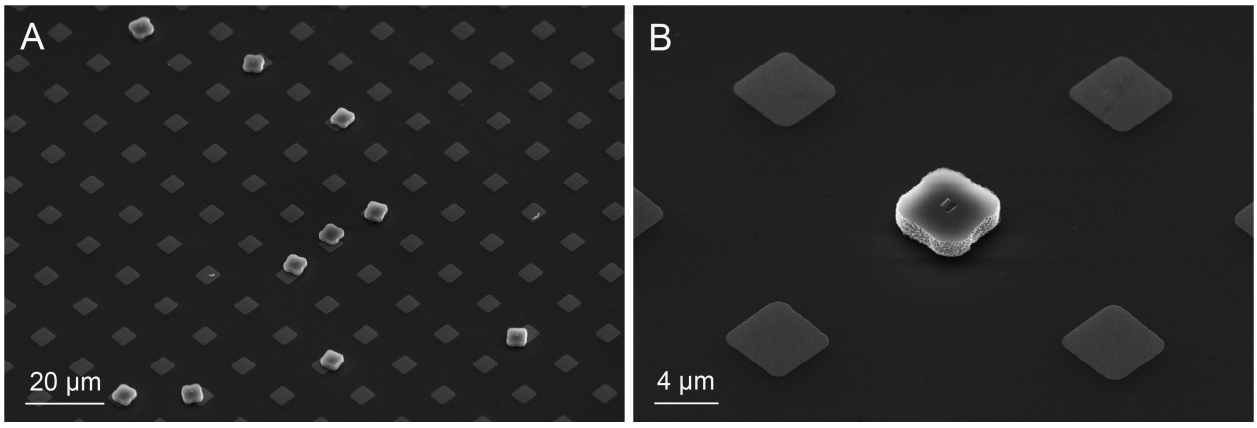

Figure 5.8: SEM images of 5 µm square silicon microtiles that have landed on target gold pads of the same size. (A) The typical yield, selectivity, orientation and degree of pad overlap that can be seen between the microtiles and target gold pads across the wafer. (B) A 5 µm square microtile that is completely overlapping and very well aligned with its target gold pad.

5.2.1. Selectivity and Yield

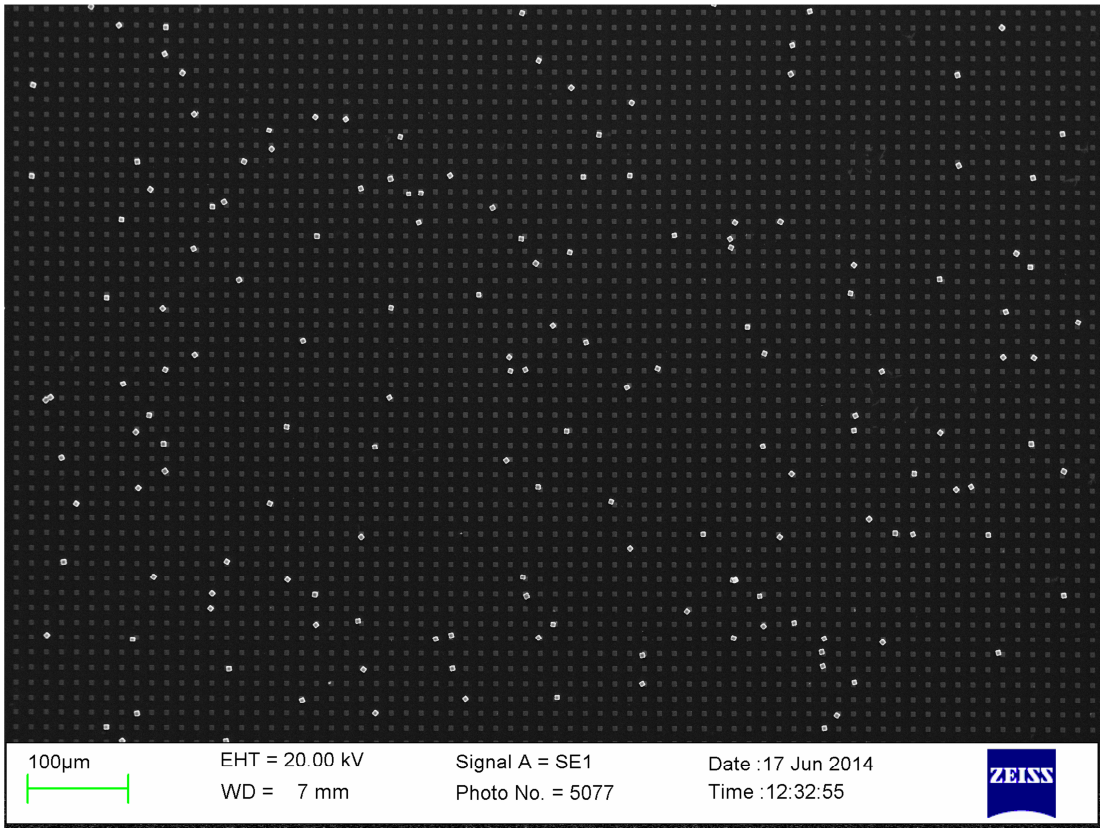

Figure 5.9: A large area SEM image illustrating the yield and selectivity of 5 µm square silicon microtiles assembled onto 5 µm square gold pads across the target substrate. 2.05% of the target gold pads were covered by microtiles and the selectivity ratio of microtiles on the pads as opposed to off of the pads was found to be 7.32:1.

Figure 5.9 is a large area SEM micrograph showing a section of the target substrate after the most successful microtile assembly run with 5 µm square silicon microtiles assembling onto 5 µm square gold pads. While showing just a small portion of the substrate, this image well-demonstrates the yield and selectivity achieved by this method. As outlined in Chapter 5.1.9, the entire substrate was also imaged in translational sections by a confocal microscope. After all of the microtiles on the substrate were counted by visual analysis of each image, the final count over the substrate added up to 2853 microtiles overlapping with target gold pads (‘on’ the pads) and 390 microtiles located on the intervening silicon substrate (‘off’ the pads). This means that the selectivity ratio of microtiles assembling onto the gold pads as opposed to the silicon substrate was 7.32:1. The substrate contained 139,334 target gold pads in total,

so having 2853 of the pads covered by assembled silicon microtiles implies a yield of 2.05%. In Figure 8.3A of the appendix, the entire substrate can be seen in a large area (7 mm x 4.5 mm) photostitched image of 30 confocal microscope images. The total assembled microtile count after an ImageJ analysis can also be seen in Figure 8.3B, with the successfully assembled microtiles labeled in green and the microtiles on the background silicon (off of the pads) labeled in red.

The target substrate contained 5 μm wide square target pads spaced out in an array so that the distance between each adjacent pad was 10 μm, and the center-to-center spacing was 15 μm. This means that ~11.1% of the target substrate was covered by gold target pads. However, to make a comparison between the observed results and a random distribution of the same number of microtiles landing and sticking on the substrate, a larger available target pad area must be considered. Microtiles that landed on the gold pads with only a small fraction of area overlap were counted as assembled microtiles, so any microtile having their center of mass land within 2 μm of the outer perimeter of a target pad would have been counted as successfully assembled. Therefore, using a 9 μm x 9 μm area for each target pad, it can be estimated that microtiles would be counted as successfully assembled if they landed with their centers of mass on 35.8% of the available wafer area. Therefore, if all 3243 of the total assembled microtiles had just landed on the substrate in a randomly distributed fashion, the yield of gold pads covered by microtiles would have been 0.83% and the selectivity ratio of microtiles assembled onto gold pads as opposed to the silicon substrate would have been 0.56:1. When compared with the actual results of the microtile distribution (2.05% and 7.32:1 respectively), this comparison with randomly distributed microtiles demonstrates the significance of the experimental results and the true nature of the binding selectivity.

Although the highest achievable yield of microtiles released into solution was ~80%, there were still more microtiles in the assembly solution than the number of available pads for the microtiles to land on. The size of the target pad substrate (made from the same mask) was always chosen to be ¼ of the original size of the microtile substrate. Therefore, the ratio of available microtiles in the solution to the available target sites was slightly greater than 3:1. Although this process was only able to attach a small proportion of the total number of microtiles fabricated, it may still be useful when microtile fabrication

costs are low and insignificant compared to the ability to assemble such small devices, as may be the case with 5 µm wide devices. By increasing the number of available microtiles in solution by large amounts, even by orders of magnitude, it is likely the yield of target pad sites covered with microtiles could also be greatly increased. There have also been self-assembly mechanisms proposed that use fluidic chambers and pumps to recycle chips in solution to continuously flow them over target substrates and repeatedly reuse the devices that do not attach. [6], [49], [30]

5.2.2. Microtile Shape and Size Variations

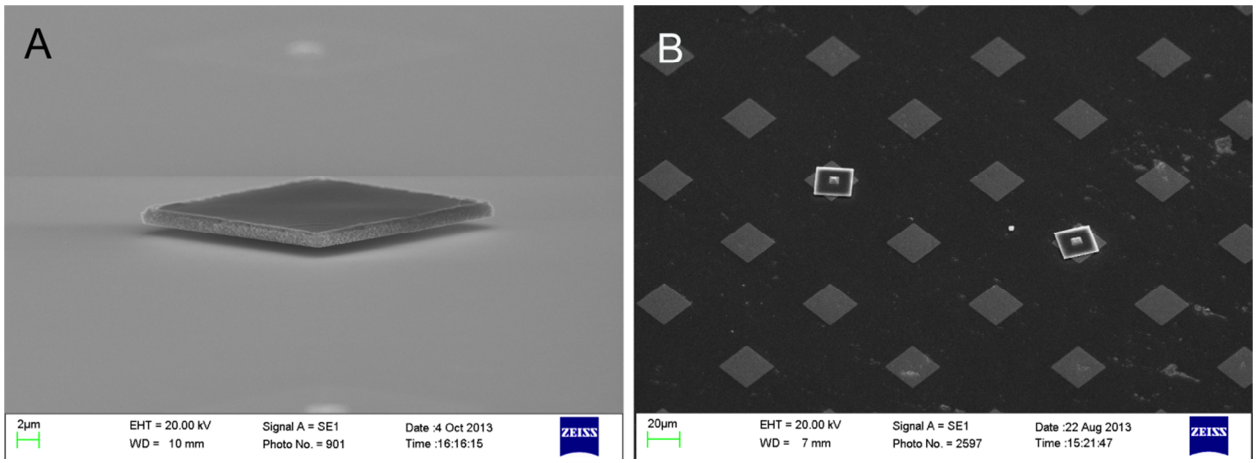

Figure 5.10: SEM images demonstrating the fabrication and assembly of 25 µm wide square silicon microtiles that were made and tested using similar procedures to the 5 µm microtiles discussed earlier. (A) A 25 µm wide microtile that has been BOE underetched and still remains on the SOI wafer after sonication release has released most of the surrounding microtiles on the substrate. (B) 25 µm square silicon microtiles affixed to 25 µm wide target gold pads with a high selectivity but poor yield.

This die-to-substrate assembly process was also tested on larger 25 µm silicon microtiles fabricated from the same SOI wafer (device layer thickness of 1.8 µm, oxide layer thickness of 2.5 µm) as the 5 µm microtiles were. With the larger microtiles, significant trends in orientation were again not observed and the yield of attached microtiles was also low, but a good selectivity was observed. An advantage seen with the larger 25 µm square microtiles was that much larger release yields (up to 99%) were achievable through the underetching and bath ultrasonication release method. An SEM image of a 25 µm microtile that has been underetched but still remains attached to the SOI substrate can be seen in Figure 5.10A. In the most successful demonstration, only 18 out of a potential 22,000 microtiles that were fabricated,

functionalized, and released into the PBSP solution from the SOI substrate successfully landed on the 25 μm wide square target pads and remained after rinsing. However, only 2 microtiles were found on the surrounding silicon substrate, giving a selectivity ratio of 9:1 (target pads:silicon substrate). An SEM image demonstrating the successful affixing of two of the 25 μm tiles can be seen in Figure 5.10B.

Experiments with microtiles of different shapes other than squares were also attempted. Figure 5.11 shows the fabrication and assembly of 5x10 μm rectangular microtiles that were landed on target pads of the same size using the exact same procedure that was outlined in section 5.1. Unfortunately, with the rectangular microtiles, it was much more difficult to reach a high release yield from the ultrasonication release method. This was because the non-symmetrical nature of the rectangular microtile meant that a fin instead of a pillar was left behind holding the microtiles to the SOI substrate after the buried SiO_2 layer was underetched. These fins can be seen in Figure 5.11A, an SEM image taken on an SOI substrate after sonication had released a majority of the rectangular microtiles into solution. The fin connection between the microtiles and the oxide layer results in much less precision and control when attempting to underetch the substrate to a point where a high yield of the microtiles will break off after sonication. For example, with the 5 μm square tiles, underetching to a point where only 85% of the tiles remained would lead to an ~80% release yield (only 5% of microtiles would remain after sonication). However, with the 5x10 μm rectangular tiles, underetching until only 85% of the tiles remained, and then sonicating, only led to a ~35% yield of microtiles released (~50% of the microtiles remained on the substrate). This much lower release yield led to poor assembly results with the rectangular microtiles, although an SEM image of one particularly well aligned microtile attached to a target pad can be seen in Figure 5.11B. An analysis was performed measuring the angles at which every rectangular microtile landed with respect to their target pads, but no significant trends in orientation were observed.

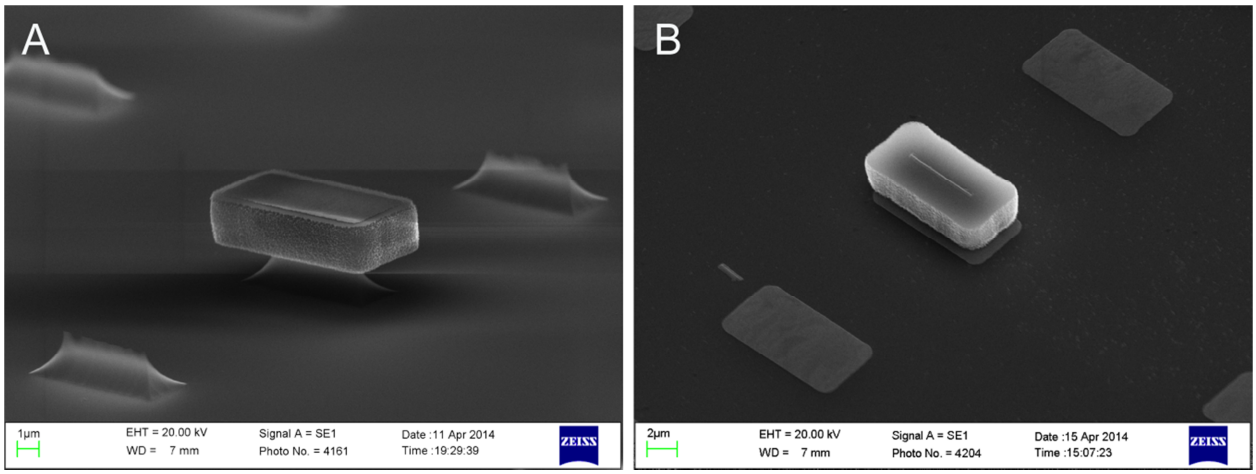

Figure 5.11: SEM images demonstrating the fabrication and assembly of 5x10 µm rectangular microtiles that were fabricated using the exact same procedures as the 5 µm square microtiles. (A) A 5x10 µm rectangular microtile that has been BOE underetched and still remains on the SOI wafer after sonication release has released of most of the surrounding microtiles. (B) A 5x10 µm rectangular microtile that has successfully landed on a target pad of the same size.

5.2.3. Discussion

It can be concluded that the successful assembly and binding of the functionalized microtiles to the gold pads was due to the avidin-biotin interaction because of the low yield assembly in control experiments that were performed to verify that the avidin-biotin interaction was driving the assembly. For example, if either the avidin protein or the biotin ligand attachment steps were left out of the procedure, the observable yield of microtiles assembling and sticking to the substrate (gold or silicon) was very low (on the order of magnitude of 1 of out 100,000 microtiles). Since the yield of microtiles sticking to the silicon portion of the target substrates was much higher when both avidin and biotin were used, it is apparent that the chemistry used in one or both of these SAMs increases the tendency for the microtiles to stick to silicon.

It is predicted that for microtiles of this size and mass, the avidin-biotin interaction induces a mild at best effect on the orientation of the microtiles as they are falling and landing on the target substrate. During the settling period of the timed cycles, the force of gravity likely dominates, and the tiles likely fall and land on the substrate in the same manner that they normally would due to gravitational forces in a fluid. However, whether or not they stick to the substrate and remain there through many cycles of stirring and settling and rinsing at the end is dependent on the avidin-biotin interaction. The rate of

sticking is also likely a function of the surface area overlap that a functionalized microtile shares in connection with a target gold pad after landing. The more avidin-biotin connections that form should lead to stronger attachment. This can be concluded because of the very strong observable selectivity that the microtiles demonstrated landing on the target gold pads as opposed to the silicon substrate across the entire substrate.

An important factor in the microtile design that likely contributed to the success of these results was the SiO_2 stubs that were left behind on the backside of the microtiles after they were released into solution by sonication. This SiO_2 stub can be seen clearly in Figure 5.8B. When a microtile lands with its stub side down on a surface, it is much less likely to stick to that surface due to limited surface area in contact with the substrate. This can be inferred because when the target substrates were observed after assembly, it was a very rare occurrence to see microtiles landing gold side up the gold pads or on the silicon substrate. If microtiles were stuck to the substrate after rinsing cycles, they almost always had their gold side down, facing the substrate. It is likely that, during the stirring and settling step of the experiment, many microtiles landed on the substrate with their stub side down and that they could be brought back up into solution when the stirring phase started again because of the stub and its prevention of stiction. The stub likely increased the overall assembly yield because it gave those microtiles another chance at landing on a gold pad with their functionalized (gold) side down.

Although this experiment demonstrated a respectable yield and selectivity, the alignment of some of the assembled microtiles may not be satisfactory for some applications. It is likely that for devices of this size, the avidin-biotin interaction only acts as a 'smart glue', binding specific devices together if they are brought into contact in a suitable configuration, but not actively orienting them as they come together into a specific arrangement. However, this is only an initial demonstration of the concept, and there are possible additional steps and optimizations that could be performed to significantly improve the alignment of the microtiles. For example, since the avidin-biotin interaction can be reversibly broken and reformed in nonionic aqueous solutions at temperatures near 70°C, [89] it is possible that many cycles of heating and cooling could help the microtiles to realign themselves into more aligned, lower energy

conformations on the target pads. Gentle heating and cooling cycles near 70°C have been used in polymerase chain reactions (PCR) to demonstrate the reusability (up to 4 cycles) of biotinylated DNA molecules and streptavidin-coated beads that were dissociated from each other and reassembled during the subsequent cycles. [89]

5.3. Conclusion

It was demonstrated in this chapter that the selective self-assembly of microscale semiconductor devices onto patterned target substrates is possible at moderate yields and selectivities when driven by the avidin-biotin interaction. Gold-coated silicon microtiles (model 'nanochips') were successfully fabricated from an SOI substrate, functionalized with the biotin-PEG/methoxy-PEG mixed monolayer SAM from Chapter 4, and then released into a PBS/polysorbate solution to be assembled onto a patterned target substrates that was functionalized with the avidin SAM from Chapter 3. A key feature of the fabrication technique was the front side release of the microtiles from the SOI substrate by ultrasound fracture of the narrow SiO_2 pillars that held the microtiles onto the SOI substrate. These SiO_2 pillars were formed during a BOE etch step that undercut the buried oxide layer beneath the silicon microtiles. After the avidin-functionalized target substrate was placed in the PBS/polysorbate solution that the microtiles were released into, assembly was achieved by intermittently stirring the solution over a period of 24 hours. The best assembly results were achieved with 5 µm wide microtiles versus 25 µm wide ones. When attempting to land the microtiles on large gold areas, a very high assembled microtile density of 999 microtiles/mm^2 was achieved at a selectivity ratio of 23.5:1 (large gold area: large silicon area). When attempting to land the 5 µm square microtiles onto matching 5 µm target pads on a substrate, this assembly mechanism yielded 2.05% of the total target pads covered by assembled microtiles at a selectivity ratio of 7.32:1 in favour of the target pads as opposed to the silicon substrate. Rectangular 5 µm x 10 µm microtiles and 25 µm square microtiles were also successfully landed on matching target pads, but at a much lower assembly yield.

6. Single-Stranded DNA Driven Microtile Self-Assembly

This chapter discusses a set of self-assembly experiments where single-stranded DNA oligonucleotides are employed to drive the assembly 5 μm wide silicon microtiles. In contrast to the avidin-biotin interaction, using DNA to drive such assembly is a very attractive approach because DNA can offer some significant advantages. Since single-stranded DNA oligonucleotides can easily be synthesized with a specific base sequence, DNA driven self-assembly allows for extensive capabilities in programmability. [24], [126] If the designer of the experiment has full control of which base sequences are used on specific microtiles and specific target sites, many different microtiles could be assembled onto programmed target sites based on which oligonucleotide the SAM on that target site contains. Another attractive feature of DNA is the ability for double stranded DNA to dissociate (melt) into two independent strands at a certain temperature, and then recombine (hybridize) back into double stranded form when the temperature is lowered. Although the avidin-biotin interaction offers some promise for reversibility, [89] the repeatable melting and hybridization capabilities of DNA have been well studied and employed throughout a great amount of research. [127], [128], [129]

Following the exact same concept, process flow, and fabrication techniques as the silicon microtile experiments from Chapter 5, the goal of the experiments in this chapter was to adopt the DNA hybridization mechanism and apply it to the microtile assembly procedures that were developed and demonstrated in the previous chapter. Previous work by Yesudas *et al*. from this research group had focused on using single-stranded DNA (oligonucleotides) as the driving force behind microtile self-assembly. [130], [131] Although these attempts gave promising results for functionalizing gold surfaces with single-stranded DNA, actual attempts at microtile assembly were not successful. Since Yesudas' microtile fabrication methods were not the same as the ones described in this thesis, it was decided that an attempt should be made combining Yesudas' functionalization methods with the fabrication, release, and assembly methods from Chapter 5 in order to test out the possibilities of DNA driven self-assembly of 5 μm wide silicon microtiles. The assembly mechanism in this chapter was driven by the hybridization

interaction between two complementary single-stranded DNA oligonucleotides. Sulfur-gold induced self-assembled monolayers (SAMs) were again used to form two complementary monolayers of single-stranded DNA on both the silicon microtiles (gold-coated on one side) and target gold pads onto which the microtiles were to be assembled.

6.1. Experimental

The experimental procedure followed the exact same process flow as is shown in Figure 5.1, but with the avidin and biotin SAMs replaced by single-stranded DNA SAMs. The target pad substrate fabrication procedure (silicon substrate) was the same as is described in Chapter 3.1.2 and the microtile fabrication procedure (SOI substrate) was the same as is described in Chapter 5.1.3. The microtile sonication release and assembly procedures of Chapters 5.1.6 and 5.1.7 were the same as well. One slight difference in these procedures, however, is that instead of performing the sonication release (and the following assembly procedure) in phosphate buffered saline + 0.05% polysorbate 20, the sonication release and assembly were performed in 2x standard saline phosphate ethylenediaminetetraacetic acid (SSPE), a DNA hybridization buffer. The SSPE buffer had a pH of 7.4 and contained 0.02 ethylenediaminetetraacetic acid (EDTA) and 0.298 M NaCl, in a 0.02 phosphate buffer. The major difference in this experimental procedure from Chapter 5 was in the SAM formation.

Once both the target pad substrate and the microtile substrate were finished fabrication and were ready for functionalization, they were both functionalized simultaneously over an overnight period of ~18 hours. Complementary oligonucleotides were synthesized by a company called TriLink BioTechnologies and shipped in lyophilized solid form. Each of the oligonucleotides contained -SH groups at one end so that gold-thiol based SAMs could be formed on the target gold pads and gold-coated silicon microtiles. The manufacturers warned that the thiol ends might dimerize during shipping and storage, so a *tris*(2-carboxyethyl)phosphine (TCEP) reducing agent was used to reduce any disulfides back into thiols immediately prior to the SAM formation. The specific sequences of the complementary oligonucleotides that were purchased were (5' to 3') CTC CAA ATT TGC TGA A–Spacer 18–Spacer 18–uracil–C_3–SH and TTC AGC AAA TTT GGA G–Spacer 18–Spacer 18–uracil–C_3–SH, where Spacer 18 denotes

hexaethylene glycol, a six unit long PEG chain. A phosphodiester DNA backbone was used for both oligonucleotides. Other than the length of the spacer group, these were the exact same oligonucleotides as the ones used by Yesudas *et al*. in previous experiments. [130] A longer PEG spacer chain was chosen for this experiment because it was expected that this longer chain would give the SAMs a little bit more flexibility to expand and contract when interacting with the complementary DNA SAM to form the appropriate DNA hybridization bond.

When the two oligonucleotides were received from the manufacturer, they were both dissolved in triethanolamine (TEA) buffer solutions to make two 1 mM stock solutions (one for each variety). This was then aliquoted into smaller amounts which were then frozen for storage. The aliquoted amounts were used so that each time the oligonucleotides were required for an experiment, they did not need to go through any more thawing/freezing cycles than one. The TEA buffer was made by dissolving 4.490 g of triethanolamine in 80 mL of HPLC water and then ~24 mL of 1 M HCL was added to adjust the pH to 7.00. The final volume was then diluted with water to 200 mL, to make a final concentration of 0.150 M. To make the SOI microtile substrate functionalization solution, 60 µL of the first 1 mM oligonucleotide was added to a clean 50 mL centrifuge tube, then 16 µL of 0.5M Pierce Bond-Breaker™ TCEP was added, and then the final volume was diluted up to 6 mL with TEA buffer. After gently vortexing to mix, the SOI microtile substrate was submersed in the solution and left upright overnight. The target gold pad substrate functionalization solution was made in a similar manner, but the other oligonucleotide stock solution was used, and only $\frac{1}{4}$ of the total volume was made because the target pad substrate contained $\sim\frac{1}{4}$ of the amount of gold surface area. So 15 µL of the second 1 mM oligonucleotide solution and 4 µL of Pierce TCEP solution were used, and the final volume was diluted to 1.5 mL with TEA buffer. The target pad substrate was also submersed upright in this solution and left to functionalize overnight.

The next day, 27.5 mL of 2x SSPE hybridization buffer was poured into a clean 50 mL centrifuge tube. The SOI microtile substrate was removed from its functionalization solution, rinsed with water (without drying), clamped in polypropylene forceps, and placed microtile-side down into the centrifuge

tube solution, ready for sonication release. This substrate was then sonicated in the solution without external heating for 50 minutes. The Elmasonic S30H sonicator from Chapter 5.1.6 was used for this as well. After 50 minutes, the substrate was pulled out of the solution, and almost all of the microtiles had been released into the SSPE solution. As in Chapter 5, the SOI microtile substrate had been BOE underetched so that only ~85% of the microtiles remained. Since a different sonication solution was used in this chapter, however, even higher sonication release yields were possible. Approximately all 85% of the microtiles that remained on the SOI substrate after underetching were successfully released into the SSPE solution.

After being brought back to the chemistry lab where the target pad substrate had been left functionalizing, the microtiles in the SSPE solution were left to settle for 10 minutes, before having the volume of the solution pipetted (from the top) down to 10 mL. The target pad substrate was then pulled out of its functionalization solution, lightly rinsed with water, and dried. It was then glued to an SEM stub with Krazy Glue® and placed into the microtile solution held upright (gold pads facing up) by a cross-shaped SEM stub holder. Right before doing this, a small magnetic stir bar (1/8") was placed into the centrifuge tube, and the microtiles in solution were stirred for 10 seconds. The timer apparatus was then set up in the same way as described in Chapter 5.1.7 to cycle through stirring (235 RPM) and settling intervals (1 minute each) over 24 hours. After 24 hours, the stirring was disabled and the target pad substrate was taken out, rinsed with HPLC water from a spray bottle, dried, and imaged with a scanning electron microscope for evaluation of the assembly.

6.2. Results & Discussion

The results from these experiments demonstrated that using complementary single-stranded DNA oligonucleotides to drive the selective self-assembly of 5 μm wide microtiles is possible, but at a very low yield. SEM images of the typical assembly yield and microtile alignment can be seen in Figure 6.1A. In similar fashion to the results of Chapter 5, no significant trends towards alignment of the microtiles were observed, although some microtiles did end up well aligned on the target pads and others ended up well centered, like the microtile pictured in Figure 6.1B.

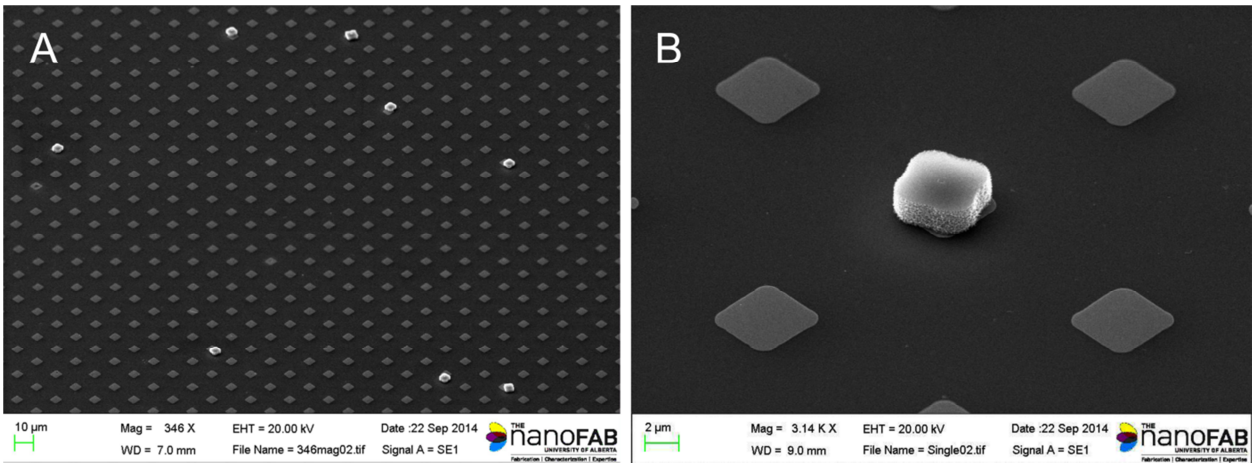

Figure 6.1: SEM images demonstrating the successful low-yield assembly of 5 µm wide square silicon microtiles driven by complementary single-stranded DNA oligonucleotides. (A) A lower magnification SEM image demonstrating the low assembly yield but good selectivity of the microtiles landing on the target gold pads as opposed to the background silicon substrate. (B) A higher magnification SEM image showing a microtile affixed to a target gold pad.

Similar counting techniques to the ones described in 5.1.9 were used to assess the assembly yield and selectivity by counting the number of microtiles on and off the target gold pads. In the best resulting run of this assembly scheme, a total of 389 microtiles were counted on the pads and 118 were counted off of the pads over the entire substrate. As in Chapter 5, the target substrate contained 139,334 target gold pads in total. Therefore, the yield of target pads covered by microtiles in this experiment was only 0.28%. The selectivity of microtiles assembling onto the functionalized gold pads as opposed to the silicon substrate was also lower than demonstrated in Chapter 5, at only 3.30:1. Although these results demonstrate the possibility of DNA driven microscale assembly, they are inferior to the results of the same experiment performed using the avidin-biotin interaction to drive the assembly (which produced a yield of 2.05% and a selectivity ratio of 7.32:1). Although it is possible that further improvements could be made to the procedure to attain better assembly results with DNA driven self-assembly, it is also possible that the DNA hybridization binding interaction is simply not strong enough for high yield assembly at the microscale. The same conclusion was made by Morris *et al*. after DNA-driven assembly attempts by McNally, Bashir, and Lee proved unsuccessful with 8.5 µm wide silicon islands in the early 2000s. [6], [74]

6.3. Conclusion

The results from this chapter demonstrated that microscale die-to-substrate self-assembly driven by complementary single-stranded DNA oligonucleotides is possible, but these initial attempts resulted in a much lower yield than what was achieved when the avidin-biotin interaction was used as the driving force. The exact same experimental techniques that were described in Chapter 5 were used to fabricate, release, and induce the assembly of the microtiles. Complementary oligonucleotide SAMs, however, were instead used to functionalize the gold-coated microtiles and the gold target pads. When attempting to land 5 μm square microtiles on matching 5 μm square target pads on a substrate, this assembly mechanism yielded 0.28% of the total target pads covered by assembled microtiles at a selectivity ratio of 3.30:1 in favour of microtiles affixed to the target pads as opposed to the surrounding silicon substrate. These results demonstrate that the hybridization forces of complementary DNA strands are strong enough to induce assembly of microscale semiconductor devices. However, they may not be as effective as the avidin-biotin interaction, which demonstrated more compelling results in Chapter 5.

7. Conclusion and Future Work

The experiments in this thesis were carried out in order to determine the potential for biomolecular recognition interactions to be used for the selective self-assembly of microscale components onto patterned substrates. Two mechanisms of selective adhesion through biomolecular recognition were explored and tested in this thesis: the strong protein-ligand interaction between avidin and biotin and the hybridization interaction that occurs between two complementary single-stranded DNA oligonucleotides. The concept of avidin-biotin driven die-to-substrate self-assembly was initially tested at the nanoscale with 100 nm diameter biotin-functionalized gold nanoparticles. The results from these experiments demonstrated that this assembly mechanism was very effective, with assembly yields as high as 7.9% of the total available nanoparticles assembling onto large patterned gold areas at an average selectivity ratio of 11.3:1 in favour of the gold pads (which were functionalized with an avidin SAM) as opposed to the surrounding silicon substrate. By introducing a low intensity IPA bath sonication step into the target substrate post-assembly cleaning procedure, this observed selectivity result was be improved to a ratio of 83.5:1, but at the cost of reducing the final assembly yield by a factor of $\sim\frac{2}{3}$. Although the nanoparticles were purchased pre-functionalized with a biotin SAM, attempted variations in this experiment procedure and the resulting nanoparticle assembly yields were used to develop a recipe for forming a biotin-binding avidin SAM on gold target pads. This recipe was used again in later experiments for self-assembling microscale semiconductor devices onto patterned substrates.

Another set of experiments in this thesis involved self-assembling submicron scale avidin-coated polystyrene microspheres onto biotin-functionalized target gold pads. Using the resulting assembly density to judge the avidin-binding capabilities of the biotin SAM, these experiments were performed to develop a procedure for forming a reliable, avidin-binding SAM on gold with biotin as the functional group. It was found that a biotin-PEG/methoxy-PEG mixed monolayer SAM formed in two sequential steps with very tight control of the biotin-PEG-SH concentration is a very successful functionalization method for selectively binding avidin-coated components. A variety of microsphere sizes were tested,

ranging from 0.82 μm to 3.08 μm in diameter. Although the 0.82 μm microspheres assembled onto the target pads with the greatest pad coverage and density, all three microsphere sizes demonstrated a peak in the assembly density at biotin-PEG-SH reagent concentrations in the range of 9-18 μg/mL. The data also demonstrated a trend towards lower concentrations as the microsphere size decreased. A clustering analysis was performed using histograms to compare the average number of near neighbouring pairs of microspheres in each image. From the 1.34 μm batch images, this analysis found that, as the assembled microsphere density increased, the clustering of the microspheres became less pronounced when compared to a random distribution of the same number of assembled microspheres on a pad.

The avidin SAM that was developed and tested in the gold nanoparticle experiments and the biotin SAM that was developed and tested in the polystyrene microsphere experiments were both employed for larger scale assembly experiments leading toward the ultimate objective of self-assembling microscale semiconductor devices onto patterned target sites on a substrate. Gold-coated silicon microtiles (model 'nanochips') were successfully fabricated from an SOI substrate, functionalized with the biotin-PEG/methoxy-PEG mixed monolayer SAM, and then released into a PBS/polysorbate solution to be assembled onto a patterned substrate containing target gold pads that were functionalized with the avidin SAM from Chapter 3. A key feature of the fabrication technique that was developed in this thesis was the front side release of the microtiles from the SOI substrate by ultrasound fracture of the undercut SiO_2 pillars that held the microtiles onto the substrate. This technique proved to be a very convenient method for releasing the fabricated and functionalized semiconductor devices into any liquid medium of choice. Through experimentation, a PBS/polysorbate solution was chosen to be the assembly medium. After the biotin-functionalized microtiles were released into this solution, a target pad substrate with gold pads functionalized with the avidin SAM recipe from the nanoparticle experiments was placed into the PBS/polysorbate solution as well. Successful assembly of 5 μm wide silicon microtiles was achieved at moderate yields and selectivities by intermittently stirring the solution over a period of 24 hours. When attempting to land the microtiles on large gold areas, a very high assembled microtile density of 999 microtiles/mm^2 was achieved at a selectivity ratio of 23.5:1 (large gold area: large silicon area). When

attempting to land the 5 µm square microtiles onto matching 5 µm target pads on a substrate, this assembly method yielded 2.05% of the total target pads covered by assembled microtiles at a selectivity ratio of 7.32:1 in favour of the gold target pads as opposed to the silicon substrate. These results demonstrate the potential for this assembly process to be useful for assembling microscale components when the component fabrication costs are low and insignificant compared to the ability to assemble such small devices, as a very low yield of the available fabricated devices were actually attached onto the substrate using this method.

Rectangular 5 µm x 10 µm microtiles and 25 µm square microtiles were also successfully attached to target pads with matching sizes, but at a much lower assembly yield, introducing some of the limitations of this assembly process. A major limitation was that the sonication release method was only able to release square microtiles at a high yield, but other shapes such as rectangles resulted in much lower release yields. A DNA-driven approach to the self-assembly of 5 µm wide silicon microtiles was also attempted using the same experimental techniques that were previously used for the avidin-biotin driven microtile assembly. The exact same procedures were used to fabricate, release, and induce assembly of the microtiles, but instead of using avidin/biotin SAMs, complementary single-stranded DNA oligonucleotide SAMs were formed on both the gold-coated microtiles and the target gold pads. When attempting to land the 5 µm square microtiles on matching 5 µm square target pads on a substrate, an assembly yield of only 0.28% was achieved at a selectivity ratio of 3.30:1 in favour of microtiles affixed to the target pads as opposed to the surrounding silicon substrate. These results demonstrate that the hybridization forces of complementary DNA strands are strong enough to induce low-yield assembly of microscale semiconductor devices. However, this interaction is evidently not as effective for self-assembly as the avidin-biotin interaction, which demonstrated superior results using the exact same procedures.

7.1. Future Work

Future research should work towards adjusting the fabrication, functionalization, and assembly procedures of Chapters 3, 4, 5, and 6 to see if it is possible to improve upon the results presented in this

thesis. Further experimentation with the self-assembly of silicon microtiles could be focused on developing a method to release a much higher number of functionalized microtiles into solution, so that there is at least an order of magnitude more microtiles in the solution available for assembly than there are available target sites to be assembled onto. This might be able to significantly increase the assembly yield. Other experiments could also investigate a wider range of microtile shapes and sizes than the ones tested in this thesis. It would be very interesting to see what kind of assembly yields are possible using the process outlined in Chapter 5 to fabricate and assemble microtiles that are even smaller than 5 μm wide. However, in order for the microtiles to continue to have a tile-like aspect ratio, an SOI wafer with an even thinner device layer thickness than the one used in this thesis (~2 μm device layer thickness) should be used. By using an SOI wafer with a thinner device layer thickness such as 350 nm, narrower microtiles with widths such as 1 μm or 2 μm could be fabricated and assembled using the procedures from this thesis. A size range experiment could be performed with these devices and target pad substrates with matching pad sizes to determine an exact size range for which this particular assembly process is the most useful.

A great amount of future work could be put towards the SAMs that were used to drive the assembly in this work. Further characterization should be performed to verify the avidin and biotin SAMs. Techniques such as null ellipsometry, [132] quartz crystal microbalance, [133], [134] or surface plasmon resonance [135] could be used to estimate the surface densities of these SAMs. The fractional composition of the mixed monolayer biotin-PEG-SH/methoxy-PEG-SH SAM could also be estimated using X-ray photoelectron spectroscopy. [136] It would also be interesting to investigate some different SAM compositions or architectures than the ones that were already used in this work. For example, instead of using polyethylene glycol (PEG) as a spacer chain in the biotin SAM (the one illustrated in Figure 4.1 and Figure 5.4), a different spacer chain could be chosen. The main reason why this might improve upon the performance of the SAM is because numerous studies have shown PEG-containing SAMs on silicon or gold surfaces to demonstrate reduced interaction with a large variety of proteins. [137], [138], [139]

Another issue with the avidin and biotin SAMs used in this work appears to be that the binding occurs rapidly, and once the bond is formed, there is minimal flexibility for the assembled components to adjust their position or further align themselves to the target site. A different SAM architecture that may be able improve the alignment of the microtiles is one where the binding interaction between the target pad and the microtiles increases in strength over time. One way for this to occur is to employ multiple binding interactions. A low-energy, non-specific adhesion interaction could be employed to bring the microtiles into close contact with the pads (but not completely secure their positions), and then a high-energy, specific binding interaction could be employed afterwards to fully secure the microtiles. It may be possible to develop a mechanism to manually activate this second binding interaction after a predetermined amount of time. Another potential approach would be to skew the architecture of the SAM so that the first (low-energy) interaction ensues from a longer chain in the SAM, while the second (high-energy) interaction ensues from a shorter chain in the SAM. In this SAM architecture, the longer chain interaction would act first, bringing the microtile into contact with the target pad, and then the second interaction could bring about further specific binding once the two SAMs (microtile and target pad) are in close contact. There are also complex proteins that could be considered for this approach. Some multi-component proteins or antibodies have multiple binding affinities (with varying strengths) for different molecules, [140] so a mixed monolayer target SAM could be designed with multiple terminal molecules to which a complex protein can bind.

Further attempts at the experiments of Chapter 6 should also be performed to further evaluate the capabilities for complementary DNA oligonucleotides to be employed for driving the self-assembly of microscale components. Although this binding interaction may not be as strong as the avidin-biotin interaction, this approach has may have other advantages, such as extensive capabilities for programmability, or a promising potential for alignment of the microtiles induced annealing and cooling cycles near the DNA melting point. External kinetic forces such as agitation of the substrate may also help to further align the microtiles during these annealing/cooling cycles. In a similar form to the experiments of Chapter 4, the microtile assembly results may be improved upon by conducting an

experiment where the DNA SAM reagent concentrations are varied to determine which quantity of reagent will result in the highest assembly yield by producing the best SAMs for hybridization.

8. Appendix

8.1. Derivation of Equation 4.2

In section 4.1.5, a clustering analysis using histograms was described and applied to the assembled microsphere images of Chapter 4. In the histograms, expected bin values based on a random distribution of the assembled microspheres in each image were calculated from Equation 4.2. An example histogram comparing the observed results and the predicted random distribution results computed from Equation 4.2 is shown in Figure 4.6. The equation was employed to calculate the histogram values for the average number of neighbouring microspheres in each bin range, with an accounting of the effect of the pad boundaries. Equation 4.2 reads:

$$N_{bin,\,predicted\ average} = \frac{\left(L_y - \frac{2Bin_{upper}}{\pi}\right)}{L_y} \cdot \frac{\pi N_{assembled}\left(Bin_{upper}^2 - Bin_{lower}^2\right)}{L_x L_y}, \tag{8.1}$$

where: $N_{bin,\,predicted\ average}$ is the predicted average number of particles in each bin, averaged across the entire pad,

L_y is the length of the gold pad in the y-direction (the longer direction),

L_x is the length of the gold pad in the x-direction (the shorter direction),

Bin_{upper} is the upper boundary of the distance bin being solved for,

Bin_{lower} is the lower boundary of the distance bin being solved for, and

$N_{assembled}$ is the total number of particles assembled onto the target pad being analyzed.

In this appendix section, the derivation of this formula is presented.[141] Figure 8.1A illustrates S_{bin}, the surface area around a particle corresponding to a particular bin. The predicted frequency of inter-particle distance counts in the bin should be based on this area, which is simply equal to the difference between the area of the upper bin radius (Bin_{upper}) circle and the lower bin radius (Bin_{lower}) circle:

$$S_{bin} = \pi\left(Bin_{upper}^2 - Bin_{lower}^2\right) . \tag{8.2}$$

For a random distribution of particles, the frequency should also be dependent on the density of particles across the entire target pad, $\rho_{assembled}$. This density is equal to the total number of assembled particles divided by the total pad area:

$$\rho_{assembled} = \frac{N_{assembled}}{L_x L_y}. \tag{8.3}$$

If all of the assembled particles were located far enough from the pad's boundaries, Equations (8.2) and (8.3) would be sufficient to predict the frequency of inter-particle distances for a random distribution. However, some of the particles are found in the vicinity of the pad boundaries, as illustrated in Figure 8.1B. For these particles, an accounting for the influence of the boundaries should be made.

To predict the average number of particles in each bin accounting for the pad's boundary effects, a model is considered of a target pad that has boundaries in *y*-directions, but not in *x*-directions, as can be seen in Figure 8.1C. Such a model is applicable at the condition $L_x >> L_y$, which is reasonably satisfied here. Figure 8.1D shows how the area corresponding to a bin changes when a particle's distance from the boundary, *r*, is less than Bin_{upper}. Instead of Equation 8.2, the area where particles from a given bin are observed is approximately described by the following equation,

$$S_{\text{bin}}^{\text{boundary}}(r) = \left(1 - \pi^{-1} \arccos\left(\frac{r}{Bin_{upper}}\right)\right) S_{\text{bin}}, \tag{8.4}$$

where for each Bin_{upper}, S_{bin} is given by Equation 8.2. The bin area is affected for all particles found at distances $0 < r < Bin_{upper}$ from the boundaries.

By averaging over the entire target pad, the area corresponding to a per-particle bin is:

$$\left\langle S_{\text{bin}} \right\rangle = \left(\frac{L_y - 2Bin_{upper}}{L_y}\right) S_{\text{bin}} + 2L_y^{-1} \int_0^{\text{Bin}_{\text{upper}}} S_{\text{bin}}^{\text{boundary}}(r)\, dr. \tag{8.5}$$

In the right hand side of Equation 8.5, the first term represents particles located away from boundaries of the pad while the second term represents particles that are found close to the boundaries and affected by

them. The equation is valid at the condition $2Bin_{upper} < L_y$. Equation 4.2/8.1 can be obtained by performing the algebra in Equation 8.5 and combining it with Equation 8.3 in the following manner:

$$N_{bin,\,predicted\ average} = \rho_{assembled}\langle S_{bin}\rangle \ . \tag{8.6}$$

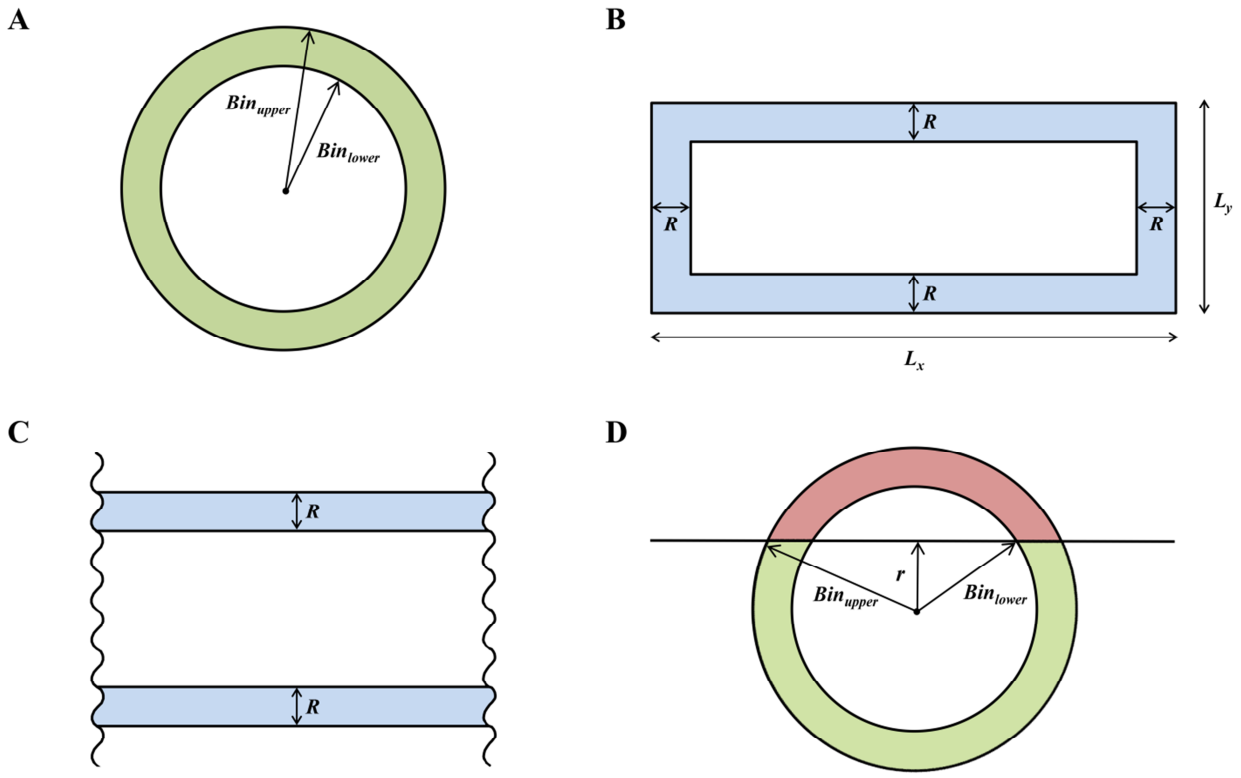

Figure 8.1: Illustrations of the model employed to derive Equation 4.1. (A) demonstrates the area of a particular bin for a particle located far from the pad's boundaries, (B) demonstrates the areas near the pad boundaries where the frequencies are affected by the boundaries, (C) demonstrates the model when assuming that the effect of the boundary along the *x*-direction is negligible because the pad length in the *x*-direction (L_x) is much longer than in the y-direction (L_y), and (D) demonstrates the effects of the pad boundaries on the corresponding bin area when a particle is located within Bin_{upper} of the pad boundary. [141]

8.2. Supplementary Figures

This section contains extra figures relevant to the thesis work.

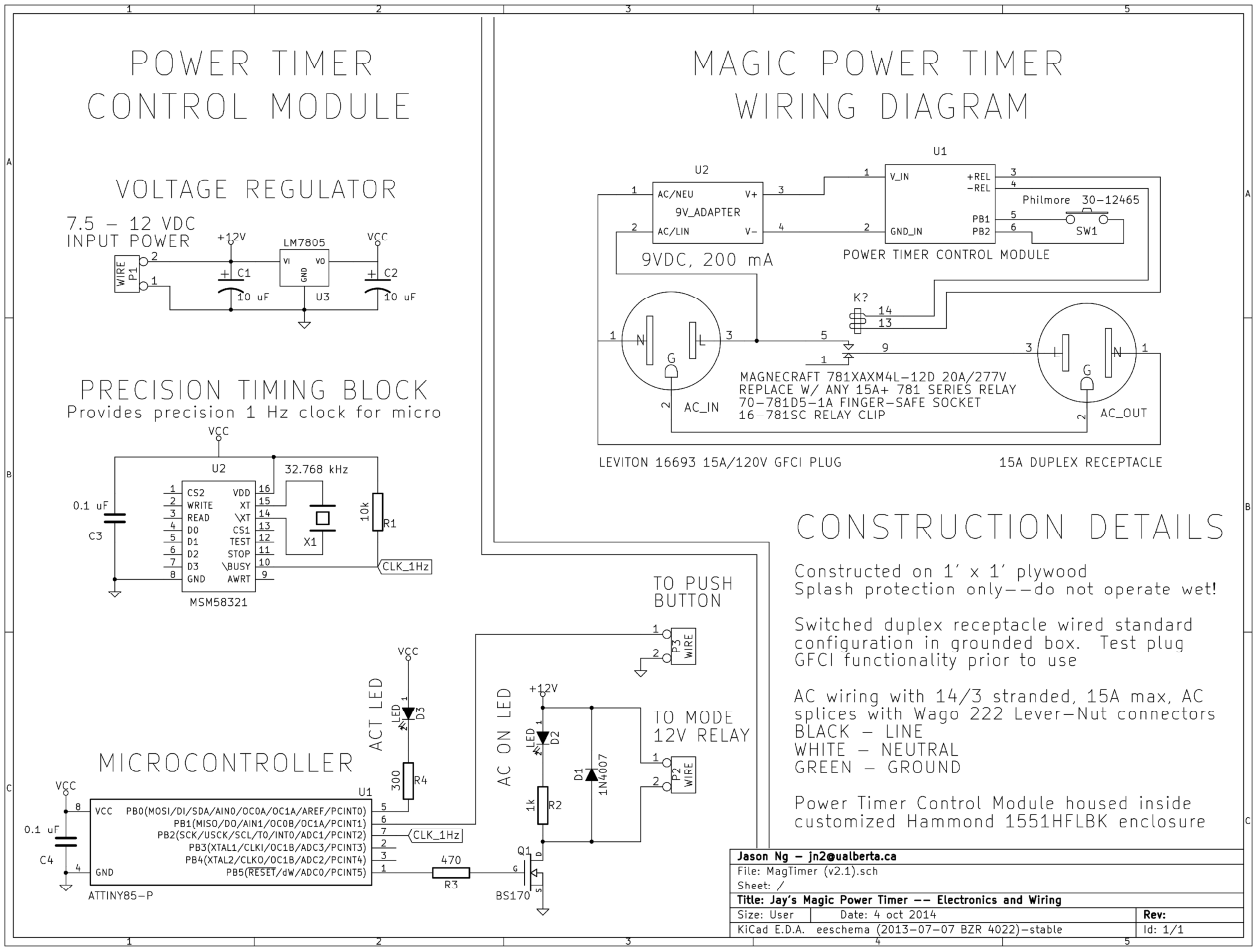

Figure 8.2: Circuit level schematic and wiring diagram of the timer apparatus used to switch on (provide power to) the magnetic stirrer in 2 minute cycles for 24 hours. This apparatus was designed and constructed by Jason Ng. [124]

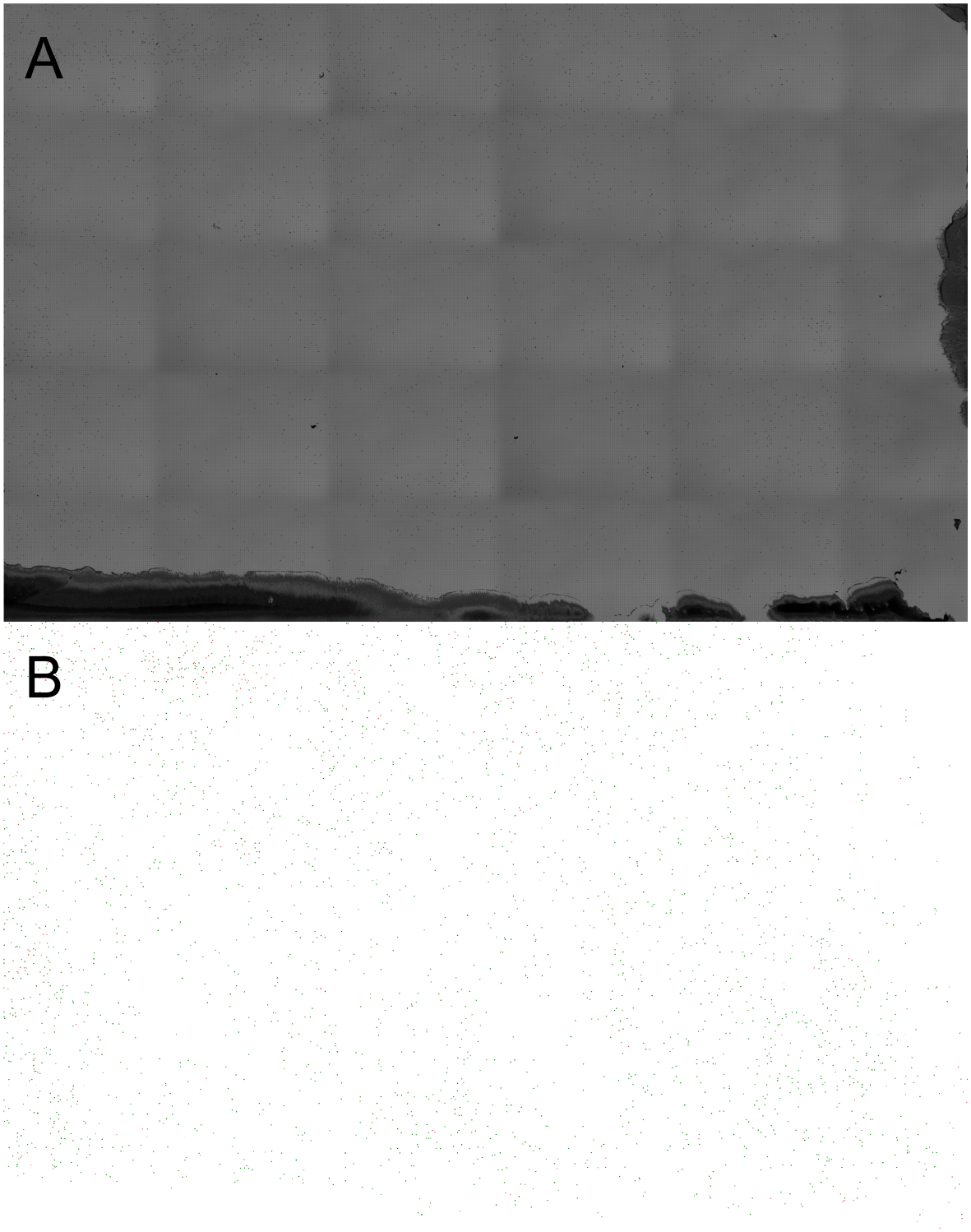

Figure 8.3: (A) Photostitched image of entire 7 mm x 4.5 mm target pad substrate (30 images from confocal microscope) with 5 µm square silicon microtiles assembled onto gold pads of the same size. This photostitch is from the most successful assembly run, with 2853 microtiles assembled overlapping with the target gold pads and 390 on the background silicon substrate, (B) The same photostitched substrate image after an ImageJ analysis counted the total number of microtiles on the substrate (on and off pads) to be 3243. The microtiles that landed on the target gold pads are labeled in green, while the microtiles on the background silicon (off of the pads) are labeled in red.

Works Cited

[1] J. R. Heath, "Molecular electronics," *Annual Review of Materials Research,* vol. 39, pp. 1--23, 2009.

[2] Z. A. K. Durrani, Single-electron devices and circuits in silicon, London: Imperial College Press, 2010.

[3] K. Ekinci and M. Roukes, "Nanoelectromechanical systems," *Review of Scientific Instruments,* vol. 76, no. 6, p. 061101, 2005.

[4] G. M. Whitesides and B. Grzybowski, "Self-assembly at all scales," *Science,* vol. 295, no. 5564, pp. 2418--2421, 2002.

[5] M. Boncheva and G. M. Whitesides, "Making things by self-assembly," *Materials Research Society Bulletin,* vol. 30, no. 10, pp. 736--742, 2005.

[6] C. J. Morris, S. A. Stauth and B. A. Parviz, "Self-assembly for microscale and nanoscale packaging: steps toward self-packaging," *IEEE Transactions on Advanced Packaging,* vol. 28, no. 4, pp. 600--611, 2005.

[7] H. S. Khoo, C. Lin, S.-H. Huang and F.-G. Tseng, "Self-assembly in micro-and nanofluidic devices: A review of recent efforts," *Micromachines,* vol. 2, no. 1, pp. 17--48, 2011.

[8] O. Laitinen, V. Hytönen, H. Nordlund and M. Kulomaa, "Genetically engineered avidins and streptavidins," *Cellular and Molecular Life Sciences,* vol. 63, no. 24, pp. 2992--3017, 2006.

[9] S. C. Esener, D. Hartmann, M. J. Heller and J. M. Cable, "DNA-assisted microassembly: a heterogeneous integration technology for optoelectronics," *Critical Reviews of Optical Science and Technology,* vol. 70, pp. 113--140, 1998.

[10] T. Olsen, J. Ng, M. Stepanova and S. K. Dew, "Programmed self-assembly of microscale components using biomolecular recognition through the avidin--biotin interaction," *Journal of Vacuum Science & Technology B,* vol. 32, no. 6, p. 06F301, 2014.

[11] C. Bower, E. Menard and P. Garrou, "Transfer printing: an approach for massively parallel assembly of microscale devices," in *58th Electronic Components and Technology Conference*, Lake Buena Vista, Florida, 2008.

[12] G. M. Whitesides and M. Boncheva, "Beyond molecules: Self-assembly of mesoscopic and macroscopic components," *Proceedings of the National Academy of Sciences,* vol. 99, no. 8, pp. 4769--4774, 2002.

[13] M. Mastrangeli, S. Abbasi, C. Varel, C. Van Hoof, J.-P. Celis and K. F. Böhringer, "Self-assembly from milli- to nanoscales: methods and applications," *Journal of Micromechanics and Microengineering,* vol. 19, no. 8, p. 083001, 2009.

[14] G. Zhang, M. Graef and F. van Roosmalen, "Strategic Research Agenda of "More than Moore"," in *IEEE International Conference on Thermal, Mechanical and Multiphysics Simulation and Experiments in Micro-Electronics and Micro-Systems*, Como, Italy, 2006.

[15] M. Mastrangeli, W. Ruythooren, J.-P. Celis and C. Van Hoof, "Challenges for capillary self-assembly of microsystems," *IEEE Transactions on Components, Packaging and Manufacturing Technology,* vol. 1, no. 1, pp. 133--149, 2011.

[16] V. Sariola, M. Jaaskelainen and Q. Zhou, "Hybrid microassembly combining robotics and water droplet self-alignment," *IEEE Transactions on Robotics,* vol. 26, no. 6, pp. 965--977, 2010.

[17] R. J. Knuesel and H. O. Jacobs, "Self-assembly of microscopic chiplets at a liquid-liquid-solid interface forming a flexible segmented monocrystalline solar cell," *Proceedings of the National Academy of Sciences,* vol. 107, no. 3, pp. 993--998, 2010.

[18] S. Kim, J. Wu, A. Carlson, S. H. Jin, A. Kovalsky, P. Glass, Z. Liu, N. Ahmed, S. L. Elgan, W. Chen, P. M. Ferreira, M. Sitti, Y. Huang and J. A. Rogers, "Microstructured elastomeric surfaces with reversible adhesion and examples of their use in deterministic assembly by transfer printing," *Proceedings of the National Academy of Sciences,* vol. 107, no. 40, pp. 17095--17100, 2010.

[19] M. A. Meitl, Z.-T. Zhu, V. Kumar, K. J. Lee, X. Feng, Y. Y. Huang, I. Adesida, R. G. Nuzzo and J. A. Rogers, "Transfer printing by kinetic control of adhesion to an elastomeric stamp," *Nature Materials,* vol. 5, no. 1, pp. 33--38, 2005.

[20] M. Mastrangeli, "Surface tension-driven self-assembly," in *Surface Tension in Microsystems*, Berlin, Springer Berlin Heidelberg, 2013, pp. 227--253.

[21] S. E. Chung, W. Park, S. Shin, S. A. Lee and S. Kwon, "Guided and fluidic self-assembly of microstructures using railed microfluidic channels," *Nature Materials,* vol. 7, no. 7, pp. 581--587, 2008.

[22] S. A. Stauth and B. A. Parviz, "Self-assembled single-crystal silicon circuits on plastic," *Proceedings of the National Academy of Sciences,* vol. 103, no. 38, pp. 13922--13927, 2006.

[23] M. Liu, W. Lau and J. Yang, "On-demand multi-batch self-assembly of hybrid MEMS by patterning solders of different melting points," *Journal of Micromechanics and Microengineering,* vol. 17, no. 11, p. 2163, 2007.

[24] J. D. Le, Y. Pinto, N. C. Seeman, K. Musier-Forsyth, T. A. Taton and R. A. Kiehl, "DNA-templated self-assembly of metallic nanocomponent arrays on a surface," *Nano Letters,* vol. 4, no. 12, pp. 2343--2347, 2004.

[25] M. P. Nikitin, T. A. Zdobnova, S. V. Lukash, O. A. Stremovskiy and S. M. Deyev, "Protein-assisted self-assembly of multifunctional nanoparticles," *Proceedings of the National Academy of Sciences,* vol. 107, no. 13, pp. 5827--5832, 2010.

[26] X. Xiong, Y. Hanein, J. Fang, Y. Wang, W. Wang, D. T. Schwartz and K. Bohringer, "Controlled multibatch self-assembly of microdevices," *Journal of Microelectromechanical Systems,* vol. 12, no. 2, pp. 117--127, 2003.

[27] J. Chung, W. Zheng, T. J. Hatch and H. O. Jacobs, "Programmable reconfigurable self-assembly: parallel heterogeneous integration of chip-scale components on planar and nonplanar surfaces," *Journal of Microelectromechanical Systems,* vol. 15, no. 3, pp. 457--464, 2006.

[28] A. O'Riordan, P. Delaney and G. Redmond, "Field configured assembly: programmed manipulation and self-assembly at the mesoscale," *Nano Letters,* vol. 4, no. 5, pp. 761--765, 2004.

[29] H.-J. J. Yeh and J. S. Smith, "Fluidic self-assembly for the integration of GaAs light-emitting diodes on Si substrates," *Photonics Technology Letters, IEEE,* vol. 6, no. 6, pp. 706--708, 1994.

[30] A. K. Verma, M. A. Hadley, H.-J. J. Yeh and J. Smith, "Fluidic self-assembly of silicon microstructures," in *Electronic Components and Technology Conference, 1995. Proceedings., 45th*, Las Vegas, NV, 1995.

[31] J. S. Smith and H.-J. J. Yeh, "Method and apparatus for fabricating self-assembling microstructures". USA Patent 5,824,186, 20 October 1998.

[32] J. S. Smith, M. A. Hadley, G. S. Craig and P. F. Nealey, "Methods and apparatuses for improved flow in performing fluidic self assembly". USA Patent 6,527,964, 4 March 2003.

[33] J. S. Smith and R. G. Stewart, "Methods and apparatuses to identify devices". USA Patent 6,988,667, 24 January 2006.

[34] A. Terfort, N. Bowden and G. M. Whitesides, "Three-dimensional self-assembly of millimetre-scale components," *Nature,* vol. 386, no. 6621, pp. 162--164, 1997.

[35] J. Tien, T. L. Breen and G. M. Whitesides, "Crystallization of millimeter-scale objects with use of capillary forces," *Journal of the American Chemical Society,* vol. 120, no. 48, pp. 12670--12671, 1998.

[36] T. L. Breen, J. Tien, R. Scott, T. Hadzic and G. M. Whitesides, "Design and self-assembly of open, regular, 3D mesostructures," *Science,* vol. 284, no. 5416, pp. 948--951, 1999.

[37] U. Srinivasan, D. Liepmann and R. T. Howe, "Microstructure to substrate self-assembly using capillary forces," *Journal of Microelectromechanical Systems,* vol. 10, no. 1, pp. 17--24, 2001.

[38] H. A. Biebuyck and G. M. Whitesides, "Self-organization of organic liquids on patterned self-assembled monolayers of alkanethiolates on gold," *Langmuir,* vol. 10, no. 8, pp. 2790--2793, 1994.

[39] U. Srinivasan, M. A. Helmbrecht, C. Rembe, R. S. Muller and R. T. Howe, "Fluidic self-assembly of micromirrors onto microactuators using capillary forces," *IEEE Journal of Selected Topics in Quantum Electronics,* vol. 8, no. 1, pp. 4--11, 2002.

[40] M. Mastrangeli, W. Ruythooren, C. Van Hoof and J.-P. Celis, "Conformal dip-coating of patterned surfaces for capillary die-to-substrate self-assembly," *Journal of Micromechanics and Microengineering,* vol. 19, no. 4, pp. 045015--045027, 2009.

[41] K. F. Böhringer, "Surface modification and modulation in microstructures: controlling protein adsorption, monolayer desorption and micro-self-assembly," *Journal of Micromechanics and Microengineering,* vol. 13, no. 4, p. S1, 2003.

[42] C. Lin, F.-G. Tseng and C.-C. Chieng, "Orientation-specific fluidic self-assembly process based on a capillary effect," *Journal of Micromechanics and Microengineering,* vol. 19, no. 11, p. 115020, 2009.

[43] S.-H. Liang, K. Wang and K. F. Bohringer, "Self-assembly of mems components in air assisted by diaphragm agitation," in *18th IEEE International Conference on Micro Electro Mechanical Systems*, Miami Beach, FL, 2005.

[44] H. O. Jacobs, A. R. Tao, A. Schwartz, D. H. Gracias and G. M. Whitesides, "Fabrication of a cylindrical display by patterned assembly," *Science,* vol. 296, no. 5566, pp. 323--325, 2002.

[45] W. Zheng, J. Chung and H. O. Jacobs, "Fluidic heterogeneous microsystems assembly and packaging," *Journal of Microelectromechanical Systems,* vol. 15, no. 4, pp. 864--870, 2006.

[46] W. Zheng and H. O. Jacobs, "Fabrication of Multicomponent Microsystems by Directed Three-Dimensional Self-Assembly," *Advanced Functional Materials,* vol. 15, no. 5, pp. 732--738, 2005.

[47] S. S. Kim, E. Saeedi, J. R. Etzkorn and B. A. Parviz, "Large scale self-assembly of crystalline semiconductor microcomponents onto plastic substrates via microfluidic traps," in *IEEE International Conference on Automation Science and Engineering*, Washington, DC, USA, 2008.

[48] E. Saeedi, S. Kim and B. A. Parviz, "Self-assembled crystalline semiconductor optoelectronics on glass and plastic," *Journal of Micromechanics and Microengineering,* vol. 18, no. 17, p. 075019, 2008.

[49] S.-C. Park, J. Fang, S. Biswas, M. Mozafari, T. Stauden and H. O. Jacobs, "A First Implementation of an Automated Reel-to-Reel Fluidic Self-Assembly Machine," *Advanced Materials,* vol. 26, no. 34, pp. 5942--5949, 2014.

[50] W. Zheng and H. O. Jacobs, "Self-Assembly Process to Integrate and Connect Semiconductor Dies on Surfaces with Single-Angular Orientation and Contact-Pad Registration," *Advanced Materials,* vol. 18, no. 11, pp. 1387--1392, 2006.

[51] R. J. Knuesel and H. O. Jacobs, "Self-Tiling Monocrystalline Silicon; a Process to Produce Electrically Connected Domains of Si and Microconcentrator Solar Cell Modules on Plastic Supports," *Advanced Materials,* vol. 23, no. 24, pp. 2727--2733, 2011.

[52] J. Lavin, R. A. Kemp and C. A. Stewart, "Photovoltaic self-assembly," Sandia National Laboratories, Albuquerque, New Mexico, 2010.

[53] B. Chang, I. Routa, V. Sariola and Q. Zhou, "Self-alignment of RFID dies on four-pad patterns with water droplet for sparse self-assembly," *Journal of Micromechanics and Microengineering,* vol. 21, no. 9, p. 095024, 2011.

[54] A. Shah, B. Chang, S. Suihkonen, Q. Zhou and H. Lipsanen, "Surface-tension-driven self-alignment of microchips on black-silicon-based hybrid template in ambient air," *Journal of Microelectromechanical Systems,* vol. 22, no. 3, pp. 739--746, 2013.

[55] B. Chang, V. Sariola, M. Jääskeläinen and Q. Zhou, "Self-alignment in the stacking of microchips with mist-induced water droplets," *Journal of Micromechanics and Microengineering,* vol. 21, no. 1, p. 015016, 2011.

[56] B. Chang, A. Shah, I. Routa, H. Lipsanen and Q. Zhou, "Low-height sharp edged patterns for capillary self-alignment assisted hybrid microassembly," *Journal of Micro-Bio Robotics,* vol. 9, no. 1-2, pp. 1--10, 2014.

[57] J. Tien, A. Terfort and G. M. Whitesides, "Microfabrication through electrostatic self-assembly," *Langmuir,* vol. 13, no. 20, pp. 5349--5355, 1997.

[58] K.-F. Böhringer, K. Goldberg, M. Cohn, R. Howe and A. Pisano, "Parallel microassembly with electrostatic force fields," *1998 IEEE International Conference on Robotics and Automation,* vol. 2, pp. 1204--1211, 1998.

[59] S. Lee, H. McNally, D. Guo, M. Pingle, D. Bergstrom and R. Bashir, "Electric-field-mediated assembly of silicon islands coated with charged molecules," *Langmuir,* vol. 18, no. 8, pp. 3383--3386, 2002.

[60] C. Edman, R. Swint, C. Gurtner, R. Formosa, S. Roh, K. Lee, P. Swanson, D. Ackley, J. Coleman and M. Heller, "Electric field directed assembly of an InGaAs LED onto silicon circuitry," *IEEE Photonics Technology Letters,* vol. 12, no. 9, pp. 1198--1200, 2000.

[61] T. S. Mayer, T. N. Jackson and C. D. Nordquist, "Electro-fluidic assembly process for integration of electronic devices onto a substrate". USA Patent 6,687,987, 10 February 2004.

[62] S. Lee and R. Bashir, "Dielectrophoresis and electrohydrodynamics-mediated fluidic assembly of silicon resistors," *Applied Physics Letters,* vol. 83, no. 18, pp. 3833--3835, 2003.

[63] S. W. Lee and R. Bashir, "Dielectrophoresis and Chemically Mediated Directed Self-Assembly of Micrometer-Scale Three-Terminal Metal Oxide Semiconductor Field-Effect Transistors," *Advanced Materials,* vol. 17, no. 22, pp. 2671--2677, 2005.

[64] C. G. Fonstad Jr, "Magnetically-Assisted Statistical Assembly - a new heterogeneous integration technique," *Advanced Materials for Micro- and Nano-Systems (AMMNS),* 2002.

[65] S. Shet, V. R. Mehta, A. T. Fiory, N. Ravindra and M. P. Lepselter, "The magnetic field-assisted assembly of nanoscale semiconductor devices: A new technique," *JOM,* vol. 56, no. 10, pp. 32--34, 2004.

[66] S. B. Shetye, I. Eskinazi and D. P. Arnold, "Self-assembly of millimeter-scale components using integrated micromagnets," *IEEE Transactions on Magnetics,* vol. 44, no. 11, pp. 4293--4296, 2008.

[67] C. J. Morris, B. Isaacson, M. D. Grapes and M. Dubey, "Self-assembly of microscale parts through magnetic and capillary interactions," *Micromachines,* vol. 2, no. 1, pp. 69--81, 2011.

[68] K. S. Park, J. H. Hoo, R. Baskaran and K. Bohringer, "Parallel Heterogeneous Integration of Chip-Scale Parts by Self-Assembly," *Journal of Microelectromechanical Systems,* vol. 21, no. 6, pp. 1273--1275, 2012.

[69] C. A. Mirkin, R. L. Letsinger, R. C. Mucic and J. J. Storhoff, "A DNA-based method for rationally assembling nanoparticles into macroscopic materials," *Nature,* vol. 382, no. 6592, pp. 607--609, 1996.

[70] D. M. Hartmann, M. Heller, S. Esener, D. Schwartz and G. Tu, "Selective DNA attachment of micro-and nanoscale particles to substrates," *Journal of Materials Research,* vol. 17, no. 2, pp. 473--478, 2002.

[71] M. Grzelczak, J. Vermant, E. M. Furst and L. M. Liz-Marzán, "Directed self-assembly of nanoparticles," *ACS Nano,* vol. 4, no. 7, pp. 3591--3605, 2010.

[72] H. T. Maune, S.-P. Han, R. D. Barish, M. Bockrath, W. A. Goddard III, P. W. Rothemund and E. Winfree, "Self-assembly of carbon nanotubes into two-dimensional geometries using DNA origami templates," *Nature Nanotechnology,* vol. 5, no. 1, pp. 61--66, 2009.

[73] R. Bashir, S. Lee, D. Guo, M. Pingle, D. Bergstrom, H. McNally and D. Janes, "Basic: Bio-inspired assembly of semiconductor integrated circuits," in *MRS Proceedings*, Boston, MA, 2000.

[74] H. McNally, M. Pingle, S. Lee, D. Guo, D. E. Bergstrom and R. Bashir, "Self-assembly of micro-and nano-scale particles using bio-inspired events," *Applied Surface Science,* vol. 214, no. 1, pp. 109--119, 2003.

[75] T. Kusakabe, T. Tanemura, Y. Higuchi, K. Sugano, T. Tsuchiya and O. Tabata, "DNA mediated sequential self-assembly of nano/micro components," in *IEEE 21st International Conference on Micro Electro Mechanical Systems*, Tuscon, AZ, 2008.

[76] M. Yasuda, T. Hayashi, M. Michihata and Y. Takaya, "A Novel Batch Fabrication of Micro Parts Using DNA Pattern Recognition," *Key Engineering Materials,* vol. 523, pp. 598--603, 2012.

[77] M. P. Williamson, How proteins work, New York, NY: Garland Science, 2012.

[78] G. Gitlin, E. A. Bayer and M. Wilchek, "Studies on the biotin-binding site of avidin. Tryptophan residues involved in the active site," *Biochemical Journal,* vol. 242, pp. 291--294, 1987.

[79] S. R. Whaley, D. English, E. L. Hu, P. F. Barbara and A. M. Belcher, "Selection of peptides with semiconductor binding specificity for directed nanocrystal assembly," *Nature,* vol. 405, no. 6787, pp. 665--668, 2000.

[80] A. Arakaki, S. Hideshima, T. Nakagawa, D. Niwa, T. Tanaka, T. Matsunaga and T. Osaka, "Detection of biomolecular interaction between biotin and streptavidin on a self-assembled monolayer using magnetic nanoparticles," *Biotechnology and Bioengineering,* vol. 88, no. 4, pp. 543--546, 2004.

[81] S. Pierrat, I. Zins, A. Breivogel and C. Sönnichsen, "Self-assembly of small gold colloids with functionalized gold nanorods," *ACS Publications,* vol. 7, no. 2, pp. 259--263, 2007.

[82] H. McNally, S. Lee, D. Guo, M. Pingle, D. Bergstrom and R. Bashir, "Bio-inspired Self-Assembly of Micro and Nano-Structures for Sensing and Electronic Applications," *MRS Proceedings,* vol. 739, pp. H9--7, 2002.

[83] S. Takahashi, K. Sato and J.-i. Anzai, "Layer-by-layer construction of protein architectures through avidin--biotin and lectin--sugar interactions for biosensor applications," *Analytical and Bioanalytical Chemistry,* vol. 402, no. 5, pp. 1749--1758, 2012.

[84] N. Kresge, R. D. Simoni and R. L. Hill, "The Discovery of avidin by Esmond E. Snell," *Journal of Biological Chemistry,* vol. 279, no. 41, pp. e5--e5, 2004.

[85] H. Nordlund, Avidin engineering: modification of function, oligomerization, stability and structure topology, University of Jyväskylä: Jyväskylän Yliopisto, 2003.

[86] T. Bing, T. Chang, C. Qi, N. Zhang, X. Liu and D. Shangguan, "Specific interactions between adenosine and streptavidin/avidin," *Bioorganic & Medicinal Chemistry Letters,* vol. 22, no. 23, pp. 7052--7055, 2012.

[87] L. M. Shamansky, C. B. Davis, J. K. Stuart and W. G. Kuhr, "Immobilization and detection of DNA on microfluidic chips," *Talanta,* vol. 55, no. 5, pp. 909--918, 2001.

[88] M. Wilchek and E. Bayer, "Avidin-biotin immobilisation systems," in *Immobilised Macromolecules: Application Potentials*, London, Springer, 1993, pp. 51--60.

[89] A. Holmberg, A. Blomstergren, O. Nord, M. Lukacs, J. Lundeberg and M. Uhlén, "The biotin-streptavidin interaction can be reversibly broken using water at elevated temperatures," *Electrophoresis,* vol. 26, no. 3, pp. 501--510, 2005.

[90] N. Green, L. Konieczny, E. Toms and R. Valentine, "The use of bifunctional biotinyl compounds to determine the arrangement of subunits in avidin," *Biochemical Journal,* vol. 125, pp. 781--791, 1971.

[91] L. Pugliese, A. Coda, M. Malcovati and M. Bolognesi, "Three-dimensional Structure of the Tetragonal Crystal Form of Egg-white Avidin in its functional Complex with Biotin at 2·7 Å Resolution," *Journal of Molecular Biology,* vol. 231, no. 3, pp. 698--710, 1993.

[92] B. Kuhn and P. A. Kollman, "A ligand that is predicted to bind better to avidin than biotin: insights from computational fluorine scanning," *Journal of the American Chemical Society,* vol. 122, no. 16, pp. 3909--3916, 2000.

[93] A. Ulman, "Formation and structure of self-assembled monolayers," *Chemical Reviews,* vol. 96, no. 4, pp. 1533--1554, 1996.

[94] N. Fahmy, M. Woo, M. Alameldin, K. C. J. Lee, K. MacDonald, L. W. Goneau, P. Cadieux, J. Burton and S. E. Pautler, "Endogenous biotin expression in renal and testicular tumors and literature review," *Canadian Urological Association Journal,* vol. 8, no. 7-8, pp. 268--272, 2014.

[95] J. Nix, D. Sussman and C. Wilson, "The 1.3 Å crystal structure of a biotin-binding pseudoknot and the basis for RNA molecular recognition," *Journal of Molecular Biology,* vol. 296, no. 5, pp. 1235--1244, 2000.

[96] Thermo Scientific Avidin-Biotin Technical Handbook, Waltham, MA: Thermo Fisher Scientific Inc. , 2009.

[97] E. P. Diamandis and T. K. Christopoulos, "The biotin-(strept) avidin system: principles and applications in biotechnology," *Clinical Chemistry,* vol. 37, no. 5, pp. 625--636, 1991.

[98] M. Wilchek and E. A. Bayer, "Applications of avidin-biotin technology: literature survey," *Methods in Enzymology,* vol. 184, pp. 14--45, 1990.

[99] J. Snider, "Protein Methods Library: Avidin-Biotin Interaction," [Online]. Available: http://www.piercenet.com/method/avidin-biotin-interaction. [Accessed 24 Aug. 2014].

[100] L. A. De Jong, D. R. Uges, J. P. Franke and R. Bischoff, "Receptor--ligand binding assays: technologies and applications," *Journal of Chromatography B,* vol. 829, no. 1, pp. 1--25, 2005.

[101] M. Wilchek and E. Bayer, "Avidin-biotin immobilization systems," in *Immobilized Biomolecules in Analysis : A Practical Approach*, Oxford, Springer/Oxford University Press, 1998, pp. 15--34.

[102] E. Bayer and M. Wilchek, "Modified avidins for application in avidin-biotin technology: an improvement on nature," in *Egg uses and processing technologies, new developments*, Cab International, 1994, pp. 158--177.

[103] J. C. Love, L. A. Estroff, J. K. Kriebel, R. G. Nuzzo and G. M. Whitesides, "Self-assembled monolayers of thiolates on metals as a form of nanotechnology," *Chemical Reviews,* vol. 105, no. 4, pp. 1103--1170, 2005.

[104] A. Adamson and A. Gast, "The solid--liquid interface-contact angle," *Physical Chemistry of Surfaces,* vol. 4, pp. 333--361, 1997.

[105] C. Vericat, M. Vela, G. Benitez, P. Carro and R. Salvarezza, "Self-assembled monolayers of thiols and dithiols on gold: new challenges for a well-known system," *Chemical Society Reviews,* vol. 39, no. 5, pp. 1805--1834, 2010.

[106] R. Valiokas, M. Östblom, S. Svedhem, S. C. Svensson and B. Liedberg, "Thermal stability of self-assembled monolayers: Influence of lateral hydrogen bonding," *The Journal of Physical Chemistry B,* vol. 106, no. 40, pp. 10401--10409, 2002.

[107] J. P. Bareman and M. L. Klein, "Collective tilt behavior in dense, substrate-supported monolayers of long-chain molecules: A molecular dynamics study," *Journal of Physical Chemistry,* vol. 94, no. 13, pp. 5202--5205, 1990.

[108] D. Dowling, K. Donnelly, M. McConnell, R. Eloy and M. Arnaud, "Deposition of anti-bacterial silver coatings on polymeric substrates," *Thin Solid Films,* vol. 398, pp. 602--606, 2001.

[109] V. K. Poon and A. Burd, "In vitro cytotoxity of silver: implication for clinical wound care," *Burns,* vol. 30, no. 2, pp. 140--147, 2004.

[110] X. Jiang, D. A. Bruzewicz, M. M. Thant and G. M. Whitesides, "Palladium as a substrate for self-assembled monolayers used in biotechnology," *Analytical Chemistry,* vol. 76, no. 20, pp. 6116--6121, 2004.

[111] L. H. Dubois and R. G. Nuzzo, "Synthesis, structure, and properties of model organic surfaces," *Annual Review of Physical Chemistry,* vol. 43, no. 1, pp. 437--463, 1992.

[112] C. D. Bain, E. B. Troughton, Y. T. Tao, J. Evall, G. M. Whitesides and R. G. Nuzzo, "Formation of monolayer films by the spontaneous assembly of organic thiols from solution onto gold," *Journal of the American Chemical Society,* vol. 111, no. 1, pp. 321--335, 1989.

[113] R. Yamada, H. Wano and K. Uosaki, "Effect of temperature on structure of the self-assembled monolayer of decanethiol on Au (111) surface," *Langmuir,* vol. 16, no. 13, pp. 5523--5525, 2000.

[114] H. Ma, M. Wells, T. P. Beebe and A. Chilkoti, "Surface-Initiated Atom Transfer Radical Polymerization of Oligo (ethylene glycol) Methyl Methacrylate from a Mixed Self-Assembled Monolayer on Gold," *Advanced Functional Materials,* vol. 16, no. 5, pp. 640--648, 2006.

[115] Y. Liu, M. K. Shipton, J. Ryan, E. D. Kaufman, S. Franzen and D. L. Feldheim, "Synthesis, stability, and cellular internalization of gold nanoparticles containing mixed peptide-poly (ethylene glycol) monolayers," *Analytical Chemistry,* vol. 79, no. 6, pp. 2221--2229, 2007.

[116] S.-J. Ding, B.-W. Chang, C.-C. Wu, M.-F. Lai and H.-C. Chang, "Electrochemical evaluation of avidin--biotin interaction on self-assembled gold electrodes," *Electrochimica Acta,* vol. 50, no. 18, pp. 3660--3666, 2005.

[117] Pierce Biotechnology, Inc., "NHS and Sulfo-NHS FAQ," 2014. [Online]. Available: http://www.piercenet.com/guide/nhs-sulfo-nhs-faq. [Accessed 21 Oct. 2014].

[118] J. V. Staros, R. W. Wright and D. M. Swingle, "Enhancement by N-hydroxysulfosuccinimide of water-soluble carbodiimide-mediated coupling reactions," *Analytical Biochemistry,* vol. 156, no. 1, pp. 220--222, 1986.

[119] J. H. Conway and N. J. A. Sloane, in *Sphere Packings, Lattices and Groups, 3rd ed.*, New York, Springer, 1998, p. xix.

[120] S. D. Perrault and W. C. Chan, "In vivo assembly of nanoparticle components to improve targeted cancer imaging," *Proceedings of the National Academy of Sciences,* vol. 107, no. 25, pp. 11194--11199, 2010.

[121] X. Huang, D. Du, X. Gong, J. Cai, H. Tu, X. Xu and A. Zhang, "Composite assembly of silver nanoparticles with avidin and biotinylated AChE on gold for the pesticidal electrochemical sensing," *Electroanalysis,* vol. 20, no. 4, pp. 402--409, 2008.

[122] C. A. Canaria, J. So, J. R. Maloney, C. Yu, J. O. Smith, M. L. Roukes, S. E. Fraser and R. Lansford, "Formation and removal of alkylthiolate self-assembled monolayers on gold in aqueous solutions," *Lab on a Chip,* vol. 6, no. 2, pp. 289--295, 2006.

[123] G. A. Luurtsema, "Spin coating for rectangular substrates. Master's Thesis," University of California, Berkeley, Berkeley, CA, U.S.A, 1997.

[124] Power timer control module was designed by J. Ng (unpublished). 2014.

[125] K. E. Nelson, L. Gamble, L. S. Jung, M. S. Boeckl, E. Naeemi, S. L. Golledge, T. Sasaki, D. G. Castner, C. T. Campbell and P. S. Stayton, "Surface characterization of mixed self-assembled monolayers designed for streptavidin immobilization," *Langmuir,* vol. 17, no. 9, pp. 2807--2816, 2001.

[126] F. A. Aldaye, A. L. Palmer and H. F. Sleiman, "Assembling materials with DNA as the guide," *Science,* vol. 321, no. 5897, pp. 1795--1799, 2008.

[127] J. G. Wetmur and J. Fresco, "DNA probes: applications of the principles of nucleic acid hybridization," *Critical reviews in biochemistry and molecular biology,* vol. 26, no. 3-4, pp. 227--259, 1991.

[128] J. J. Storhoff and C. A. Mirkin, "Programmed materials synthesis with DNA," *Chemical Reviews,* vol. 99, no. 7, pp. 1849--1862, 1999.

[129] Y. Sun and C.-H. Kiang, "DNA-based artificial nanostructures: Fabrication, properties, and applications," in *Handbook of Nanostructured Biomaterials* , American Scientific Publishers, 2005, pp. 224-246.

[130] J. P. Yesudas, J. Ng, A. Kovalenko and S. K. Dew, "DNA mediated heterogeneous integration of micro- and nano-scale devices," (unpublished). 2014.

[131] J. P. Yesudas, N. Blinov, S. K. Dew and A. Kovalenko, "Calculation of binding free energy of short double

stranded oligonucleotides using MM/3D-RISM-KH approach," *Journal of Molecular Liquids,* (published online) 2014.

[132] J. Benesch, A. Askendal and P. Tengvall, "The Determination of Thickness and Surface Mass Density of Mesothick Immunoprecipitate Layers by Null Ellipsometry and Protein 125Iodine Labeling," *Journal of Colloid and Interface Science,* vol. 249, no. 1, pp. 84--90, 2002.

[133] K. A. Marx, "Quartz crystal microbalance: a useful tool for studying thin polymer films and complex biomolecular systems at the solution-surface interface," *Biomacromolecules,* vol. 4, no. 5, pp. 1099--1120, 2003.

[134] F. Höök, J. Vörös, M. Rodahl, R. Kurrat, P. Böni, J. Ramsden, M. Textor, N. Spencer, P. Tengvall and J. Gold, "A comparative study of protein adsorption on titanium oxide surfaces using in situ ellipsometry, optical waveguide lightmode spectroscopy, and quartz crystal microbalance/dissipation," *Colloids and Surfaces B: Biointerfaces,* vol. 24, no. 2, pp. 155--170, 2002.

[135] J. W. Lee, S. J. Sim, S. M. Cho and J. Lee, "Characterization of a self-assembled monolayer of thiol on a gold surface and the fabrication of a biosensor chip based on surface plasmon resonance for detecting anti-GAD antibody," *Biosensors and Bioelectronics,* vol. 20, no. 7, pp. 1422--1427, 2005.

[136] M.-C. Bourg, A. Badia and R. B. Lennox, "Gold-sulfur bonding in 2D and 3D self-assembled monolayers: XPS characterization," *The Journal of Physical Chemistry B,* vol. 104, no. 28, pp. 6562--6567, 2000.

[137] M. Zhang, T. Desai and M. Ferrari, "Proteins and cells on PEG immobilized silicon surfaces," *Biomaterials,* vol. 19, no. 10, pp. 953--960, 1998.

[138] S. Sharma, K. C. Popat and T. A. Desai, "Controlling nonspecific protein interactions in silicon biomicrosystems with nanostructured poly (ethylene glycol) films," *Langmuir,* vol. 18, no. 23, pp. 8728--8731, 2002.

[139] S. Lan, M. Veiseh and M. Zhang, "Surface modification of silicon and gold-patterned silicon surfaces for improved biocompatibility and cell patterning selectivity," *Biosensors and bioelectronics,* vol. 20, no. 9, pp. 1697--1708, 2005.

[140] B. Alberts, A. Johnson, J. Lewis, M. Raff, K. Roberts and P. Walter, "Protein Function," in *Molecular Biology of the Cell, 4th Edition*, New York, Garland Science, 2002.

[141] Equation 4.2 was derived by M. Stepanova (unpublished). 2014.